**IMPERIAL COLLEGE LONDON**

**DEPARTMENT OF PHYSICS**

# Point and planar defects in titanium

Adam John Ready

September 2017

Supervised by
Professor Adrian P Sutton
and
Professor Peter D Haynes

Submitted in part fulfilment of the requirements for the degree of
Doctor of Philosophy in Physics of Imperial College London
and the Diploma of Imperial College London

# Declaration

I herewith certify that all material in this dissertation which is not my own work has been properly acknowledged. In particular the work summarised in section 6.7 was carried out by Professor Adrian P Sutton.

Adam J Ready

# Abstract

Titanium alloys are used in the aerospace industry due to their high strength, low density, and corrosion resistance. Despite all of these virtues their use is hampered by a failure mechanism called cold dwell fatigue (CDF), which can reduce the lifetime of susceptible alloys by a factor of 10.

The plastic deformation leading to CDF failure is caused by creep at stresses as low as 60% of the yield stress and at temperatures as low 15% of the melting point of Ti. This 'cold creep' is the result of the planar glide of dislocations in the hexagonal close-packed or $\alpha$-phase of Ti. Slip is the primary deformation mechanism for Ti and its alloys, so there is an inherent interest in the slip behaviour of $\alpha$-Ti.

Motivated by this I computed the entire first-order pyramidal $\gamma$-surface for $\alpha$-Ti using density functional theory (DFT) simulations. I found one low energy and one high energy stacking fault with energies of 163 and 681 mJ/m$^2$, respectively. In contrast with previous suggestions, I found no stable stable stacking fault at $(\mathbf{c}+\mathbf{a})/2$. I computed this surface using two different pseudopotentials with 4 and 12 valence states, showing that the 4 state pseudopotential adequately reproduces the results of the 12 state pseudopotential.

At the time of writing the mechanism controlling cold creep, and hence CDF is unknown. One observation for helping to understand CDF is that the Ti alloy Ti-6Al-2Sn-4Zr-2Mo is highly susceptible to CDF failure but Ti-6Al-2Sn-4Zr-6Mo is not. The main difference between these alloys is 4 weight percent Mo. Motivated by this observation and using DFT simulations I investigated a hypothesis that Mo traps vacancies in $\alpha$ grains thus reducing the creep relaxation that exacerbates the conditions leading to CDF failure. Based on my results I found no support for this hypothesis.

The copyright of this thesis rests with the author and is made available under a Creative Commons Attribution Non-Commercial No Derivatives licence. Researchers are free to copy, distribute or transmit the thesis on the condition that they attribute it, that they do not use it for commercial purposes and that they do not alter, transform or build upon it. For any reuse or redistribution, researchers must make clear to others the licence terms of this work.

# Acknowledgements

The research detailed in this thesis was supported financially by an EPSRC studentship and by a further contribution from Rolls Royce plc. The studentship was provided through the Centre for Doctoral Training on Theory and Simulation of Materials (TSM-CDT) at Imperial College London.

I would like to thank my two supervisors Professor Adrian Sutton and Professor Peter Haynes for all of their invaluable advice and support. My thanks also go to Dave Rugg FREng at Rolls Royce for helping to make this project happen, as well as for stimulating discussions about titanium, metallurgy, and their importance in aerospace.

I am grateful to have been part of the TSM CDT which provided me with a host of learning opportunities and an engaging community. Particular thanks go to Rob Wilson and Mike Ridley for innumerable discussions about music and occasional discussions about physics during my time at the TSM CDT.

I am glad to have an opportunity to thank Jörg Neugebauer and Blazej Grabowski at the Max Planck-Institut für Eisenforschung for allowing me to visit and providing a fantastic environment for learning and numerous engaging discussions.

I must thank Matthias Kraft and Fionn Malone for putting up with sharing an office with me for three whole years. The distractions from physics in the form of cheap coffee and tiny computers were most welcome.

Thanks also go to Liang-Feng Huang and Bengt Tegner for furthering my knowledge on simulating titanium.

Last but not least I thank my family for all their love and support.

# Publications

The work of this thesis has appeared in the following publications:

*Point, linear, and planar defects in titanium*, A. J. Ready, P. D. Haynes, D. Rugg, and A. P. Sutton, Proceedings of the 13th World Conference on Titanium, 2016 [1].
The work carried out by myself and reported in [1] is presented primarily in section 5.1.

*Stacking faults and the $\gamma$-surface on first-order pyramidal planes in $\alpha$-titanium*, A. J. Ready, P. D. Haynes, D. Rugg, and A. P. Sutton, Philosophy Magazine, 2017 [2].
The work carried out by myself and reported in [2] is presented primarily in sections 5.1 and 5.2.

*Comment on "Development of an interatomic potential for the simulation of defects, plasticity, and phase transformations in titanium" [J. Chem. Phys.* **145***, 154102 (2016)]*, A. J. Ready, P. D. Haynes, A. P. Sutton, Journal of Chemical Physics, 2017 [3].
The work carried out by myself and reported in [3] is presented primarily in section 5.3.

*The role of molybdenum in suppressing cold dwell fatigue in titanium alloys*, A. J. Ready, P. D. Haynes, B. Grabowski, D. Rugg, and A. P. Sutton, Proceedings of the Royal Society A, 2017 [4].
The work carried out by myself and reported in [4] is presented primarily in chapter 6.

*"Textbooks and Heaven only are Ideal;*
*Solidity is an imperfect state."*

The Dance of the Solids, by John Updike [5]

# Contents

**Declaration** 2

**Abstract** 3

**Acknowledgements** 5

**Publications** 6

**List of Figures** 10

**List of Tables** 14

**1 Introduction** 16

**2 Density functional theory** 25
2.1 The Schrödinger equation . . . 26
2.2 The Born-Oppenheimer approximation . . . 27
2.3 The Hohenberg-Kohn Theorems . . . 28
2.4 The Kohn-Sham equations . . . 31
2.5 The exchange-correlation functional . . . 33

**3 DFT for metals** 35
3.1 Reciprocal space and k-points . . . 35
3.2 Cut-off energy . . . 37
3.3 The Fermi surface . . . 38
3.4 Density mixing . . . 41
3.5 Pseudopotentials . . . 43

**4 Bulk phases of titanium** 47
4.1 The unit cell . . . 48
4.2 Convergence tests . . . 48
4.2.1 Cut-off energy . . . 48
4.2.2 Brillouin zone sampling . . . 49
4.3 Lattice parameters . . . 51
4.4 Elastic constants . . . 53
4.5 Directional bonding in Ti . . . 55

**5 Stacking faults in titanium** 58
5.1 Interatomic potential Ti0 studies . . . 59

5.1.1 Stacking sequences . . . 59
5.1.2 The interatomic potential Ti0 . . . 61
5.1.3 Stacking fault simulation methods . . . 62
5.1.4 Convergence tests . . . 64
5.1.5 Basal, prism, and pyramidal I $\gamma$-surfaces . . . 64
5.2 Density functional theory studies . . . 68
5.2.1 DFT parameters . . . 68
5.2.2 Convergence tests . . . 69
5.2.3 Basal and pyramidal I $\gamma$-surfaces . . . 71
5.3 Interatomic potential Ti1, Ti2, Ti3 tests . . . 78
5.3.1 The interatomic potentials Ti-$\{1, 2, 3\}$ . . . 78
5.3.2 $\gamma$-surfaces and stable stacking fault energies . . . 78
5.3.3 $\gamma$-surface differences . . . 79
5.3.4 $\gamma$-surface gradient differences . . . 83

**6 Point defects in titanium** **86**
6.1 Methods . . . 87
6.1.1 DFT parameters . . . 87
6.1.2 Supercell size effects in point defect calculations . . . 87
6.1.3 The formation energies of a Mo-atom in $\alpha$ and $\beta$-phases of Ti . . . 89
6.1.4 Mo-vacancy binding energy in $\alpha$-Ti . . . 89
6.2 Vacancy in $\alpha$-Ti . . . 90
6.3 Interstitial Mo in $\alpha$-Ti . . . 92
6.4 Substitutional Mo in $\alpha$- and $\beta$-Ti . . . 95
6.5 Binding energy between a Mo substitutional atom and a vacancy in $\alpha$-Ti 95
6.6 The effect of Mo in Ti-6242 and Ti-6246 . . . 97
6.7 CDF temperature dependence . . . 98

**7 Conclusions and Outlook** **101**

**A $\gamma$-surface gradients** **122**

# List of Figures


1.1 The hcp and bcc crystal structures are represented here by their conventional unit cells. The vectors $\{\mathbf{a}_1, \mathbf{a}_2, \mathbf{a}_3, \mathbf{c}\}$ in (A) and $\{\mathbf{a}, \mathbf{b}, \mathbf{c}\}$ in (B) are the Miller (Bravais) crystal lattice vectors for hcp and bcc respectively. . . 17

1.2 The loading cycles of cyclic fatigue and cyclic dwell fatigue. In cyclic fatigue an equal amount of time is spent at every stress level, whereas in cyclic dwell loading the load 'dwells' in the state of maximum stress for an extended time period. . . . . 18

1.3 The Stroh model, adapted by Evans and Bache's group [6, 7]. Slip accumulates at the boundary between 'hard' and 'soft' grains which results in a stress concentration build up in the hard grain and crack nucleation. . 19

1.4 This figure shows two cartoons depicting a mechanism by which creep in Ti-alloys can be enhanced or reduced by the presence of point defects. (A) shows that if a substitutional defect such as Ni, Fe, or Co 'goes interstitial' it will enhance self-diffusion by increasing the number of vacancy-interstitial pairs. (B) shows that vacancies can be rendered immobile if the vacancy encounters a substitutional defect such as Mo and binds to it. If such a process is energetically favourable, then it would reduce the amount of creep deformation by immobilising vacancies. . . . . 21

2.1 The Kohn-Sham self-consistent energy minimisation procedure is started with an initial guess of the charge density. This charge density is used in a self-consistency cycle to generate an output density. If input and output densities do not agree to a high enough degree of precision, then a new density is generated and input into the next self-consistency cycle. This procedure repeats until self-consistency in the input and output charge densities is reached. Once this occurs the total energy is computed. It is worth noting that this is the procedure used for traditional density mixing DFT (see section 3.4), but there are alternative procedures that involve mixing potentials instead of densities, as well as ensemble DFT. . . . . 34

3.1 A schematic representation of the formation of energy bands. As the number of atoms that are brought into a crystal lattice configuration increases the number of available discrete states increases. In the limit of an infinite crystal lattice the energy separation between distinct states becomes vanishingly small and continuous energy bands form. . . . . 39

3.2 The density of states for $\alpha$-Ti computed using a primitive hexagonal close-packed unit cell of two Ti atoms. The red line at 0 eV is at the Fermi level. At this energy the occupancy is non-zero, which means that $\alpha$-Ti will have a partially filled band at the Fermi level and no band gap. . . . 40

3.3 The all-electron (AE) radial s-orbital wavefunctions for a Ti atom (broken lines) and the corresponding pseudo (PS) wavefunctions (solid lines). This plot was generated by CASTEP's on-the-fly pseudopotential generator [8]. The vertical black dotted line is the cut-off radius (1.8 $a_0 \approx 9.5 \times 10^{-11}$ m) for the pseudopotential. The functional form of the AE and PS wavefunctions agree for $r > r_c$. For $r < r_c$ the PS wavefunctions have fewer nodes and so are less oscillatory than the AE wavefunctions. . . . . 46

4.1 The unit cells I used to simulate hcp and bcc Ti. . . . . 48

4.2 The variation of the total energy with cut-off energy generated using the 12elPP, 10elPP, and 4elPP within CASTEP and VASP. The system I used was a primitive hcp unit cell of two Ti atoms. All total energies are shown as deviations from $E_\infty$, which was generated using the same system with a cut-off energy of 1000 eV. . . . . 50

4.3 The convergence of the total energy with **k**-point sampling. The abscissa is the first component $N_1$ of the $N_1 \times N_1 \times N_2$ MP sampling grid. $N_1$ and $N_2$ are chosen s.t. $N_1/N_2 \approx c/a$. Total energies $E_{tot}$ are expressed relative to the lowest total energy of the dataset $E_0$. The MP grid is also compared with the corresponding number of **k**-points in the irreducible Brillouin zone. . . . . 50

4.4 (A-D) The energy-volume curves computed using CASTEP for the hcp and bcc crystal structures simulated using the LDA and PBE exchange-correlation functionals. I used the USPP 12elPP to obtain the data shown in this figure. Each plot has its energy offset by the amount shown in the top-left corner of the plot. Both cells simulated were two-atom cells, so the volumes and energies can be compared directly. (E) The equilibrium $a$-lattice parameters in Å obtained from the energy-volume curves. . . . . 52

4.5 (A-D) The energy-volume curves computed using VASP for the hcp and bcc crystal structures simulated using the LDA and PBE exchange-correlation functionals. I used the PAW 10elPP to obtain the data shown in this figure. Each plot has its energy offset by the amount shown in the top-left corner of the plot. Both cells simulated were two-atom cells, so the volumes and energies can be compared directly. (E) The equilibrium $a$-lattice parameters in Å obtained from the energy-volume curves. . . . . 53

4.6 The variation of the total energy of a primitive unit cell of hcp-Ti with $c/a$ ratio computed using (A) CASTEP and (B) VASP. Both plots have their energy offset by the amount shown in the top-left corner of the plot. The points were fitted to quadratic polynomials of the $c/a$ ratio, with minima at (A) 1.580, and (B) 1.586. . . . . 54

4.7 The charge densities of (A) bulk fcc-Al on the (111) plane, and (B) bulk hcp-Ti on the (0001) basal plane. In both plots atoms are at the corners and centre. The straight black lines mark the edges where charge density plots were tiled in a periodic fashion to include an atom in the centre of the plot. They are not contours of constant charge. The contours of constant charge density are (A) $\{30, 30.5, 31, 31.5, 32\}$, and (B) $\{22, 22.5, 23, \ldots, 35\}$ in units of $10^{-3}$ e/$a_0^3$. Values for specific regions and contours have been indicated using arrows. . . . . 57

5.1 The (0001) basal, $(1\bar{1}00)$ prism, and $(01\bar{1}1)$ pyramidal I planes are shown in blue, red, and green respectively. . . . . 59

5.2 The stacking sequences of the (A) basal, (B) prism, and (C) pyramidal I 'superplanes' in $\alpha$-Ti. Small and large circles distinguish atoms on adjacent $(11\bar{2}0)$ planes. (A) and (C) from [2]. . . . . 60
5.3 The two stacking fault system geometries I used to simulate $\gamma$-surfaces are the (A) bulk (B) and slab geometries. Regions containing atoms are red/blue in the bulk/slab system, and regions of vacuum are white. Displaced regions are coloured darker than regions that are not displaced. See the text in section 5.1.3 for more details. . . . . 63
5.4 The basal (A), prism (B), and pyramidal I (D) $\gamma$-surfaces simulated using Ti0 [9]. In (C) a section of the prism $\gamma$-surface with a higher sampling density is plotted for a more detailed view of the $F_1$ stacking fault. Contour labels are in units of $mJ/m^2$. All heat plots use the colour scheme in the colour bar next to (D). (A) and (D) are based on Fig. 3(b) from [2] and Fig. 3 from [1] respectively. . . . . 65
5.5 The interplanar spacings through slabs of 8, 12 and 16 superplanes after constrained relaxations. (A) shows the 12elPP results, and (C) shows the 4elPP results. From [2]. . . . . 70
5.6 The $\gamma$-surface for the basal plane calculated with (A) DFT with the 12elPP and (B) Ti0 [9]. The maxima and minima are in the same locations for both surfaces, but the energies are generally lower in the Ti0 surface. All energies are shown in $mJ/m^2$. A contour spacing of 50 $mJ/m^2$ was used. The basal plane unit cell is highlighted in black. From [2]. . . 71
5.7 Pyramidal I $\gamma$-surfaces computed using (A) DFT with the 4elPP and (B) Ti0 [9]. All energies are expressed in $mJ/m^2$, and the contours are separated by 50 $mJ/m^2$. The difference between the DFT $\gamma$-surfaces computed with the 4elPP and 12elPP is plotted in (C), where the contours are separated by 10 $mJ/m^2$. Contours of negative energy are shown by broken lines. From [2]. . . . . 72
5.8 A section of the full DFT pyramidal I $\gamma$-surface shown in Fig. 5.7(A), with a refined contour spacing of 10 $mJ/m^2$. From this plot it is clear that the stationary point at [0.5,0.23] is a saddle point. . . . . 74
5.9 Two periods of the fully relaxed (A) unfaulted slab, (B) $I_1$ fault, (C) $I_2$ fault, viewed in projection along $[11\bar{2}0]$ obtained from 12elPP calculations. (A) Local atomic structures in the bulk and surface regions are specified by octahedra and tetrahedra labels 'o' and 't' respectively. Circle sizes follow the same scheme as in Fig. 5.3. (B) The fault structure in the $I_1$ fault region is specified by octahedra labels 'o'. (C) The fault structure in the $I_2$ fault region is specified by trigonal prisms and tetrahedra labels 'p' and 't' respectively. From [2]. . . . . 76
5.10 A line section of the 4elPP pyramidal $\gamma$-surface shown in Fig. 5.7(A) along the straight line between [0,0] and [0.5,0.5]. The point [0.5,0.5] on the $\gamma$-surface corresponds to a translation of $\frac{1}{3}[2\bar{1}\bar{1}3]$. From [2]. . . . . 77
5.11 The basal $\gamma$-surfaces of $\alpha$-Ti generated using the Ti-$\{1,2,3\}$ IPs and DFT. All energies are expressed in $mJ/m^2$, and contours are separated by 50 $mJ/m^2$. . . . . 80
5.12 The pyramidal I $\gamma$-surfaces of $\alpha$-Ti generated using the IPs and DFT. All energies are expressed in $mJ/m^2$, and contours are separated by 50 $mJ/m^2$. . . . . 81

5.13 The root-mean-square difference between samples of the IP and DFT $\gamma$-surfaces. (A) shows the RMS differences between $\gamma$-surface samples, and (B) shows the RMS differences with samples weighted by the Boltzmann factor in (5.5). . . . . 83
5.14 RMS differences between gradients of the IP and DFT $\gamma$-surfaces expressed as a percentage of the average slope of the corresponding DFT $\gamma$-surface. (A) shows the RMS gradient differences between $\gamma$-surfaces samples, and (B) shows the RMS gradient differences with samples weighted by the Boltzmann factor in (5.5). . . . . 84

6.1 The distinct bonds between atoms neighbouring the vacancy in $\alpha$-Ti. Bond lengths are shown as percentages of the corresponding equilibrium bond lengths $a = 2.94$ Å in the basal plane and $a' = 2.88$ Å out of the basal plane. The vacancy occupies a site of $C_{3v}$ symmetry. . . . . 91
6.2 (A) The minimum energy dumbbell structure of the Mo interstitial in red with Ti atoms in blue. The structure is shown as a projection along the $c$-axis of two adjacent basal planes of the $6 \times 6 \times 4$ supercell. Circles of the same size denote atoms in the same basal plane. The dumbbell has been outlined. There are two equivalent structures related to this one by a three-fold rotational symmetry about the $c$-axis (normal to the page). The distortion due to the Mo atom is highlighted by black lines between atoms parallel to the $[1\bar{2}10]$ perfect crystal direction. (B) A close-up of the Mo interstitial and the bond lengths between the defect and its nearest neighbours. . . . . 94
6.3 (A) The Mo substitutional atom (red circle) in $\alpha$-Ti (blue circles) showing bond lengths in the basal plane, shown as a percentage of the ideal bond length in the basal plane of $\alpha$-Ti. The relaxed defect configuration is located in a site of $C_{3v}$ symmetry, highlighted by green and brown shading, the same as a Ti atoms in $\alpha$-Ti. (B) Projection of the Mo substitutional along $[1\bar{1}00]$ with bond lengths shown as a percentage of ideal bond lengths in pure $\alpha$-Ti. The smaller circles are on adjacent planes along $[1\bar{1}00]$. . . . 94
6.4 (A) Neighbouring Mo substitutional atom (red) and vacancy defects in the same basal plane of $\alpha$-Ti. (B) Neighbouring Mo substitutional atom (red) and vacancy defects in adjacent basal planes. The Mo atom lies in the basal plane containing atoms represented by larger circles, and the vacancy in the basal plane containing atoms represented by smaller circles. All bond lengths are shown as percentages of the ideal lattice parameter $a = 2.94$ Å. . . . . 96

# List of Tables


4.1 The elastic constants for Ti in its hcp ($\alpha$) and bcc ($\beta$) bulk phases computed using DFT and experiment. All values are expressed in GPa. . . . . 54

5.1 The equilibrium cohesive energy and lattice parameters I computed using Ti0 [9]. The values are compared with those of Mendelev [10] computed using Ti0 and with experimental values. . . . . 62

5.2 Stacking fault energies (SFEs) generated using Ti0 [9] on the basal, prism and pyramidal I planes. I varied the number of atoms ($N$atoms) in the system used to compute each SFE in order to converge the system size. Energies are in units of mJ/m$^2$. See section 5.1.4 for more details. . . . . 66

5.3 Stacking fault energies computed using Ti0 [9] on the basal, prism, and pyramidal I planes. These are compared with results in the literature computed using central force (CF) potentials, interatomic potentials with angular dependence (A), as well as experimental data. All energies are shown in mJ/m$^2$. Positions mark coordinates on the $\gamma$-surfaces in Fig. 5.4. Based in part on Tables 1 and 2 from [1]. . . . . 66

5.4 DFT stacking fault energies generated on the basal and pyramidal I planes. I varied the number of atoms (Natoms) in the system used to compute each SFE in order to converge the system size. See section 5.2.2 for more details. . . . . 70

5.5 $I_2$ stacking fault energies on the basal plane computed in this work and elsewhere compared with experiment. All values quoted are DFT results apart from the results labelled tight-binding (TB) or Experiment. DFT results are labelled according to the number of valence electrons used in the pseudopotential where this information is known. Based on Table 1 from [2]. . . . . 73

5.6 The energies and $\gamma$-surface positions of the $I_1$ and $I_2$ intrinsic faults for the pyramidal I plane computed with DFT and three pseudopotentials, and with Ti0 [9]. 'Full' indicates an unconstrained ionic relaxation allowing atomic displacements parallel and normal to the fault plane. 'Con' indicates a constrained ionic relaxation allowing displacements only normal to the fault plane. The energies quoted for the $I_2$ fault with constrained DFT relaxation are for the unstable saddle point configuration in the $\gamma$-surface, which becomes a local minimum with full DFT relaxation. All energies in mJ/m$^2$. Based on Table 2 from [2]. . . . . 75

5.7 Stable SFEs and their positions on the basal and pyramidal I $\gamma$-surfaces computed using the IPs and DFT. All energies are expressed in mJ/m$^2$. All positions are expressed as fractions of the lattice vectors along the $x$- and $y$-axes of the $\gamma$-surfaces in Figs. 5.11 and 5.12. . . . . 79

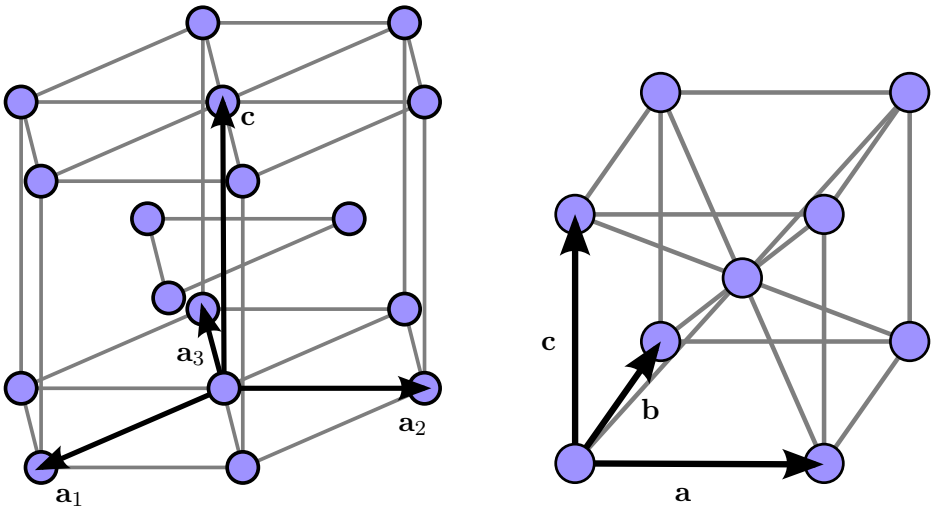
6.1 Vacancy formation energies ($E^{\mathrm{f}}$) in $\alpha$-Ti and cohesive energies ($E^{\mathrm{coh}}$) of the perfect hcp crystal in eV computed for different supercell sizes. MP mesh is the Monkhorst-Pack mesh of **k**-points. kp×atom is the number of **k**-points multiplied by the number of atoms in the supercell used for comparisons between the **k**-point sampling for different supercells. . . . . 88
6.2 Self-interstitial formation energies in $\alpha$-Ti computed as part of this study and compared with those of Vérité *et al.* [11]. . . . . 88
6.3 Vacancy formation energies in Ti from DFT using different exchange-correlation functionals (PBE, PBEsol PW91 and LDA), tight-binding (TB), and experiment. All formation energies are shown in eV. The estimate calculated from the results of Köppers *et al.* [12] and Shang *et al.* [13] is discussed in section 6.2. . . . . 90
6.4 Relaxed formation energies of six Mo interstitial configurations in $\alpha$-Ti, and of Mo substitutional atoms in $\alpha$- and $\beta$-Ti. The last two rows show binding energies between a Mo substitutional atom and a vacancy in $\alpha$-Ti (Mo - Vac in $\alpha$-Ti) in the same basal plane and adjacent basal planes. (Positive binding energies correspond to defects that are attracted to each other). . . . . 93

# Chapter 1

# Introduction

Titanium and its alloys are a broad category of metallic materials primarily used for structural applications. Their main application is in the aerospace industry owing to their high specific strength, and their resistance to fatigue and corrosion [14, p. 15]. Their mechanical properties can be modified significantly by the addition of alloying elements. One example is the Ti-alloy Ti-6Al-2Sn-4Zr-2Mo (Ti-6242), where the digits denote weight percentages (wt.%) of the alloying elements. The addition of 6 wt.% Al stabilises Ti's low temperature $\alpha$-phase, which has a hexagonal close-packed (hcp) crystal structure, whereas the 2 wt.% Mo stabilises Ti's high temperature body-centred cubic (bcc) $\beta$ phase (see Fig. 1.1). Sn and Zr do not stabilise either phase but instead modify the mechanical properties of the alloy via solute strengthening ([15] and [14, pp. 37-38]). The stabilisation of these two phases helps give Ti-6242 its high strength and fatigue resistance properties [16], which is why it is widely used to make the blades and disks in the high-pressure compressor of aerospace jet engines [16].

Despite these desirable properties as structural materials Ti-alloys with a high $\alpha$ phase fraction are susceptible to a fatigue failure mechanism called cold dwell fatigue (CDF). CDF was first discovered in the uncontained failure of the fan disk assemblies of two jet engines in late 1972 and early 1973 [17, 18]. Since then it has caused a number of jet engines to fail whilst in service on commercial flights [19–21]. Fortunately no deaths or serious injuries were sustained as all the engine failures occurred on or near the ground. All the failures were caused by the fatigue fracture of one of the disks of the high-pressure compressor 3-9 spool made from Ti-6242 and the failed disk in each case




(A) (B)

FIGURE 1.1: The hcp and bcc crystal structures are represented here by their conventional unit cells. The vectors $\{\mathbf{a}_1, \mathbf{a}_2, \mathbf{a}_3, \mathbf{c}\}$ in (A) and $\{\mathbf{a}, \mathbf{b}, \mathbf{c}\}$ in (B) are the Miller (Bravais) crystal lattice vectors for hcp and bcc respectively.

showed characteristic signs of CDF fracture. The components in question have been removed from service by a number of safety directives by the National Transportation Safety Board [20, 22].

The macroscopic conditions that cause CDF failure are now well known [23, Section 4(c)]. CDF failure is a fatigue failure mechanism that occurs over repeated loading cycles below the yield stress of the alloy. CDF loading cycles include a 'dwell' period, as shown in Fig. 1.2, in which the component or sample is held at the maximum stress level for an extended period of time during the cycle. This type of loading cycle is similar to the stresses experienced during a flight, which includes a large increase in stress during take-off, a lower stress-hold during cruising, and unloading during landing [24, 25].

Despite detailed knowledge of CDF at the macroscale a precise mechanistic origin of CDF failure is still unknown [23, Section 4(b)]. This uncertainty costs the aerospace industry millions in over-conservative design and extensive testing for each commercial aircraft [14, p. 279]. Because it is known that CDF can reduce the time to failure of susceptible alloys by more than an order of magnitude [26], susceptible components need to have their time in service reduced drastically to guarantee safe use. A detailed understanding of the mechanisms involved in CDF failure would address these problems allowing affected components to be designed lighter to save fuel, and to be used for more hours in service, saving the money and time needed for frequent replacements.

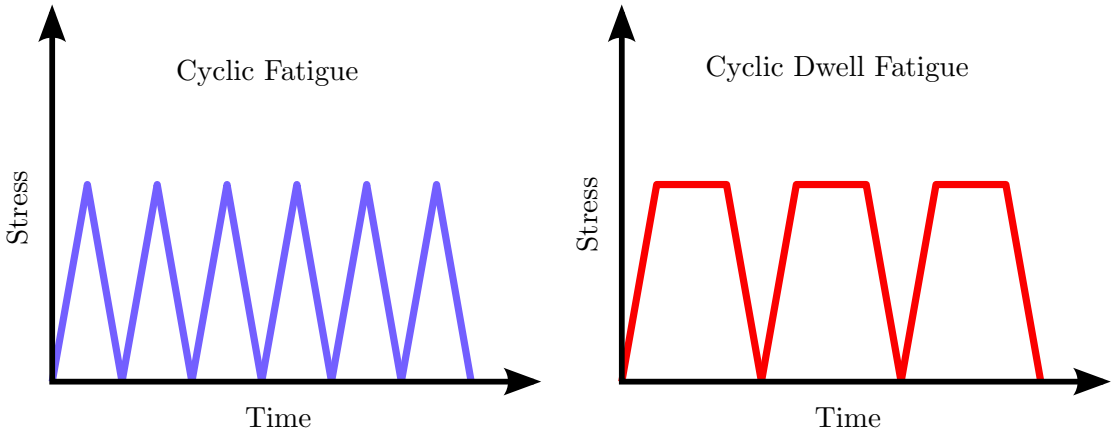



FIGURE 1.2: The loading cycles of cyclic fatigue and cyclic dwell fatigue. In cyclic fatigue an equal amount of time is spent at every stress level, whereas in cyclic dwell loading the load 'dwells' in the state of maximum stress for an extended time period.

The plastic deformation that causes CDF failure is due in part to Ti's unusual creep deformation behaviour at stresses as low as 60% of the yield stress[1], and at temperatures as low as room temperature[28, 29]. This creep deformation is often called 'cold creep' [30] and appears to involve the planar glide of dislocations in grains oriented suitably for slip ('soft' grains). These soft grains gradually become exhausted as load is transferred to grains unfavourably oriented for slip ('hard' grains). The planar nature of slip in Ti-alloys containing 6 wt.% Al during room temperature creep was shown [31] to be a result of short range ordering of Ti and Al atoms.

CDF failure also depends on load redistribution (a.k.a. load shedding) from soft to hard grains during low temperature creep [30]. Evans and Bache [24, 32] proposed a mechanism describing crack nucleation based on the Stroh model [33, 34]. This mechanism involves pile-ups of dislocations at the boundary between a soft $\alpha$ grain favourably oriented for slip and a hard $\alpha$ grain in which slip is difficult (see Fig. 1.3). The stress concentration ahead of the pile-up in the hard grain cannot be relieved by slip in the hard grain, so a crack nucleates. Failure occurs when the crack reaches a certain length.

At temperatures greater than 200 °C CDF is no longer a failure mechanism [14, p. 272]. Thus although creep leads to load shedding at temperatures possibly too low for diffusion, there must be some thermally activated process that relaxes stresses at temperatures above 200 °C.

The groups Zhang *et al.* [25] and Ozturk *et al.* [35] developed crystal plasticity models to

[1]The yield stress is usually defined as the flow stress at a strain of 0.002 [27].

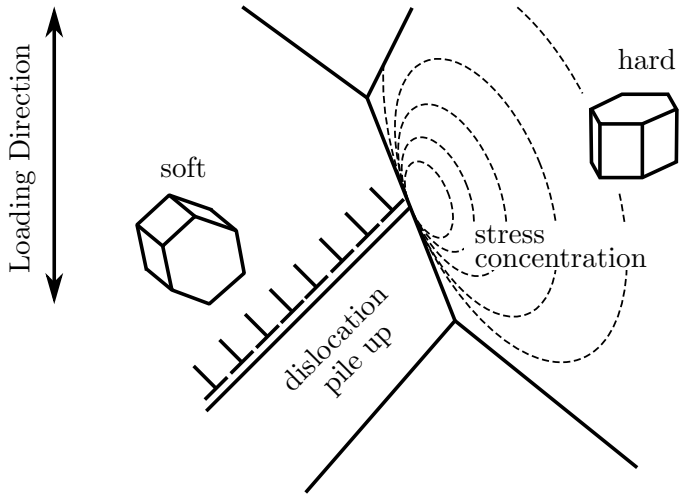



FIGURE 1.3: The Stroh model, adapted by Evans and Bache's group [6, 7]. Slip accumulates at the boundary between 'hard' and 'soft' grains which results in a stress concentration build up in the hard grain and crack nucleation.

study near $\alpha$ and $\alpha+\beta$ Ti-alloys and the temperature dependence of CDF. The model of Zhang *et al.* simulates Ti-6Al (the digit denotes 6 wt. % Al) assuming that dislocations in corresponding to all slip systems are pinned and then released by a thermally activated process with a common activation energy of $\Delta H$ and an attempt frequency $\nu$. Zhang *et al.* obtained their results by setting $\Delta H \approx 0.62$ eV and $\nu = 10^{11}$ s$^{-1}$. However the work does not explain the mechanistic origin of the activation energy $\Delta H$, nor the low attempt frequency compared with the Debye frequency of Ti in the range of $7.6 - 8.9 \times 10^{12}$ [36–38].

In contrast the model of Ozturk *et al.* simulates Ti-7Al (the digit denotes 7 wt. % Al) and Ti-6242 assuming that statistically stored dislocations are the cause of dislocation pinning. The authors use a power law to relate the statistically stored dislocation density to the resolved shear stress and slip rate for each slip system. Both models incorporated the temperature dependence of the critical resolved shear stresses of slip on the basal, prism, and pyramidal planes, as well as the temperature dependence of the anisotropic elastic constants.

Both groups use measurements of the critical resolved shear stress (CRSS) over a range temperatures carried out by Williams *et al.* [39] for single crystals of $\alpha$-Ti to calibrate their models. Both groups also applied a shift to each individual curve in Fig. 27 of Williams *et al.* [39] to better match the room temperature critical resolved shear stresses (CRSSs) for their system of interest. Zhang *et al.* shifted the curves so that the CRSS

values match the Ti-6Al values of Hasija *et al.*, and Ozturk *et al.* shifted the curves so that the CRSS values match the Ti-6242 values of Deka *et al.* [40] for their model of Ti-6242.

The models of both groups reproduced experimental creep data for single crystals and polycrystals, with the model of Zhang *et al.* also reproducing data for different strain rates. Both groups studied the effects of load shedding by considering a hard-soft grain boundary. For these studies Zhang *et al.* simulated Ti-6Al and Ozturk *et al.* simulated Ti-6242. They both found that under dwell loading conditions at temperatures below 230 °C a high stress concentration builds up at the hard-soft grain boundary. Above 230 °C the models of both groups predicted that this load shedding does not occur.

Both groups reached different conclusions about the temperature dependence of load shedding using their models. Zhang *et al.* found that their model predicted that load shedding was strongest at a temperature of about 120 °C under cyclic dwell loading with a stress hold. This is in agreement with experimental results from industry [25]. In contrast, Ozturk *et al.* found that the effects of load shedding decreased with temperature [35].

The two groups also reached different conclusions about the mechanism causing load shedding. The model of Zhang *et al.* predicted that load shedding is caused by the temperature sensitivity of the strain rate sensitivity in Ti-6Al. Zhang *et al.* found that this strain rate sensitivity was exacerbated by using dwell loading compared with conventional cyclic loading. In contrast Ozturk *et al.* concluded from the results of their model that load shedding is caused by the plastic anisotropy of Ti-6242. Their results showed that this anisotropy was temperature dependent and weakened with increasing temperature. However, because their results were all carried out at the using one strain rate they did not assess the role that strain rate plays in their model.

It is possible that the activation energy $\Delta H$ used by Zhang *et al.* in their crystal plasticity model corresponds to a process involving point defects in the Ti lattice. Point defects in Ti and its alloys are well-known to play an important role in affecting their plastic deformation behaviour [41]. An example is the effect of Fe and Ni impurities, which are hard to remove from Ti due to the way Ti is produced via the Kroll process [14, p. 56]. These impurities as well as Co are known to significantly increase the

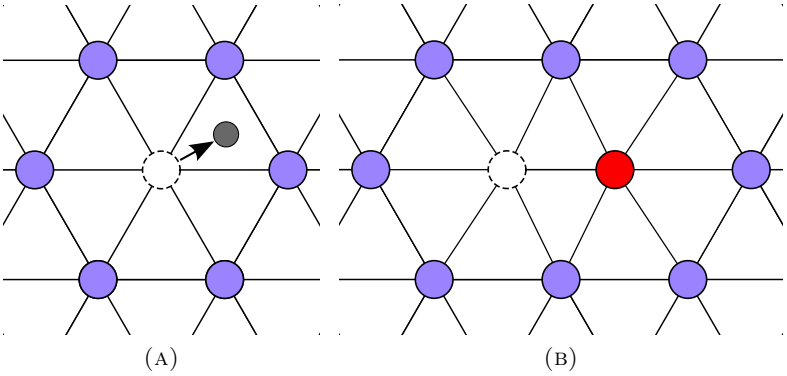



FIGURE 1.4: This figure shows two cartoons depicting a mechanism by which creep in Ti-alloys can be enhanced or reduced by the presence of point defects. (A) shows that if a substitutional defect such as Ni, Fe, or Co 'goes interstitial' it will enhance self-diffusion by increasing the number of vacancy-interstitial pairs. (B) shows that vacancies can be rendered immobile if the vacancy encounters a substitutional defect such as Mo and binds to it. If such a process is energetically favourable, then it would reduce the amount of creep deformation by immobilising vacancies.

rate of self-diffusion in Ti-alloys by becoming interstitial defects, thus creating vacancy-interstitial complexes that contribute to self-diffusion [42]. This process is shown in Fig. 1.4(A). These Frenkel defects outnumber the intrinsic vacancy concentration and dominate self-diffusion, hence diffusion is possible at low temperatures.

The effect of these impurities on self-diffusion has been well studied experimentally. Herzig [43] found the activation energy for self-diffusion in commercially pure Ti to be $\approx$ 2.00 eV, whilst in contrast Köppers *et al.* [12] found that much purer Ti with less than 1 weight parts per million Fe, Co, and Ni had an activation energy of 3.14 eV in the temperature range 560-860 °C. This is almost certainly the activation energy of self-diffusion in pure $\alpha$-Ti, and so the difference between these activation energies demonstrates the effect of Fe, Co, and Ni impurities on the self-diffusion properties of Ti. Whilst these impurities have a significant effect on self-diffusion both activation energies are larger than 0.62 eV of Zhang *et al.* [25], and so cannot be the mechanism responsible for the cold creep leading to CDF failure.

A possible clue to eliminating CDF is the experimental observation that Ti-alloy Ti-6Al-2Sn-4Zr-2Mo (Ti-6242) and Ti-alloy Ti-6Al-2Sn-4Zr-6Mo (Ti-6246) have very different CDF susceptibilities [26]. As mentioned earlier in this chapter, Ti-6242 is highly susceptible to CDF, whereas Ti-6246 is not [26]. The most significant difference between them is Ti-6246 has 4 weight percent more Mo than Ti-6242.

Qiu *et al.* [26] looked at Ti-624X, X=2,3,4,5,6, and their CDF susceptibilities. They attributed the differing CDF susceptibilities of Ti-6242 and Ti-6246 in part to the higher $\beta$ phase fraction in Ti-6246. Since CDF doesn't occur in the $\beta$ phase [44] this reduces the probability of CDF failure. However, in Ti-6246 there is a 60% $\alpha$ phase fraction, suggesting that Mo is doing more to suppress CDF failure besides increasing the $\beta$ phase fraction. Qiu *et al.* also observed that the increasing Mo content from Ti-6242 to Ti-6246 leads to an increasingly random distribution of $\alpha$ grain orientations, as well as a decreasing average $\alpha$ grain size. The authors argue that both the orientation and size distributions of $\alpha$ grains are have a strong effect on the CDF susceptibility.

Mo could also reduce CDF susceptibility by reducing the creep rate in the $\alpha$ phase of Ti at the point defect length-scale. At this length-scale creep can be enhanced by the presence of mobile vacancies in the $\alpha$-Ti lattice. If a significant concentration of Mo substitutional defects and Ti-vacancies can reduce the free energy of the system by binding to each other, then Mo might reduce the creep rate by rendering vacancies immobile (see Fig. 1.4). In chapter 6 of this thesis I will show that this is not the case.

To test the above hypothesis I used density functional theory (DFT) calculations to compute the formation and binding energies of a range of Mo and intrinsic point defects. Computer simulations such as DFT are ideal for probing these systems because a wide range of parameters can be controlled compared with experiment. For example, the precise positions of all the atoms can be specified in a computer simulation relatively easily, allowing a wide range of geometries to be set up and studied in order to find the most stable structure [45, section 6].

DFT was used because it explicitly treats the electronic structure of the system, leading to a more accurate treatment than approaches where electronic structure is treated implicitly through fitting procedures such as interatomic potentials (IPs). This is particularly important for accurately predicting the properties of Ti as changes in the treatment of the $s$, $p$, and $d$ valence states of Ti have been shown to significantly affect the description of equilibrium crystal structures [46].

Even computing ground-state properties of large systems using DFT is a computationally demanding task. Not only do DFT simulations generally require more computational resources than IP simulations, but the resources required can also scale as rapidly as

$\mathcal{O}(n^3)$, where $n$ is the number of atoms [47, section 10.5]. In contrast IPs such as Finnis-Sinclair potentials [48] scale linearly with system size as $\mathcal{O}(n)$. Thus despite IPs being less accurate than DFT in general, they have a low computational cost and can be used to simulate much larger systems than DFT. Hence they are an ideal tool for testing and developing methods in preparation for using DFT calculations.

After the introduction in chapter 1 density functional theory (DFT) and its use in metals are described in chapters 2 and 3 respectively. These chapters provide an overview of how the DFT calculations described in this thesis have been carried out, and how one can perform DFT calculations to determine the properties of metal solids.

Chapter 4 summarises tests of the DFT method I carried out on the bulk hcp and bcc phases of Ti. I used these tests to establish the accuracy of the DFT models and to better understand the bulk properties of Ti in these phases. I then used the DFT models to investigate directional bonding in hcp-Ti by comparing the charge densities of hcp-Ti and face-centred cubic Al.

In chapter 5 I summarise a study carried out on stacking fault energies and $\gamma$-surfaces in $\alpha$-Ti. The first section summarises interatomic potential (IP) calculations I used as a computationally inexpensive method to learn how to simulate isolated stacking faults in $\alpha$-Ti. These studies helped to reduce the number of DFT calculations in the second section of this chapter, and thus provided a significant saving of computational resources. The second section summarises DFT simulations I carried out to compute $\gamma$-surfaces for $\alpha$-Ti. The main result of these simulations is the full pyramidal I $\gamma$-surface shown in Fig. 5.7(A). The pyramidal I $\gamma$-surface is a useful tool for understanding $\mathbf{c} + \mathbf{a}$ slip, and hence plastic deformation in $\alpha$-Ti. I also computed properties of the pyramidal I $\gamma$-surface using two different pseudopotentials to assess their suitability for simulating $\gamma$-surfaces in $\alpha$-Ti. Finally in the third section I used the DFT $\gamma$-surface data to test a newly developed set of Ti IPs by Mendelev *et al.* [49].

Chapter 6 contains the main result of the thesis. In this chapter I show that the mechanism of Mo binding to vacancies does not suppress the creep rate in Ti-alloys, and so does not significantly affect the CDF susceptibility of Ti-alloys. I also summarise the formation energies of intrinsic and extrinsic Mo point defects in $\alpha$ and $\beta$-Ti and discuss their atomic and electronic structure. The chapter also contains a detailed discussion of the role of the vacancy in $\alpha$-Ti. The chapter concludes with discussions of the role

of Mo in affecting CDF susceptibility in Ti-6242 and Ti-6246, and a suggestion for how CDF gets its characteristic temperature dependence.

Finally the thesis is concluded in chapter 7 which summarises the main results from chapters 4, 5, and 6. This includes results pertaining to the pyramidal I $\gamma$-surface and the tests of the hypothesis described in this chapter. Chapter 7 also suggests further research that could be carried out, which builds upon the work described in this thesis.

# Chapter 2

# Density functional theory

Quantum mechanics is the most successful approach so far for describing the physics of electronic and atomic systems. The range of applications for this branch of physics includes some of the biggest technological breakthroughs of the 20th century such as the transistor [50, Vol. III, ch. 14-6], the basis of all modern computers, and the laser [50, Vol. I, ch. 5-3], which in the form of fibre-optic technology forms the backbone of telecommunication networks worldwide [51].

The main difficulty of using quantum mechanics to describe many-electron systems is that it is very computationally intensive. Small systems such as the hydrogen atom can be solved analytically with a pen-and-paper calculation, but describing the wavefunction of a many-electron system requires a set of Slater determinants which scales combinatorially with the number of particles [52, 53].

The most widely used quantum mechanical methods are those based on density functional theory (DFT), and the computational approaches that resulted from it [54]. DFT is so called because it treats the electronic charge density as the principle variable rather than the many-electron wavefunction. The charge density is a much simpler object, but it holds enough information within DFT to determine all the useful physical properties of any quantum mechanical system.

## 2.1 The Schrödinger equation

Understanding many quantum mechanical systems amounts to obtaining an accurate description of the stationary states of the system. These can be obtained for a system of atoms or molecules by solving the time-independent Schrödinger equation shown below:

$$\hat{H}\tilde{\Psi} = E\tilde{\Psi}, \tag{2.1}$$

where the operator $\hat{H}$ called the Hamiltonian is defined as:

$$\hat{H} = \Bigg[ -\sum_i \frac{1}{2m_\mathrm{e}}\nabla_i^2 - \sum_\alpha \frac{1}{2m_\alpha}\nabla_\alpha^2 - \sum_{i,\alpha} \frac{Z_\alpha e^2}{4\pi\epsilon_0|\mathbf{r}_i - \mathbf{r}_\alpha|} + \sum_{i>j} \frac{e^2}{4\pi\epsilon_0|\mathbf{r}_i - \mathbf{r}_j|} + \sum_{\alpha>\beta} \frac{Z_\alpha Z_\beta e^2}{4\pi\epsilon_0|\mathbf{r}_\alpha - \mathbf{r}_\beta|} \Bigg]. \tag{2.2}$$

The time-independent Schrödinger equation shown in (2.1) is a partial differential equation describing the energy contributions from all the particles in the system and their interactions. Here all terms that depend upon the electrons' positions $\{\mathbf{r}_i\}$ are shown using roman letters $i, j, \ldots$, and all terms that depend upon the positions of the nuclei $\{\mathbf{r}_\alpha\}$ are shown using greek letters $\alpha, \beta, \ldots$. Thus the first two terms in the right-hand side bracket are the kinetic energy terms of the electrons and the nuclei respectively. The next three terms are Coulomb electrostatic potential energies between electrons and nuclei, between just the electrons, and between just the nuclei respectively.

A solution of (2.1) consists of a total energy of the system denoted by $E$, as well as a function $\tilde{\Psi} \equiv \tilde{\Psi}(\{\mathbf{r}_i\}, \{\mathbf{r}_\alpha\})$ called the wavefunction. This is a complex function of the positions of all the electrons and nuclei.

To simplify (2.1) it is convenient to rewrite it in natural or atomic units which set the electron mass $m_\mathrm{e}$, the electron charge $e$, Planck's reduced constant $\hbar$, and the Coulomb constant $1/(4\pi\epsilon_0)$ equal to unity. In these units the Hamiltonian can be written as:

$$\hat{H} = \left[ -\sum_i \frac{1}{2}\nabla_i^2 - \sum_\alpha \frac{1}{2m_\alpha}\nabla_\alpha^2 - \sum_{i,\alpha} \frac{Z_\alpha}{|\mathbf{r}_i - \mathbf{r}_\alpha|} + \sum_{i>j} \frac{1}{|\mathbf{r}_i - \mathbf{r}_j|} + \sum_{\alpha>\beta} \frac{Z_\alpha Z_\beta}{|\mathbf{r}_\alpha - \mathbf{r}_\beta|} \right]. \tag{2.3}$$

## 2.2 The Born-Oppenheimer approximation

The computational difficulty posed by the time-independent Schrödinger equation is due to two characteristics of the problem it represents. The first is that it is a many-body problem, where the energy of any single particle depends on its interactions with all the others in the system. The second is the large number of particles involved, all being described in a quantum mechanical framework, resulting in a large number of degrees of freedom to be accounted for [47, 1.3]. These problems can be partially alleviated by making use of the Born-Oppenheimer approximation.

The approximation is usually justified by observing that the nuclei are almost 2000 times heavier than the electrons but experience forces of similar magnitude. Hence it can be argued they will also have momenta of similar magnitude. This means that the electrons move much faster than the nuclei, and thus when any nucleus is moved the electrons can respond and relax to their ground-state almost instantly. Following this motivation the wavefunction is approximated as a product of an electronic wavefunction $\Psi$ and a nuclear wavefunction $\Phi$:

$$\tilde{\Psi}(\{\mathbf{r}_i\},\{\mathbf{r}_\alpha\}) = \Psi(\{\mathbf{r}_i\};\{\mathbf{r}_\alpha\})\Phi(\{\mathbf{r}_\alpha\}). \tag{2.4}$$

The form of $\Psi(\{\mathbf{r}_i\};\{\mathbf{r}_\alpha\})$ shows that it is a function of the electron coordinates $\{\mathbf{r}_i\}$ only, with the nuclear coordinates $\{\mathbf{r}_\alpha\}$ acting only as fixed parameters. Substituting (2.4) into (2.1) results in the equations of motion in (2.6) and (2.7). Here we have discarded all terms proportional to $\nabla_\alpha\Psi$ and $\nabla_\alpha^2\Psi$ in (2.5) to obtain (2.6), assuming that the derivative of $\Psi$ with respect to the positions of the nuclei is small. It has been shown that the first of these derivative terms strictly vanishes, and that the second term is proportional to $1/m_\alpha$, thus justifying this approximation [55].

$$\left[-\sum_\alpha \frac{1}{2m_\alpha}\nabla_\alpha^2 + \mathcal{E}\right]\Phi - \sum_\alpha \frac{1}{2m_\alpha}\left[2\nabla_\alpha\Phi\cdot\nabla_\alpha\Psi + \Phi\nabla_\alpha^2\Psi\right] = E\Phi \tag{2.5}$$

$$\rightarrow \quad \left[-\sum_\alpha \frac{1}{2m_\alpha}\nabla_\alpha^2 + \mathcal{E}\right]\Phi = E\Phi \tag{2.6}$$

$$\hat{H}_\mathrm{e}\Psi = \left[-\sum_i \frac{1}{2}\nabla_i^2 - \sum_{i,\alpha}\frac{Z_\alpha}{|\mathbf{r}_i-\mathbf{r}_\alpha|} + \sum_{i>j}\frac{1}{|\mathbf{r}_i-\mathbf{r}_j|} + \sum_{\alpha>\beta}\frac{Z_\alpha Z_\beta}{|\mathbf{r}_\alpha-\mathbf{r}_\beta|}\right]\Psi = \mathcal{E}\Psi. \tag{2.7}$$

We have also defined $\mathcal{E}$ which collects all the electronic terms into (2.7) in the form of

an electronic time-independent Schrödinger equation with electronic Hamiltonian $\hat{H}_{\mathrm{e}}$. Written in this form it is clear that the motion of the electrons is decoupled from the motion of the nuclei. The electrons only affect the motion of the nuclei in (2.6) the term $\mathcal{E} \equiv \mathcal{E}(\{\mathbf{r}_\alpha\})$ called the Born-Oppenheimer potential energy surface. Because the nuclei typically behave like classical point particles under most conditions [55, pp. 200-203] Newtonian mechanics can be used to solve for the nuclear degrees of freedom in (2.6).

## 2.3 The Hohenberg-Kohn Theorems

The Born-Oppenheimer approximation simplifies solving the time-independent Schrödinger-equation explicitly by decoupling the equations of motion of the nuclei and the electrons. When the approximation is applied the main difficulty lies in solving the all-electron time-independent Schrödinger equation shown in (2.7). Under the Born-Oppenheimer approximation the Coulomb interaction between the nuclei is a constant when solving for the electronic ground-state, and so can be ignored, and the Coulomb interaction between the electrons and the nuclei is a static external potential acting on the electrons defined as:

$$V_{\mathrm{ext}}(\mathbf{r}) = -\sum_{\alpha} \frac{Z_\alpha}{|\mathbf{r} - \mathbf{r}_\alpha|}. \tag{2.8}$$

Hence we can redefine the electronic Schrödinger equation in terms of this external potential as:

$$\begin{aligned} \hat{H}_{\mathrm{e}}\Psi &= [\hat{F} + \hat{V}_{\mathrm{ext}}]\Psi = \mathcal{E}\Psi, \\ \hat{F} &= \left[ -\sum_i \frac{1}{2}\nabla_i^2 + \sum_{i>j} \frac{1}{|\mathbf{r}_i - \mathbf{r}_j|} \right], \\ \hat{V}_{\mathrm{ext}} &= \sum_i V_{\mathrm{ext}}(\mathbf{r}_i). \end{aligned} \tag{2.9}$$

The way in which this equation is solved using DFT starts with the statement of two theorems proved by Hohenberg and Kohn in 1964 [56]. These two theorems propose solving the many-electron Schrödinger equation such that the principle object being varied is not the wavefunction $\Psi$, but the density $n$. This can be defined in terms of $\Psi$ as:

$$n(\mathbf{r}) = \int \prod_{i=2} d^3\mathbf{r}_i |\Psi(\mathbf{r}, \mathbf{r}_2, \ldots, \mathbf{r}_N)|^2. \tag{2.10}$$

As a function of just 3 variables compared with the $3N$ needed to describe $\Psi$, the density is a much simpler object. The potential savings in terms of computational effort by making this switch is significant. The Hohenberg-Kohn theorems can be stated as:

- The external potential $V_{\text{ext}}(\mathbf{r})$, and thus any observable, is a unique functional of the ground-state electron density $n_0(\mathbf{r})$.
- The ground-state energy can be obtained using a variational principle and functional for the density. The density that minimises the total energy functional is the exact ground-state density.

We can prove the first Hohenberg-Kohn theorem by first assuming that, in contradiction with the statement of the theorem, there exists another external potential $V'_{\text{ext}}(\mathbf{r})$ with ground-state wavefunction $\Psi'_0$ corresponding to the same ground-state density $n_0(\mathbf{r})$. This defines two different Hamiltonians $\hat{H} = \hat{F} + \hat{V}_{\text{ext}}$ and $\hat{H}' = \hat{F} + \hat{V}'_{\text{ext}}$ each with a ground-state energy of $E_0 = \int \Psi_0 \hat{H} \Psi_0 d^3\mathbf{r}$ and $E'_0 = \int \Psi'_0 \hat{H}' \Psi'_0 d^3\mathbf{r}$ respectively. By using the ground-state wavefunction $\Psi_0$ as the trial wavefunction for $\hat{H}'$ and $\Psi'_0$ as the trial wavefunction for $\hat{H}$ along with the variational principle we get:

$$\begin{aligned} E_0 &< \int \Psi'_0 \hat{H} \Psi'_0 d^3\mathbf{r} = \int \Psi'_0 \hat{H}' \Psi'_0 d^3\mathbf{r} + \int \Psi'_0 (\hat{H} - \hat{H}') \Psi'_0 d^3\mathbf{r} \\ E'_0 &< \int \Psi_0 \hat{H}' \Psi_0 d^3\mathbf{r} = \int \Psi_0 \hat{H}' \Psi_0 d^3\mathbf{r} + \int \Psi_0 (\hat{H}' - \hat{H}) \Psi_0 d^3\mathbf{r}. \end{aligned} \tag{2.11}$$

Because both of these systems correspond to the same ground-state density both of the right-hand terms can be written in terms of the ground-state density using (2.9) which gives:

$$\begin{aligned} E_0 &< E'_0 + \int n_0 (\hat{V}_{\text{ext}} - \hat{V}'_{\text{ext}}) d^3\mathbf{r} \\ E'_0 &< E_0 - \int n_0 (\hat{V}_{\text{ext}} - \hat{V}'_{\text{ext}}) d^3\mathbf{r}. \end{aligned} \tag{2.12}$$

Adding both of these inequalities together results in the contradiction:

$$E_0 + E'_0 < E_0 + E'_0. \tag{2.13}$$

Using this result the ground-state density uniquely defines an external potential $V_{\text{ext}}$. The ground-state density also defines the number of electrons $N$ which uniquely defines

$\hat{F}$. Hence the Hamiltonian $\hat{H}_e$ all observables are unique functionals of the ground-state density.

This means that for all densities $n(\mathbf{r})$ that are the ground-state density for some external potential ($v$-representable) we can define the functional $F[n] = \int d^3\mathbf{r}\Psi_0^*(\mathbf{r})\hat{F}\Psi_0(\mathbf{r})$, since both $\Psi_0$ and $\hat{F}$ are defined by $n(\mathbf{r})$ (uniquely for non-degenerate ground-states). Using this definition a total energy functional can be defined for a potential $V(\mathbf{r})$ unrelated to the external potential $V_{\text{ext}}(\mathbf{r})$ given by $n(\mathbf{r})$, in terms of $n(\mathbf{r})$:

$$E_V[n] = F[n] + \int d^3\mathbf{r}V(\mathbf{r})n(\mathbf{r}). \tag{2.14}$$

The proof of the second Hohenberg-Kohn theorem relies on the variational principle of quantum mechanics. This states that for a Hamiltonian $\hat{H}$ and a normalised wavefunction $\Psi$ we can define an energy functional:

$$E_V[\Psi] = \int d^3\mathbf{r}\Psi^*(\mathbf{r})\hat{H}\Psi(\mathbf{r}) \tag{2.15}$$

such that $E[\Psi] \geq E_0$, where $E_0$ is the ground-state energy of $\hat{H}$. Equality is reached only when $\Psi$ is equal to the ground-state wavefunction $\Psi_0$. Using the result of the first Hohenberg-Kohn theorem a given electron density $n(\mathbf{r})$ determines an external potential $V_{\text{ext}}(\mathbf{r})$, for which it is the ground-state density, and also a ground-state $\Psi(\mathbf{r})$. We can use this wavefunction as a trial wavefunction for the Hamiltonian $\hat{H}$ constructed using the external potential $V(\mathbf{r})$ unrelated to $V_{\text{ext}}(\mathbf{r})$ in (2.14):

$$\begin{aligned}\int d^3\mathbf{r}\Psi^*(\mathbf{r})\hat{H}\Psi(\mathbf{r}) &= \int d^3\mathbf{r}\Psi^*(\mathbf{r})\hat{F}\Psi(\mathbf{r}) + \int d^3\mathbf{r}\Psi^*(\mathbf{r})\hat{V}\Psi(\mathbf{r}) \\ &= F[n] + \int d^3\mathbf{r}V(\mathbf{r})n(\mathbf{r}) = E_V[n] \geq E_0. \end{aligned} \tag{2.16}$$

The last inequality is given by the variational principle. Hence we have a new variational principle given by the new inequality $E_V[n] \geq E_0$ where equality is reached only if $n$ is the ground-state density for the external potential $V(\mathbf{r})$. The ground-state can thus be computed by minimising the functional $E_V[n] \geq E_0$ over all possible $v$-representable densities.

## 2.4 The Kohn-Sham equations

The Hohenberg-Kohn theorems show that there exists a variational method for finding the ground-state of a many-electron system by minimising the total energy functional $E_{\mathrm{V}}[n]$ in (2.14). However it does not define part of the total energy functional, $F[n]$, and so this must be approximated in order to take advantage of the results of these theorems.

The method of Kohn and Sham [57] can be used to do this by mapping the problem of many interacting electrons to the much simpler non-interacting problem. The non-interacting 'electrons' created by this mapping are not real, nonetheless they can still be used to compute the ground-state density, and hence the ground-state energy of the interacting many-electron system.

We first write the corresponding variational problem for the Hohenberg-Kohn total energy functional $E[n] = E_{\mathrm{V}}[n]$ in (2.14) for the external potential $V = V_{\mathrm{ext}}(\mathbf{r})$ with a Lagrange multiplier $\mu$ used to constrain the number of electrons $N$:

$$\delta\left[F[n] + \int d^3\mathbf{r} V_{\mathrm{ext}}(\mathbf{r}) - \mu\left(\int d^3\mathbf{r} n(\mathbf{r}) - N\right)\right] = 0. \tag{2.17}$$

Kohn and Sham chose to separate $F[n]$ in the following way:

$$F[n] = T_{\mathrm{s}}[n] + \frac{1}{2}\int d^3\mathbf{r} d^3\mathbf{r}' \frac{n(\mathbf{r})n'(\mathbf{r})}{|\mathbf{r}-\mathbf{r}'|} + E_{\mathrm{xc}}[n] \tag{2.18}$$

where $T_{\mathrm{s}}[n]$ is the kinetic energy of a system of non-interacting electrons with density $n(\mathbf{r})$. The middle term is the Hartree energy $V_{\mathrm{H}}[n]$, which accounts for the classical electrostatic interactions of the electrons with the same density $n(\mathbf{r})$. The last term gathers together the non-classical electron interactions as well as the difference between the interacting and non-interacting electron kinetic energies and is called the exchange-correlation functional $E_{\mathrm{xc}}[n]$. The reason for this separation is that the first two terms can be computed in quite a straightforward way, whereas the last term only accounts for a small part of the total energy in general. We shall see that there are surprisingly good approximations for the exchange-correlation functional.

By using the separation of (2.18) we can rewrite the variational problem as:

$$\frac{\delta T_s[n]}{\delta n(\mathbf{r})} + V_{KS}(\mathbf{r}) = \mu, \tag{2.19}$$

such that we have defined the Kohn-Sham potential $V_{KS}(\mathbf{r})$ as:

$$V_{KS}(\mathbf{r}) = \int d^3\mathbf{r}' \frac{n'(\mathbf{r})}{|\mathbf{r}-\mathbf{r}'|} + V_{\rm xc}(\mathbf{r}) + V_{\rm ext}(\mathbf{r}) \tag{2.20}$$

and the exchange-correlation potential $V_{\rm xc}[n]$ is defined as:

$$V_{\rm xc}(\mathbf{r}) = \frac{\delta E_{\rm xc}[n]}{\delta n(\mathbf{r})}. \tag{2.21}$$

The key result of rewriting the problem in this way is that (2.19) is the same form as a system of non-interacting particles moving in a potential $V_{KS}(\mathbf{r})$. Hence solving for the ground-state after this mapping consists of solving a set of single-electron Schrödinger equations called the Kohn-Sham equations:

$$\left[-\frac{1}{2}\nabla^2 + V_{KS}(\mathbf{r})\right]\psi_i = \epsilon_i \psi_i, \tag{2.22}$$

where the index $i$ runs over the single-particles states ($1 \ldots N/2$ for a spin-degenerate system at 0K such that single-particle states $\psi_i$ are doubly occupied). The electron density can then be constructed from the single-particle states $\psi_i(\mathbf{r})$ such that

$$n(\mathbf{r}) = 2\sum_{i=1}^{N/2} |\psi_i(\mathbf{r})|^2, \tag{2.23}$$

as can the non-interacting kinetic energy $T_s[n]$

$$T_s[n] = -\sum_{i=1}^{N/2} \int d^3\mathbf{r} \psi_i^*(\mathbf{r}) \nabla^2 \psi_i(\mathbf{r}). \tag{2.24}$$

The total energy is obtained from the Kohn-Sham eigenvalues $\{\epsilon_i\}$ as follows:

$$\begin{aligned} E[n] &= T_s[n] + \frac{1}{2}\int d^3\mathbf{r} d^3\mathbf{r}' \frac{n(\mathbf{r})n'(\mathbf{r})}{|\mathbf{r}-\mathbf{r}'|} + E_{\rm xc}[n] + \int d^3\mathbf{r} n(\mathbf{r}) V_{\rm ext}(\mathbf{r}), \\ &= 2\sum_{i=1}^{N/2} \epsilon_i - \frac{1}{2}\int d^3\mathbf{r} d^3\mathbf{r}' \frac{n(\mathbf{r})n'(\mathbf{r})}{|\mathbf{r}-\mathbf{r}'|} - \int d^3\mathbf{r} n(\mathbf{r}) V_{\rm xc}(\mathbf{r}) + E_{\rm xc}[n], \end{aligned} \tag{2.25}$$

taking into account the over counting of the Hartree energy and the exchange-correlation

energy of the Kohn-Sham eigenvalues compared with the fully-interacting picture. The form of the Kohn-Sham equations shown in (2.22) requires an initial guess for the electron density $n(\mathbf{r})$ in order that $V_{KS}(\mathbf{r})$ can be defined. Solution of the Kohn-Sham equations gives a set of single-particles states $\{\psi_i(\mathbf{r})\}$, which in turn defines a density as in (2.23). The same procedure could be applied with the new density, and the procedure could be repeated iteratively for all subsequent output densities. The problem will only be solved self-consistently when the input and output densities differ by a sufficiently small amount, at which point these densities define the ground-state density. The total energy can then be obtained by evaluating $E[n]$ in (2.25) with the self-consistent ground-state density. The self-consistency minimisation procedure is shown as a flow-chart in Fig. 2.1.

## 2.5 The exchange-correlation functional

In principle DFT is an exact theory which can be used to determine the ground-state configuration of any atomic system by mapping the full interacting many-body problem to a set single particles interacting with a mean field. However the main problem of DFT is that the exact form the exchange-correlation functional $E_{\mathrm{xc}}[n]$ in (2.18) is unknown. It must be approximated in all but the simplest cases using physical insight, experimental data, [58], and methods more accurate than DFT [59–61]. The first approximation and one of the most widely used is the local density approximation (LDA. [56, 62]):

$$E_{\mathrm{xc}}[n] = \int n(\mathbf{r})\epsilon_{\mathrm{xc}}\big(n(\mathbf{r})\big)d^3\mathbf{r}, \tag{2.26}$$

where $\epsilon_{\mathrm{xc}}\big(n(\mathbf{r})\big)$ is the XC-energy per particle of the homogeneous electron gas with a density $n(\mathbf{r})$. Transition metals pose two problems for the LDA that limit its accuracy in describing them. The first is that $d$-electrons are strongly affected by self-interaction errors, which are very significant in the LDA [63–65]. In addition $d$-bonding is localised and directional [66, ch. 9], which the LDA does not describe well. Both of these problems are dealt with better by generalised gradient approximations (GGAs) which tend to favour inhomogeneity more than the LDA and generally offer improved performance for transition metals [65, 67]. The two most widely used are parameterisations by Perdew-Burke-Ernzerhof (PBE, [68]) and that of Perdew and Wang (PW91, [69]). I have carried

out all calculations in this thesis with the PBE exchange-correlation functional, except where stated otherwise.

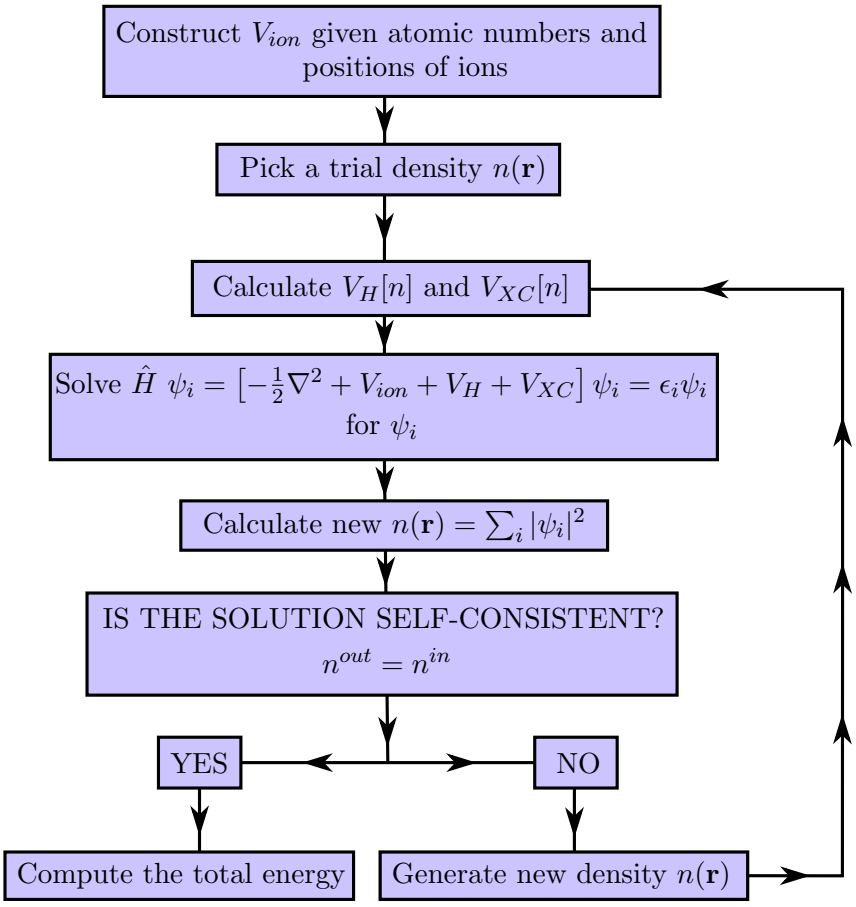



FIGURE 2.1: The Kohn-Sham self-consistent energy minimisation procedure is started with an initial guess of the charge density. This charge density is used in a self-consistency cycle to generate an output density. If input and output densities do not agree to a high enough degree of precision, then a new density is generated and input into the next self-consistency cycle. This procedure repeats until self-consistency in the input and output charge densities is reached. Once this occurs the total energy is computed. It is worth noting that this is the procedure used for traditional density mixing DFT (see section 3.4), but there are alternative procedures that involve mixing potentials instead of densities, as well as ensemble DFT.

# Chapter 3

# DFT for metals

Metals are a particularly difficult class of materials to simulate using DFT. The source of this difficulty is that metals do not have a band-gap in their band structure, unlike insulators and semiconductors [47, p. 28]. This means that there exists a Fermi surface that divides the occupied and unoccupied states in reciprocal space, which requires accurate sampling in order to be described correctly. Carrying out this sampling is much more computationally expensive than insulator and semiconductor calculations of systems with the same number of atoms. To cope with this a host of computational methods have been developed to improve the computational efficiency of DFT for calculating the ground-states properties of metals.

In this chapter I will summarise the methods that I have used to simulate metallic systems using DFT. This includes using finite temperature smearing and density mixing. I also used periodic boundary conditions with a plane-wave basis set plus ultrasoft and projector augment-wave pseudopotentials, methods that are not essential to the simulation of metals and can be used to model other classes of materials as well.

## 3.1 Reciprocal space and k-points

Because we are interested in metals which take on a crystalline structure in their solid form we would like to model atoms arranged in a periodic manner in space. The shape of the cell which can be repeated in space to generate the crystal structure is given

by three lattice vectors $\mathbf{a}$, $\mathbf{b}$, and $\mathbf{c}$. Examples for the hexagonal close-packed (hcp) and body centred cubic (bcc) crystal structures are shown in Fig. 1.1. When we solve the Schrödinger equation in this case Bloch's theorem applies [70]. A more detailed discussion of Bloch's theorem can be found in [71, ch. 8]. This states that the solution will take the form $\psi_{\mathbf{k}}(\mathbf{r}) = \exp(i\mathbf{k}\cdot\mathbf{r})u_{\mathbf{k}}(\mathbf{r})$ where $u_{\mathbf{k}}$ is periodic in the lattice vectors, i.e. $u_{\mathbf{k}}(\mathbf{r} + n_a\mathbf{a} + n_b\mathbf{b} + n_c\mathbf{c}) = u_{\mathbf{k}}(\mathbf{r})$, for all integers $n_a$, $n_b$, and $n_c$. $\mathbf{k}$ are the wave-vectors or $\mathbf{k}$-vectors labelling the eigenstates of the Schrödinger equation. It corresponds to a vector in reciprocal or $\mathbf{k}$-space.

The $u_{\mathbf{k}}$ have the same periodicity as the crystal lattice, which means that we can decompose it into a linear combination of periodic functions. One such set of periodic functions is the set of plane-waves $\exp(i\mathbf{G}\cdot\mathbf{r})$. The $\mathbf{G}$ are linear combinations of reciprocal lattice vectors $\{\mathbf{a}^*, \mathbf{b}^*, \mathbf{c}^*\}$ corresponding to the real-space lattice vectors $\{\mathbf{a}, \mathbf{b}, \mathbf{c}\}$. These are defined as

$$\mathbf{a}^* = 2\pi\frac{\mathbf{b}\times\mathbf{c}}{\mathbf{a}\cdot(\mathbf{b}\times\mathbf{c})}, \qquad \mathbf{b}^* = 2\pi\frac{\mathbf{c}\times\mathbf{a}}{\mathbf{a}\cdot(\mathbf{b}\times\mathbf{c})}, \qquad \mathbf{c}^* = 2\pi\frac{\mathbf{a}\times\mathbf{b}}{\mathbf{a}\cdot(\mathbf{b}\times\mathbf{c})}. \tag{3.1}$$

Hence when $\mathbf{G} = g_a\mathbf{a}^* + g_b\mathbf{b}^* + g_c\mathbf{c}^*$ for integers $g_a$, $g_b$, and $g_c$, $\mathbf{G}\cdot\mathbf{a} = 2\pi g_a$, $\mathbf{G}\cdot\mathbf{b} = 2\pi g_b$, etc. It is worth noting here that longer real space lattice vectors correspond to shorter reciprocal space lattice vectors and vice-versa. The decomposition takes the form:

$$u_{\mathbf{k}}(\mathbf{r}) = \sum_{\mathbf{G}} c_{\mathbf{k}+\mathbf{G}} \exp(i\mathbf{G}\cdot\mathbf{r}). \tag{3.2}$$

Applying Bloch's theorem to the single particle solutions to the Kohn-Sham equations in (2.22), our solutions can be expressed as $\psi_i = \psi_{n\mathbf{k}}$, where $n$ labels the band index and $\mathbf{k}$ labels the solution's corresponding $\mathbf{k}$-point or $\mathbf{k}$-vector. Plane-waves form a natural basis set for periodic functions such as wave-functions of crystals. It is common for DFT calculations to be carried out using plane-waves as a basis set to describe the wave-function. One of the advantages of doing this is that it is possible to solve the Schrödinger equation for each k-vector independently [47, 3.1.1]. This also applies to any quantity derived from these solutions such as the electron density.

In real space the smallest periodic repeat cell for a crystal is called the primitive unit cell. One such primitive unit cell is the Wigner-Seitz cell, and its reciprocal equivalent is called the first Brillouin zone, often shortened to just the Brillouin zone. The reason that

the Brillouin zone is important in plane-wave DFT calculations is that many important quantities are evaluated by integrating over the first Brillouin zone in reciprocal space. If the quantities to be integrated are slowly varying across the Brillouin zone then a weighted sampling over discrete points suffices to evaluate the whole integral accurately, and that is what is done in many DFT codes. Hence the discrete set of **k**-points chosen to sample reciprocal space usually lie within the first Brillouin zone.

A common method of sampling the Brillouin zone is the scheme of Monkhorst and Pack [72] involving the specification of a grid of $N_a \times N_b \times N_c$ points in total, where there are $N_a$ equally spaced points along the first reciprocal lattice vector $\mathbf{a}^*$, $N_b$ along $\mathbf{b}^*$, and $N_c$ along $\mathbf{c}^*$,. The use of a Monkhorst-Pack (MP) grid is equivalent to applying periodic boundary conditions to a supercell made up of $N_a \times N_b \times N_c$ unit cells. Conversely, running calculations with a supercell made up of a larger number of unit cells corresponds to a finer sampling of the first Brillouin zone. In this case fewer k-points are needed to achieve the same sampling density of the first Brillouin zone as using a single unit cell.

## 3.2 Cut-off energy

As stated in the previous section, solutions of the Schrödinger for periodic systems are constrained by Bloch's theorem to take the form $\psi_{\mathbf{k}}(\mathbf{r}) = \exp(i\mathbf{k}\cdot\mathbf{r})u_{\mathbf{k}}(\mathbf{r})$, where the $u_{\mathbf{k}}$ can be further expressed in terms of a linear combination of plane waves $\exp(i\mathbf{G}\cdot\mathbf{r})$ as shown in (3.2). When expressed in this way we can define our solutions to the Schrödinger equation as

$$\psi_{\mathbf{k}}(\mathbf{r}) = \sum_{\mathbf{G}} c_{\mathbf{k}+\mathbf{G}} \exp(i(\mathbf{k}+\mathbf{G})\cdot\mathbf{r}). \tag{3.3}$$

Since each of the **G** span the over the integers, computing $\psi_{\mathbf{k}}$ for each **k** involves an infinite sum over all the possible G-vectors. This infinite sum can be truncated by noting that each of the plane-waves in the sum of (3.3) corresponds to a solution of the Schrödinger equation with kinetic energy $E_{kinetic} = (1/2m)|\mathbf{k}+\mathbf{G}|^2$. This means that G-vectors with higher magnitudes correspond to higher kinetic energy solutions. When searching for ground-state solutions to the Schrödinger equation low energy solutions are more likely to be physically relevant than higher energy solutions. Hence it makes sense to remove those higher energy solutions from the minimisation by applying a kinetic

energy cut-off $(1/2)|\mathbf{k}+\mathbf{G}|^2 < E_{cut}$, or equivalently a G-vector cut-off $|\mathbf{k}+\mathbf{G}| < G_{cut}$ which constrains the number of G-vectors to sum over. Thus when the kinetic energy cut-off is applied the form of $\psi_{\mathbf{k}}$ reduces to

$$\psi_{\mathbf{k}}(\mathbf{r}) = \sum_{|\mathbf{k}+\mathbf{G}|<G_{cut}} c_{\mathbf{k}+\mathbf{G}} \exp(i(\mathbf{k}+\mathbf{G})\cdot\mathbf{r}). \tag{3.4}$$

The precision of the computed total energy increases with the cut-off energy for all plane-wave DFT calculations. However so does the computational time required to perform the calculation as well as the amount of memory needed to store the wavefunction. Convergence of this quantity to a value which provides the required precision and computational cost is essential to performing efficient plane-wave DFT calculations. The cut-off energy convergence tests I carried out for hcp-Ti are discussed in section 4.2.1.

## 3.3 The Fermi surface

A single hydrogen-like atom with only one electron and a nucleus has a number of discrete quantised states that the electron can occupy. Adding more electrons increases the number of possible electronic states further via angular momentum coupling [52, pp. 185-195 ].

If we arrange these many-electron atoms into an infinite crystalline arrangement then many new possible electronic states are created compared with the number of isolated atom states (see Fig. 3.1). The energy gap between many of the states decreases as the number of atoms increases, and in the limit of an infinite crystal lattice the states form continuous energy bands [52, pp. 442-447].

If all the electrons occupy their lowest energy or ground state configuration it is possible to define a state that has a 50% probability of being occupied. This state is called the Fermi level. At zero temperature (0 K) the Fermi level is the highest energy occupied state in a metal.

The Fermi level can be computed from the density of states, the occupation of electronic states as a function of energy, and integrating such that the integral equals the electron number. An example of the density of states for $\alpha$-Ti that I computed using DFT is shown in Fig. 3.2. The energy axis of this figure was scaled such that the Fermi level is

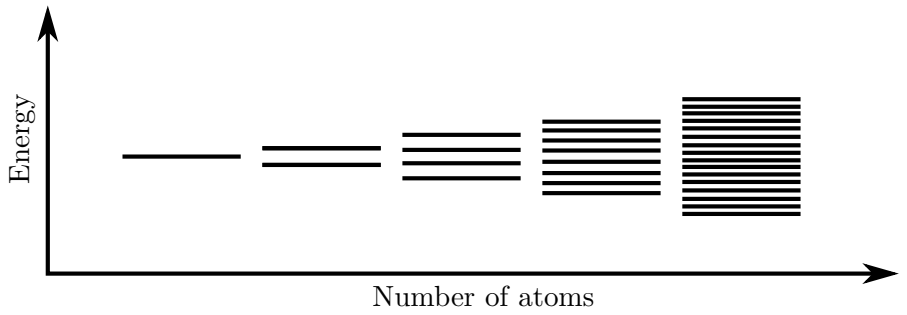



FIGURE 3.1: A schematic representation of the formation of energy bands. As the number of atoms that are brought into a crystal lattice configuration increases the number of available discrete states increases. In the limit of an infinite crystal lattice the energy separation between distinct states becomes vanishingly small and continuous energy bands form.

at 0 eV on the plot. The Fermi level does not necessarily correspond to the energy of a physical quantum state, but serves as a useful means of characterising the electronic structure of solids.

The conduction properties of a material are determined in part by the location of the Fermi level relative to the energy bands. An insulator has a large energy gap called a band gap between the valence band, the band containing the highest energy occupied state, and the conduction band, which contains the lowest energy unoccupied state [47, p. 28]. Hence the Fermi level lies between these two bands for an insulator at zero temperature.

In contrast with insulators, a metal has its Fermi level located within an energy band, and so does not have a band gap. This means that in reciprocal space all occupied electronic states will reside within a closed surface. This is called the Fermi surface. Because the Fermi level for a metal lies within a band and the states within a band are continuously distributed it only takes a small amount energy to excite an electron into a higher energy state.

To account for this during the energy minimisation it is necessary to include extra states beyond the minimum number for electronic structure metals calculations. The number of extra bands must be kept to a minimum since the computational cost increases quadratically with the number of bands. It is not possible to determine beforehand which bands will be unoccupied, so an initial calculation is required to determine the band occupancies and hence the number of extra bands needed to run the calculation.

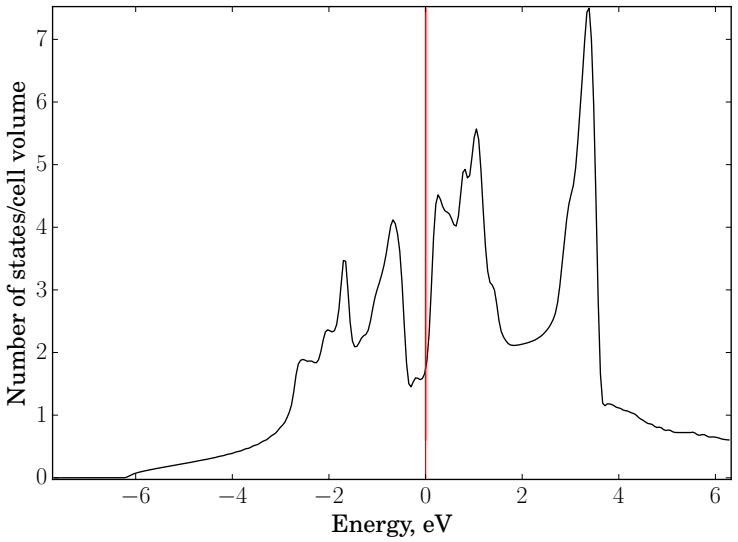



FIGURE 3.2: The density of states for $\alpha$-Ti computed using a primitive hexagonal close-packed unit cell of two Ti atoms. The red line at 0 eV is at the Fermi level. At this energy the occupancy is non-zero, which means that $\alpha$-Ti will have a partially filled band at the Fermi level and no band gap.

Because states are occupied up to the Fermi surface in a metal at 0 K this calculation involves the numerical integration of a step function. This is a computationally expensive operation because of the step function's discontinuity at the Fermi level. A common solution is to introduce a fictitious finite temperature, corresponding to an energy distribution centred around the Fermi level, that smooths the discontinuity of the step function. This procedure is called finite temperature smearing. This is what has been used to generate the density of states in Fig. 3.2.

The error associated with this smearing procedure depends on the amount of smoothing, which is given by the width of the temperature distribution (often called the smearing width), as well as the type of smearing scheme. The use of a temperature changes the calculation from calculating the total energy of the system to calculating the free energy of the system instead.

An estimate of this energy error given by one half of the product of the temperature and the entropy is calculated and added to the computed free energy at the end of the calculation to give an estimate of the 0 K total energy.

The smearing scheme that I used in all of my VASP calculations is the one developed by Methfessel and Paxton [73]. The smearing scheme uses an expansion of the step

function using Hermite polynomials multiplied by Gaussians to give very accurate results depending on when the expansion is truncated and the character of the function being integrated. In most cases a first- or second-order Hermite polynomial expansion provides a smooth approximation to the step function and produces an energy close to the true total energy for a given temperature [73]. In the case of my VASP calculations I used a first-order expansion with a smearing width of 0.1 eV.

One disadvantage of the Methfessel-Paxton smearing scheme is the possibility of introducing negative occupancies of electronic states, thus introducing the possibility of regions where the density is negative [74]. The scheme I used for all of my CASTEP simulations called cold smearing [74] has positive definite occupancies, and so avoids all problems associated with negative occupancies. Within CASTEP I used cold smearing with a smearing width of 0.1 eV.

## 3.4 Density mixing

Because metals do not have a band gap, i.e. their Fermi level lies within a band; the charge density can vary quite significantly with small changes in energy. This property of metals leaves them prone to the effects of 'charge sloshing': where a small change in the input charge density results in a large output charge density [75, III. A], [76]. This leads to large long-range oscillations of charge density, causing the calculation either to take much longer to reach a self-consistent solution or to diverge completely from the solution [76]. Thus self-consistent convergence can only be reached under these circumstances if oscillations are damped by minimising large long-range variations between the input and output densities of each iteration.

The most straightforward form of damping to implement for a given self-consistency cycle $N$ is to 'mix' in some of the input density $n_N^{in}(\mathbf{r})$ with the output density $n_N^{out}(\mathbf{r})$ to generate a new input density for SCF iteration $N+1$:

$$n_{N+1}^{opt,in}(\mathbf{r}) = \alpha n_N^{out}(\mathbf{r}) + (1-\alpha) n_N^{in}(\mathbf{r}). \tag{3.5}$$

The constant $\alpha$ can be used to specify the degree of mixing manually. This scheme is called simple or linear mixing. This scheme can be improved in many cases [77] by

mixing in input and output densities from previous self-consistency cycles as well as those of the current cycle. One such scheme is Pulay mixing [77] which involves taking a linear combination of the input densities

$$n^{in}_{opt,N+1} = \sum_{\mu=1}^{N} \alpha_\mu n^{in}_\mu, \tag{3.6}$$

where the coefficients $\alpha_\mu$ are constrained by norm conservation $\sum_{\mu=1}^{N} \alpha_\mu = 1$. The $\alpha_\mu$ are given by

$$\alpha_\mu = \frac{\sum_\nu A^{-1}_{\nu\mu}}{\sum_{\nu,\mu} A^{-1}_{\nu\mu}} \quad , \quad A_{\nu\mu} = \int d^3\mathbf{r} R([n^{in}_\nu], \mathbf{r}) R([n^{in}_\mu], \mathbf{r}), \tag{3.7}$$

where the charge density residual is defined as $R\left[n^{in}_\mu\right] = n^{out}_\mu[n^{in}_\mu] - n^{in}_\mu$. It is possible to improve this mixing procedure further by suppressing long-range variations in the density and thus more effectively prevent charge sloshing. This is done using a pre-conditioning method by Kerker [76]. First consider the Fourier transform of (3.6) with the addition of a term that depends on the Fourier transformed residuals $\tilde{R}\left[\tilde{n}^{in}_\mu\right]$:

$$\tilde{n}^{in}_{opt,N+1} = \sum_{\mu=1}^{N} \alpha_\mu \left( \tilde{n}^{in}_\mu + \mathbf{\Lambda} \tilde{R}\left[\tilde{n}^{in}_\mu\right] \right), \tag{3.8}$$

where $\tilde{n}^{in}_\mu \equiv \tilde{n}^{in}_\mu(\mathbf{G})$ are the Fourier transformed input densities and $\tilde{R}\left[\tilde{n}^{in}_\mu\right] = \tilde{n}^{out}_\mu(\mathbf{G}) - \tilde{n}^{in}_\mu(\mathbf{G})$. For Kerker pre-conditioning the $\mathbf{\Lambda}$ is a diagonal matrix:

$$\mathbf{\Lambda} = A \frac{G^2}{G^2 + G_0^2}, \tag{3.9}$$

where $A$ is a mixing weight, $G = |\mathbf{G}|$ and $G_0$ is a user-defined parameter that determines the 'length-scale' for damping. When $G \ll G_0$, i.e. long-ranged components, mixing is damped significantly.

The value of $A$ plays an important role in determining the rate at which convergence is reached. Too much mixing can slow down convergence to the ground-state, but too little will not damp out charge sloshing. Another consequence of using density mixing is that the wavefunction and the density must evolve separately, as the mixed densities do not necessarily correspond to a wavefunction of the system. Because of this density mixing is not variational, and so it is not guaranteed that the total energy will decrease

with each minimisation step.

## 3.5 Pseudopotentials

The electrons that are localised closest to the nucleus are called the core electrons, and are insensitive to the chemical environment of the atom. This means that their contribution to the total energy is to a good approximation unaffected when isolated atoms are brought together to form molecules or solids. The only significant energy changes occur in the valence electrons involved in chemical bonding, and so only those need to be updated every time the atoms are repositioned.

Not only are core electrons essentially chemically inert, they also cause computation difficulties when included in a calculation. The electronic states associated with each atom are eigenstates of the atomic Hamiltonian and so must be mutually orthogonal [52, pp. 135-136]:

$$\int d^3\mathbf{r}\psi_i^*(\mathbf{r})\psi_j^*(\mathbf{r}) = \delta_{ij}, \tag{3.10}$$

where the $\{i, j\}$ label the eigenstates. Because the core states are spatially localised near the nucleus the valence states must include rapidly oscillations in order to satisfy the mutual orthogonality condition as shown in Figure 3.3. Variations over small length scales must be described by plane-waves with large $\mathbf{k}$-vectors, which requires a higher cut-off energy as described in section 3.2. This drastically increases the computational cost of calculations involving these states.

These problems can be addressed by replacing the all-electron (AE) problem including the strong nuclear Coulomb potential and the core electrons with a pseudopotential, an effective potential than can be made as smooth and computationally cheap as the calculation requires. Using a pseudopotential also requires replacing the valence wavefunctions with pseudo (PS) wavefunctions that vary smoothly inside the core region.

One widely used class of pseudopotentials are called norm-conserving pseudopotentials [78]. A good norm-conserving pseudopotential is required to have the following features [79]:

- The PS wavefunctions should have no nodes or zeroes for $r < r_c$ as shown in

Fig. 3.3. Nodes are associated with spatial variations over small length-scales, and so removing them also removes high kinetic energy components.

- The radial components of the AE and PS wavefunctions, denoted by $R_i^{\mathrm{AE}}$ and $R_i^{\mathrm{PS}}$ respectively, agree outside a specified cut-off radius $r_c$:

$$R_i^{\mathrm{AE}}(r) = R_i^{\mathrm{PS}}(r) \text{ for } r > r_c. \tag{3.11}$$

- The pseudopotential is 'norm-conserving', that is charge inside the core region is preserved for both the AE and PS wavefunctions:

$$\int_0^{r_c} |R_i^{\mathrm{AE}}|^2 r^2 dr = \int_0^{r_c} |R_i^{\mathrm{PS}}|^2 r^2 dr. \tag{3.12}$$

- The AE and pseudo eigenvalues of the Kohn-Sham equations agree:

$$\epsilon_i^{\mathrm{AE}} = \epsilon_i^{\mathrm{PS}}. \tag{3.13}$$

These conditions help ensure that the logarithmic and first energy derivatives of the pseudo and AE wavefunctions agree when $r > r_c$ [78]. A related issue that is encountered when constructing pseudopotentials is transferability. Pseudopotentials are constructed for an isolated atom, but a well-constructed pseudopotential should be able to accurately reproduce the AE system properties in a wide range of chemical environments. If a large cut-off radius $r_c$ is used then typically a smoother pseudopotential described by fewer plane-waves can be constructed, since more of the PS wavefunction's functional form can be varied by the pseudopotential generation procedure, and thus it can be made smoother. However transferability usually suffers as a consequence because the core region could impinge upon the bonding region between atoms.

This trade-off between transferability and smoothness or 'softness' is a key issue for the construction of norm-conserving pseudopotentials [79]. Usually the cut-off radius must be close to the outermost maximum of the AE wavefunction to ensure good transferability [80]. This is restrictive for Ti because its $3d$ valence electrons are strongly localised near the core, requiring a small core region and thus a very 'hard' pseudopotential which needs to be described by a large plane-wave basis set. If the norm-conservation condition is dropped however, it is possible to create much softer pseudopotentials and significantly

lower computational costs. Two such methods that drop the norm-conservation condition and retain transferability are the ultrasoft pseudopotential (USPP, [81]) and the projector augmented-wave (PAW, [82]) methods.

Without norm-conservation the charge inside the core region can differ from the AE case. The difference is called the augmentation charge for both USPPs and PAW pseudopotentials, and must be kept track of to produce the correct Kohn-Sham eigenstates and charge density. The Ultrasoft and PAW pseudopotentials only differ in how they treat this core region. The PAW method uses actual on-site terms, whereas the USPP method uses a truncated linear expansion around a reference atom configuration [83]. The difference in practical terms is very little, but the PAW usually uses lower cut-off energies and performs better for magnetic systems. I have used ultrasoft pseudopotentials within the DFT code CASTEP version 8.0 [8] for the stacking faults calculations in chapter 5, and PAW pseudopotentials [83] within the DFT code VASP version 5.3.5 [84–87] for the point defects calculations in chapter 6.

The description of the augmentation charge and the charge density can be varied by varying the reciprocal space grid used to store them. The reason this is useful can be understood by considering the charge density. For norm-conserving pseudopotentials the charge density is given by the square of the wavefunction, thus doubling the number of terms in the Fourier series needed to describe it compared with the wavefunction. This means that the reciprocal space grid used to store the wavefunction is unlikely to have a enough samples to describe the charge density.

To account for this the charge density is usually stored on a larger spherical grid with a maximum radius of $2|G_{cut}|$. The value of this maximum radius can be varied but I chose a value of $2|G_{cut}|$ for all our CASTEP and VASP calculations as this is recommended to ensure an accurate description of the charge density [88].

The augmentation charge is described on another grid often called the fine or augmentation grid. The reason that another grid is required is that the augmentation charge can require a very large grid to be described accurately [88]. We set this grid equal to the charge density grid, i.e. a reciprocal space spherical grid with a radius of $2|G_{cut}|$. Because my cut-off energy convergence tests in section 4.2.1 produced a reasonable cut-off energy for both CASTEP and VASP I kept the radius of both augmentation grids set at $2|G_{cut}|$.

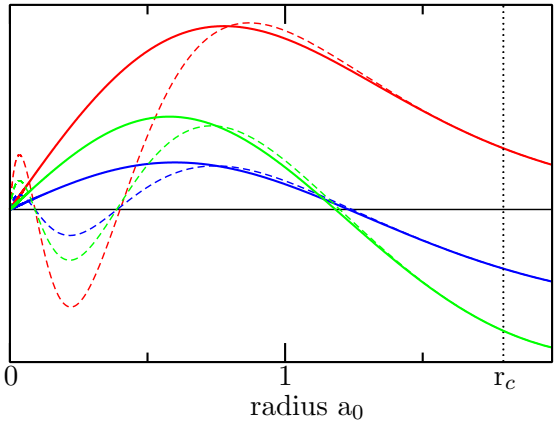



FIGURE 3.3: The all-electron (AE) radial s-orbital wavefunctions for a Ti atom (broken lines) and the corresponding pseudo (PS) wavefunctions (solid lines). This plot was generated by CASTEP's on-the-fly pseudopotential generator [8]. The vertical black dotted line is the cut-off radius (1.8 $a_0 \approx 9.5 \times 10^{-11}$ m) for the pseudopotential. The functional form of the AE and PS wavefunctions agree for $r > r_c$. For $r < r_c$ the PS wavefunctions have fewer nodes and so are less oscillatory than the AE wavefunctions.

Ti has 22 electrons with the electronic configuration $1s^2\ 2s^2\ 2p^6\ 3s^2\ 3p^6\ 3d^2\ 4s^2$ in standard orbital notation [50, Vol. III, Ch. 19]. Elements like Ti pose a problem for pseudopotential generation because there is not a clear distinction between its core and valence electrons. Usually the $1s^2\ 2s^2\ 2p^6$ are described as core electrons, and $3d^2\ 4s^2$ as valence electrons, but the so-called semi-core states $3s^2\ 3p^6$ can affect a pseudopotential's accuracy if they are treated as core states [46].

Because of this there are two types of pseudopotential that are often used for Ti: those that have four $3d^2\ 4s^2$ valence states (4elPP) and those that have twelve $3s^2\ 3p^6\ 3d^2\ 4s^2$ valence states (12elPP). The inclusion of 8 extra valence states means that the 12elPP is more computationally expensive than the 4elPP. However it has been shown that properties such as the stable crystal phase of Ti at 0 K is different for the 4elPP compared with the 12elPP [46]. I have used a 12elPP generated on-the-fly by CASTEP, as well as a 4elPP generated by White [89]. Unless stated otherwise I used the 12elPP.

Another widely used configuration is a 10-valence state pseudopotential (10elPP) that confines the $3s$ states to the core. This description has the advantage that the $4s$ states don't need to be orthogonalised with respect to there $3s$ states when they are described as core states, which decreases the computational cost compared with the 12elPP case. Unless stated otherwise a 10elPP of the PAW type was used for Ti in all point defect calculations described in chapter 6.

# Chapter 4

# Bulk phases of titanium

As described in the previous chapter, modelling metals using DFT is a challenging endeavour. The absence of a band-gap near the Fermi level in their band structure means that there exists a Fermi surface dividing occupied and unoccupied states in reciprocal space. An accurate description of this Fermi surface requires detailed consideration of the electronic structure of the metal.

The electronic structure of Ti includes valence electrons that occupy $s$- and $d$-type orbitals in the ground-state. These orbitals correspond to the formation of very different types of bonds: bonds formed from $s$- and $p$- orbitals are usually very un-directional and isotropic [66, pp. 109-111], whereas bonds formed from $d$-orbitals are very directional and anisotropic [66, ch. 9]. Nevertheless both types of bonding must be described accurately to obtain physically meaningful predictions about the bonding of Ti in its solid form. Because DFT treats all electrons explicitly it represents an ideal method for simulating solid Ti.

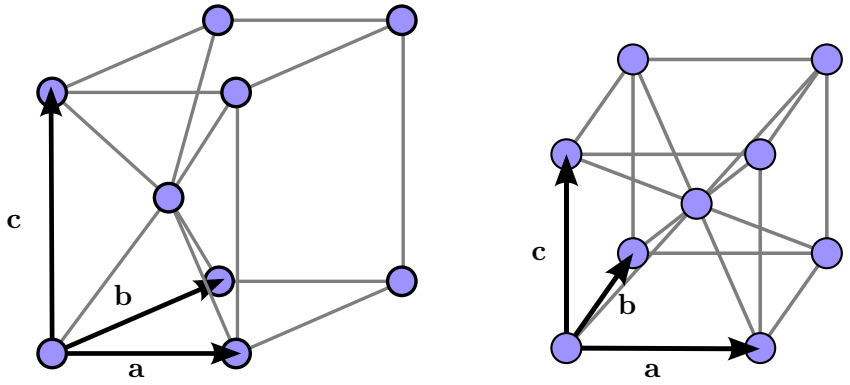
This chapter summarises how I parameterised and tested my plane-wave pseudopotential DFT model used to simulate bulk Ti. I describe the atomic geometries I used to simulate hexagonal close-packed (hcp) and body-centred cubic (bcc) Ti, the convergence tests carried out to determine the DFT cut-off energy and **k**-point mesh, and the equilibrium lattice parameters of both crystal structures at zero temperature. I used CASTEP version 8.0 [8] and VASP version 5.3.5 [84–87] throughout this chapter.

To demonstrate the accuracy of the DFT model I computed the hcp and bcc elastic

constants for Ti. The DFT model's accuracy is verified by comparing the elastic constants with other DFT and experimental values in the literature. The chapter concludes with a study of the directional bonding in hcp-Ti I carried out by looking at the charge densities of bulk hcp-Ti and and face-centred cubic Al.

## 4.1 The unit cell

For all my bulk hcp simulations I used the primitive unit cell as shown in Fig. 4.1(A), which contains two atoms and is one way of constructing the smallest unit cell of the hcp crystal [90, p. 7, and pp. 133-135]. The primitive unit cell has three lattice vectors $\{\mathbf{a}, \mathbf{b}, \mathbf{c}\}$, with $\mathbf{a}$ and $\mathbf{b}$ of equal magnitude $|\mathbf{a}| = a$ separated by 60° and $\mathbf{c}$ perpendicular to both $\mathbf{a}$ and $\mathbf{b}$. For all the bcc simulations I used a conventional cubic bcc unit cell shown in Fig. 4.1(B), with three lattice vectors $\{\mathbf{a}, \mathbf{b}, \mathbf{c}\}$ of equal magnitude $|\mathbf{a}| = a$ and each pair separated by 90°. I used the experimental lattice parameters $a = 2.95$ Å and $|\mathbf{c}| = c = 4.68$ Å for hcp [91] and $a = 3.31$ Å for bcc [92] to carry out the cut-off and $\mathbf{k}$-point convergence tests described in the following section 4.2.




(A) hcp (B) bcc

FIGURE 4.1: The unit cells I used to simulate hcp and bcc Ti.

## 4.2 Convergence tests

### 4.2.1 Cut-off energy

I determined the optimal cut-off energy by varying the working cut-off energy and computing the total energy difference between this calculation and the same calculation

carried out with a very large cut-off energy ($E_{tot}$ - $E_{\infty}$). I used 1000 eV for the very large cut-off energy. I chose a working cut-off energy that resulted in a balance between obtaining an accurate value of the total energy, and an efficient use of computational resources.

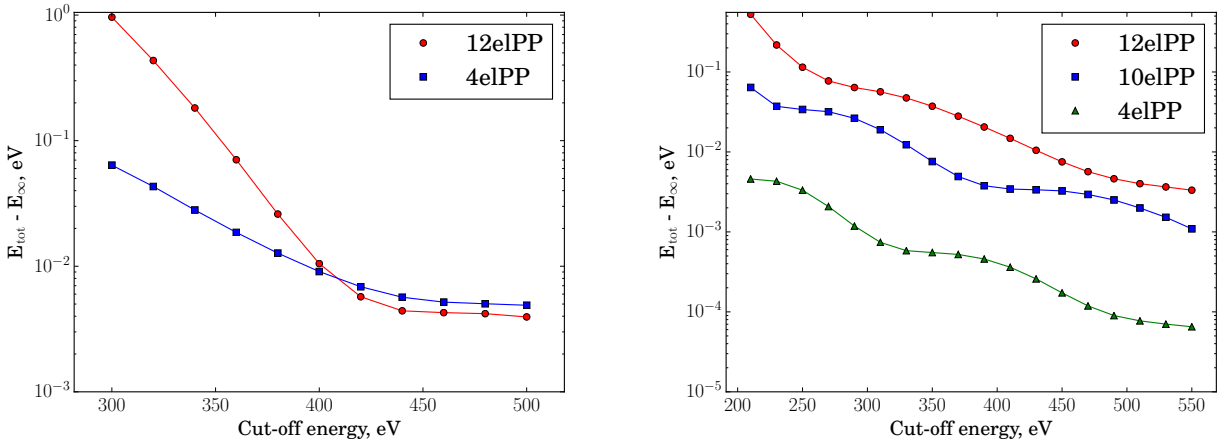
The convergence test results for different pseudopotentials used in CASTEP and VASP are shown in Fig. 4.2. The pseudopotentials are described in section 3.5. The plots show that the pseudopotential choice can significantly change the cut-off convergence behaviour. The PAW pseudopotentials provided with VASP converged faster than the 12elPP USPP that CASTEP generates by default, and the 4elPP generated by White [89]. In addition a qualitative difference between the CASTEP and VASP pseudopotentials is that the CASTEP pseudopotentials plateau after about 450 eV, but those of VASP plateau at multiple points. This means that VASP pseudopotentials can show apparent convergence at numerous cut-off energies.

The PAW pseudopotentials with fewer valence states converged more rapidly than those with more valence states. The reason for this is that valence states such as the $3s$ and $3p$ states will have variations on shorter length-scales, and hence will require a higher cut-off energy to describe these variations. For the CASTEP USPPs convergence of the 4elPP is more rapid than the 12elPP for smaller cut-off energies, but both reach almost the same level of convergence at higher cut-off energies. Based on these convergence test results I chose a cut-off energy of 480 eV for the CASTEP 12elPP and 4elPP, and a 350 eV cut-off energy for the VASP 10elPP.

### 4.2.2 Brillouin zone sampling

I used Monkhorst-Pack (MP) grids for all **k**-point sampling grids [72]. Recall from section 3.1 that reciprocal space lengths are inversely proportional to their corresponding real space lengths. Because of this the $c/a$ ratio of the hcp crystal structure helps to partially determine the optimal **k**-point MP mesh. If there are $M$ **k**-points along all of the $a$-type reciprocal directions, then using $M(c/a)^{-1}$ **k**-points along the $c$-type reciprocal direction will result in the same **k**-point density along all three directions.

This is what I have done for the MP grids used in Fig. 4.3, where the MP grid takes the form $N_1 \times N_1 \times N_2$, where $N_1/N_2 \approx c/a$ in each case. In Fig. 4.3 there is a general




(A) CASTEP (B) VASP

FIGURE 4.2: The variation of the total energy with cut-off energy generated using the 12elPP, 10elPP, and 4elPP within CASTEP and VASP. The system I used was a primitive hcp unit cell of two Ti atoms. All total energies are shown as deviations from $E_\infty$, which was generated using the same system with a cut-off energy of 1000 eV.

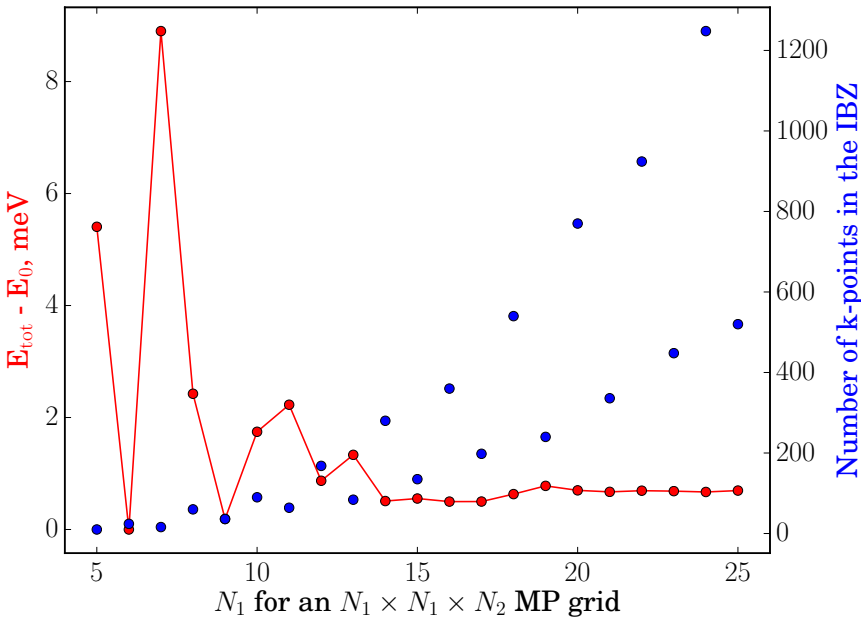



FIGURE 4.3: The convergence of the total energy with **k**-point sampling. The abscissa is the first component $N_1$ of the $N_1 \times N_1 \times N_2$ MP sampling grid. $N_1$ and $N_2$ are chosen s.t. $N_1/N_2 \approx c/a$. Total energies $E_{tot}$ are expressed relative to the lowest total energy of the dataset $E_0$. The MP grid is also compared with the corresponding number of **k**-points in the irreducible Brillouin zone.

trend that odd-numbered grids use fewer **k**-points in the irreducible Brillouin zone (IBZ) compared to even-numbered grids that have a similar number of **k**-points in the first Brillouin zone (1BZ). The reason for this is that odd-numbered grids contain the Γ-point,

the **k**-point at the origin of reciprocal space. Grids containing this point are consistent with the hcp rotational symmetry, and so the number of **k**-points in the 1BZ on these grids reduce to fewer **k**-points in the IBZ. Based on the results in Fig. 4.3 I used a $23 \times 23 \times 15$ MP sampling grid for bulk hcp-Ti. To get a similar **k**-point density for bcc-Ti I used a $20 \times 20 \times 20$ MP sampling grid.

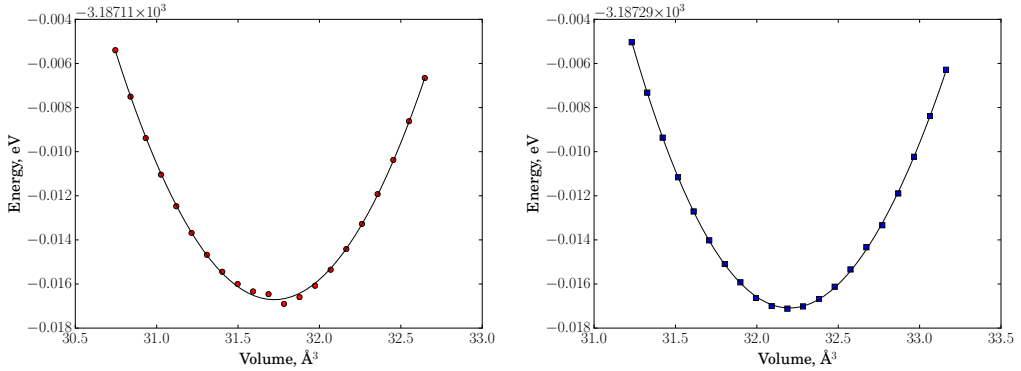
## 4.3 Lattice parameters

Once well-converged values for the cut-off energy and the **k**-point sampling grid were found, I determined the equilibrium geometry of the hcp and bcc bulk crystal structures of Ti at 0 K. I did this by using the unit cells described in section 4.1 and varying the $a$- and $c$-lattice parameters for hcp and the $a$-lattice parameter for bcc.

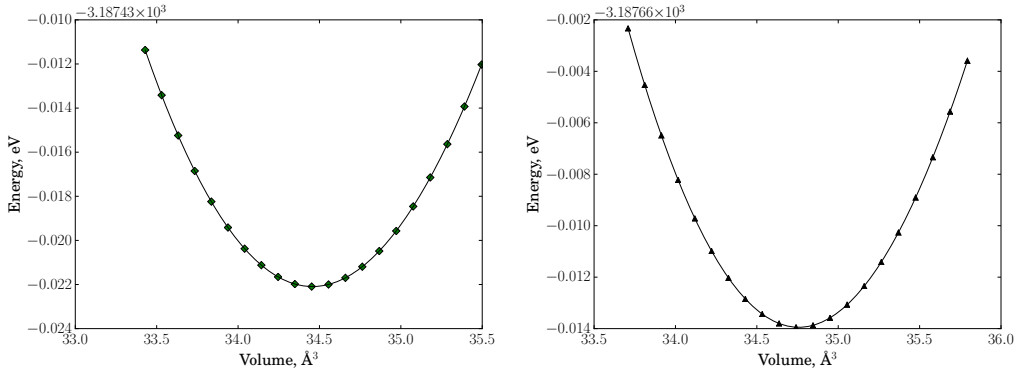
The $a$-lattice parameter was determined for each bulk phase by computing an energy-volume curve where the unit cell volume is varied by a uniform scaling of all of the lattice vector lengths. I then fitted the resulting set of points to a continuous curve given by the Birch-Murnaghan equation of state [93, 94]. The equilibrium volume and $a$-lattice parameter is then obtained from the minimum of the fitted function.

The energy-volume curves I computed for the hcp and bcc phases using the PBE and LDA exchange-correlation functionals within CASTEP are shown in Fig. 4.4, as well as the resulting equilibrium $a$-lattice parameters. Fig. 4.4 shows how the LDA and PBE functionals underestimate the equilibrium volume compared with experiment, but the PBE functional does so to a lesser degree. I found similar results using VASP as shown in Fig. 4.5. The equilibrium lattice parameters in Fig. 4.5(E) are almost identical to those in. Fig. 4.4(E).

I used a similar procedure to compute the $c$-lattice parameter for hcp-Ti using the PBE functional and the 12elPP within CASTEP, the results of which are shown in Fig. 4.6(A). The $a$-lattice parameter was held fixed whilst I varied the $c$-lattice parameter. In this case the curve was fitted to a second order polynomial function of the $c/a$ ratio. I found the minimum of the curve to be 1.580. I carried out the same procedure for VASP using the 10elPP and obtained an equilibrium $c/a$ ratio of 1.586 as shown in Fig. 4.6(B).




(A) bcc-LDA (B) hcp-LDA



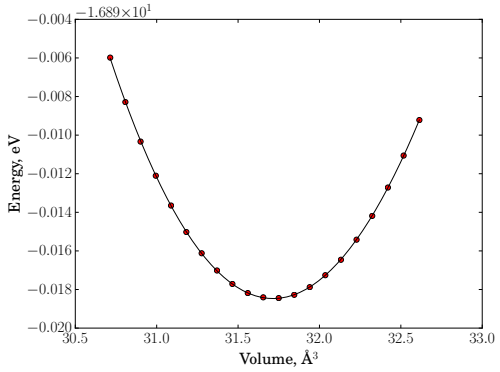

(C) bcc-PBE (D) hcp-PBE

| | PBE | LDA | Experiment |
|---|---|---|---|
| hcp | 2.937 | 2.863 | 2.95 [91] |
| bcc | 3.254 | 3.166 | 3.31 [92] |

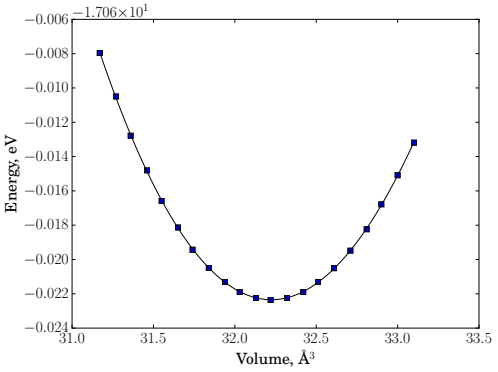
(E) Equilibrium lattice parameters, Å

FIGURE 4.4: (A-D) The energy-volume curves computed using CASTEP for the hcp and bcc crystal structures simulated using the LDA and PBE exchange-correlation functionals. I used the USPP 12elPP to obtain the data shown in this figure. Each plot has its energy offset by the amount shown in the top-left corner of the plot. Both cells simulated were two-atom cells, so the volumes and energies can be compared directly. (E) The equilibrium $a$-lattice parameters in Å obtained from the energy-volume curves.

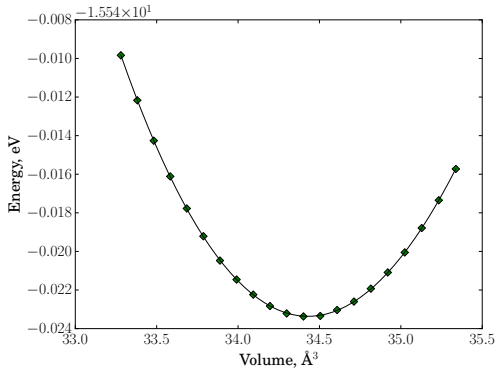
Using the equilibrium hcp and bcc geometries it is possible to compute the phase stability of hcp relative to bcc at 0K by computing the cohesive energy difference between the two bulk phases. For VASP using the 10elPP and the PBE functional I found that the cohesive energies for the hcp and bcc phases were -5.273 eV and -5.165 eV respectively, with an energy difference of 0.108 eV. These energies are in good agreement with those of Huang *et al.* [95].



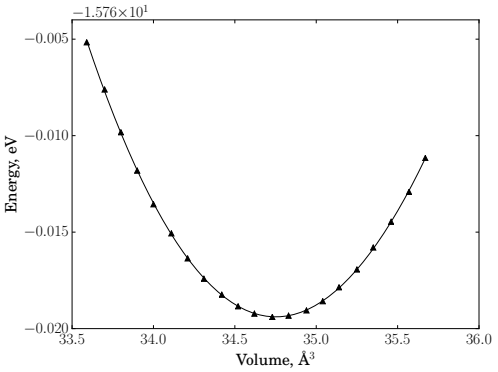

(A) bcc-LDA




(B) hcp-LDA




(C) bcc-PBE




(D) hcp-PBE

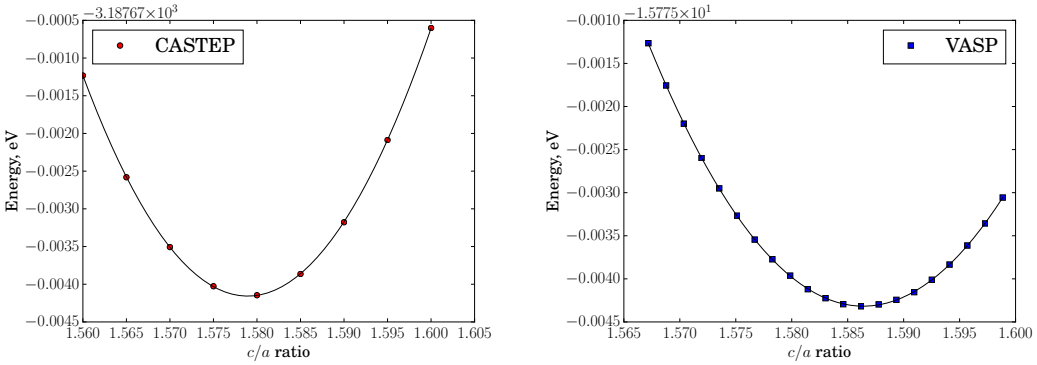
| | PBE | LDA | Experiment |
|---|---|---|---|
| hcp | 2.937 | 2.864 | 2.95 [91] |
| bcc | 3.253 | 3.165 | 3.31 [92] |

(E) Equilibrium lattice parameters, Å

FIGURE 4.5: (A-D) The energy-volume curves computed using VASP for the hcp and bcc crystal structures simulated using the LDA and PBE exchange-correlation functionals. I used the PAW 10elPP to obtain the data shown in this figure. Each plot has its energy offset by the amount shown in the top-left corner of the plot. Both cells simulated were two-atom cells, so the volumes and energies can be compared directly. (E) The equilibrium $a$-lattice parameters in Å obtained from the energy-volume curves.

## 4.4 Elastic constants

As a test of my DFT model for hcp- and bcc-Ti I computed the elastic constants of both crystal structures. Computing the elastic constants is equivalent to taking the second derivative of the total energy with respect to applied strain. Hence the elastic constants are very sensitive to errors in the computational model. I computed the elastic constants by applying strains $\epsilon_i$ $(i = 1, \ldots, 6)$ to the equilibrium geometry described in sections 4.1 and 4.3 and then computing the resulting stress tensor $\sigma_i$ $(i = 1, \ldots, 6)$. The elastic




(A) CASTEP (B) VASP

FIGURE 4.6: The variation of the total energy of a primitive unit cell of hcp-Ti with $c/a$ ratio computed using (A) CASTEP and (B) VASP. Both plots have their energy offset by the amount shown in the top-left corner of the plot. The points were fitted to quadratic polynomials of the $c/a$ ratio, with minima at (A) 1.580, and (B) 1.586.

constants $C_{ij}$ were then obtained from the following relation [96, section 5]:

$$\sigma_i = \sum_{j=1}^{6} C_{ij}\epsilon_j. \tag{4.1}$$

I generated the elastic constants using the scripts written by Andrew Walker and Dan Wilson [97, 98]. The scripts generated the required strain matrices and computed the elastic constants from the stresses output by CASTEP.

| | Results | | Tegner *et al.* [99] | | Jafari *et al.* [100] | | Experiment [91] | |
|---|---|---|---|---|---|---|---|---|
| | $\alpha$ | $\beta$ | $\alpha$ | $\beta$ | $\alpha$ | $\beta$ | $\alpha$ | $\beta$ |
| $C_{11}$ | 206 | 90 | 169 | 90 | 168 | 114 | 176 | - |
| $C_{12}$ | 92 | 113 | 92 | 112 | 88 | 88 | 87 | - |
| $C_{13}$ | 85 | - | 70 | - | 72 | - | 68 | - |
| $C_{33}$ | 195 | - | 203 | - | 185 | - | 191 | - |
| $C_{44}$ | 43 | 41 | 47 | 41 | 40 | 45 | 51 | - |
| B | 125 | 106 | 112 | 105 | 109 | 97 | 102 | - |

TABLE 4.1: The elastic constants for Ti in its hcp ($\alpha$) and bcc ($\beta$) bulk phases computed using DFT and experiment. All values are expressed in GPa.

The elastic constants are shown in table 4.1 along with other values obtained from DFT and experiment. The errors in the final fitting procedure were within 5 GPa. My results for hcp-Ti are all within about 20% of the experimental values. These deviations are fairly typical of elastic constant calculations [101]. My bcc-Ti elastic constants are in

good agreement with those of Tegner *et al.* [99] with a maximum deviation of about 1%. The disagreement with the results of Jafari *et al.* [100] is more significant, with the largest deviation between the $C_{12}$ bcc elastic constants of about 28%. One significant difference between models is the significantly lower value of the equilibrium bcc lattice parameter of 3.16 Å of Jafari *et al.* [100] compared with about 3.25 Å in tables 4.4(E) and 4.5(E).

## 4.5 Directional bonding in Ti

Ti in its hcp or $\alpha$-phase is an anisotropic material in terms of its crystallographic and mechanical characteristics [23, section 2]. One proposed explanation for this anisotropy is that the valence electrons occupying the $3d$-orbital of Ti and forming unsaturated covalent bonds along certain preferred directions ([102] and [66, ch. 9]).

A contrasting example is the metallic bonding of Al in its solid form. This bonding is due to Al having two electrons in the $3s$-orbital and one electron in the $3p$-orbital of its valence shell. The metallic bonding between Al atoms means that they behave like hard spheres embedded in a homogeneous electronic 'gas' [66, pp. 109-111]. This is why Al has a face-centred cubic (fcc) crystal structure at low temperatures and pressures.

To investigate the directional bonding in Ti and Al I carried out total energy minimisations on bulk hcp-Ti and fcc-Al. I used VASP version 5.3.5 [84–87] to compute the ground-state properties of these structures, and for the simulations of Al I used a PAW pseudopotential with three valence states from the VASP pseudopotential database [83, 103, 104]. I then plotted the charge densities of both metals using VESTA [105].

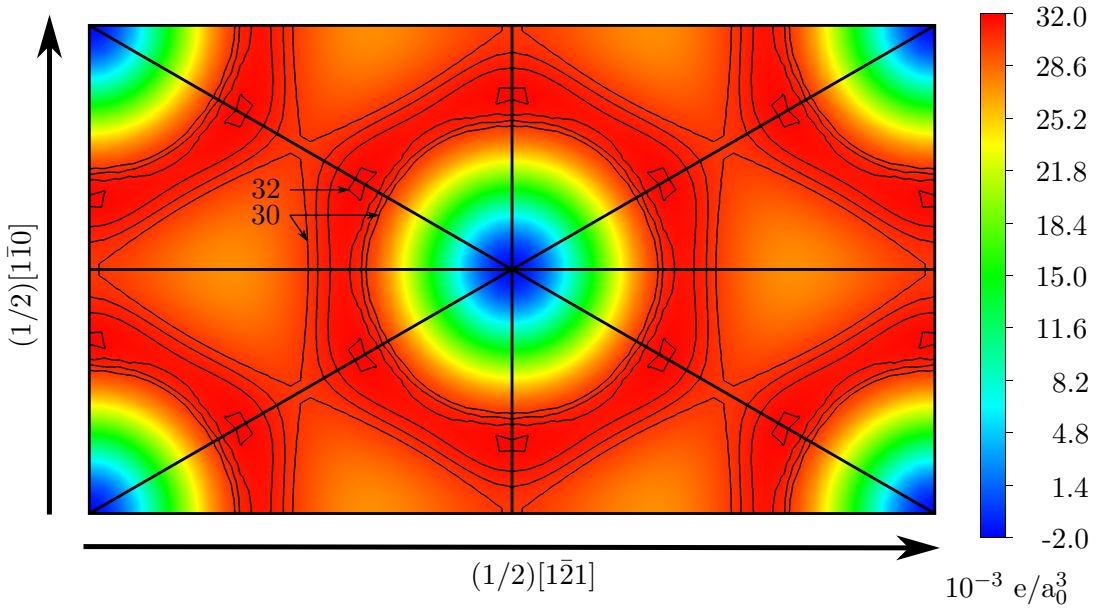
The charge densities on the (111) and (0001) close-packed planes of fcc-Al and hcp-Ti are shown in Fig. 4.7(A) and (B) respectively. These are the charge densities of the valence electrons of the corresponding pseudopotential. Atom centres are at the corners and the centres of both plots. The difference between the charges at the atom centres of Al in Fig. 4.7(A) and Ti in Fig. 4.7(B) is mainly due to the Ti pseudopotential having 10 valence electrons compared with the three in the Al pseudopotential. It is also partly due to the different forms of the pseudopotentials.

The different number of valence electrons in each element is also the most likely reason for the differing charge density ranges in the valence regions between ionic cores. In Al the valence region has a flat charge density shown by the contours of constant charge density in the range of 30 to 32 $\times$ $10^{-3}$ e/$a_0^3$ in Fig. 4.7(A). The valence region of Ti contains contours over the wider range of 22 to 35 $\times$ $10^{-3}$ e/$a_0^3$ in Fig. 4.7(B).

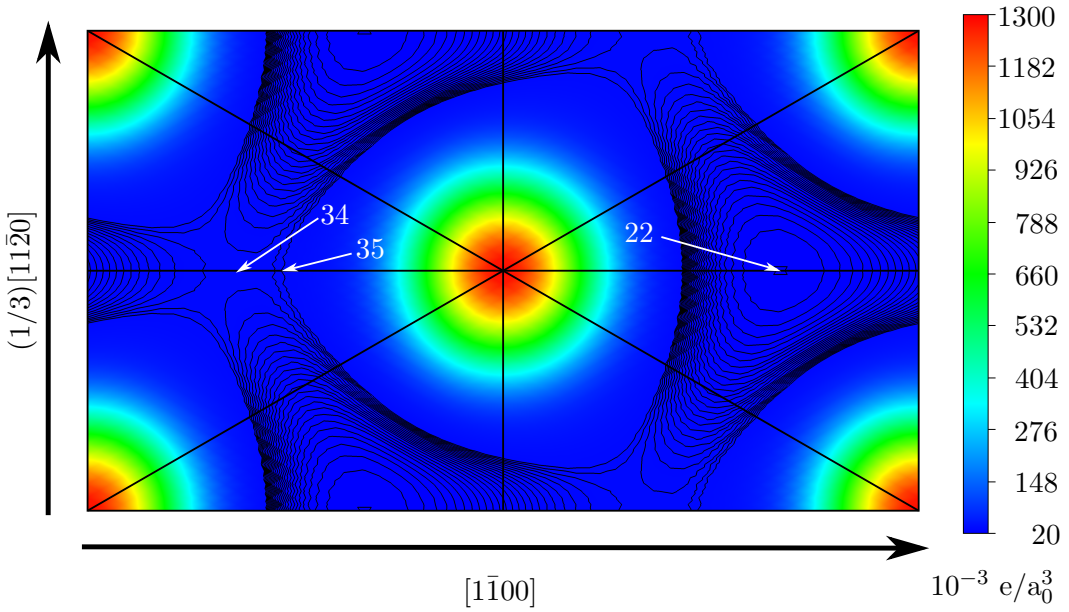
The contours in Fig. 4.7(B) reveal an accumulation of charge of about $34 \times 10^{-3}$ e/$a_0^3$ in between three Ti atoms to the left of the figure. This feature looks like the pseudoatom (unrelated to pseudopotentials) in the charge density of hcp-Zr in the work of Eberhart *et al.* [106]. Hence I shall call this feature a pseudoatom in this discussion. The charge density is concentrated in this region on the (0001) basal plane, but is lower in the regions directly between nearest neighbour Ti atoms in the basal plane. The pseudoatom in Ti appears to act like a bond charge, with bonds forming through the pseudoatom between the three neighbouring Ti atoms in the basal plane, and the two Ti atoms directly above and below the pseudoatom (going out of the page).

In Figs. 4.7(A) and 4.7(B) the heat plots show that near the ionic cores the charge in both planes is very circular. However the charge density in the valence region between atoms, as shown by the contours, is less spherical in both plots. The Al contour nearest its atom centres (with a charge density of $30 \times 10^{-3}$ e/$a_0^3$) is circular, with other contours taking on a rounded hexagonal shape the further they are from the atom centres. The Ti contour closest to the atom centres (with a charge density of $35 \times 10^{-3}$ e/$a_0^3$) appears quite non-circular with a rounded triangular shape.

Whilst both planar charge densities show signs of directional bonding due to the non-circular contours in the valence region, Ti shows a greater tendency towards directional bonding from the plots in Fig. 4.7. The presence of pseudoatoms or bond charges in the basal plane of Ti also suggests that there is a more heterogeneous distribution of charge in the valence region compared with the (111) plane of Al. However, it can be argued that the variations in charge density in the valence region are very small compared with the variations over the whole plot, and so these variations are not large enough to be evidence of directional bonding.




(A) Al




(B) Ti

FIGURE 4.7: The charge densities of (A) bulk fcc-Al on the (111) plane, and (B) bulk hcp-Ti on the (0001) basal plane. In both plots atoms are at the corners and centre. The straight black lines mark the edges where charge density plots were tiled in a periodic fashion to include an atom in the centre of the plot. They are not contours of constant charge. The contours of constant charge density are (A) $\{30, 30.5, 31, 31.5, 32\}$, and (B) $\{22, 22.5, 23, \ldots, 35\}$ in units of $10^{-3}$ e/$a_0^3$. Values for specific regions and contours have been indicated using arrows.

# Chapter 5

# Stacking faults in titanium

Ti and its alloys are known to deform plastically primarily by slip at low temperatures [14, pp. 19-23]. Some Ti-alloys also deform significantly via twinning, but for $\alpha$ and near-$\alpha$ Ti-alloys with around 6 weight percent Al, such as the two Ti-alloys Ti-6242 and Ti-6246, twinning is suppressed [39]. The dominant slip systems of Ti involve dislocations with Burgers vectors $\langle \mathbf{a} \rangle = (1/3)\langle \bar{1}\bar{1}20 \rangle$ that glide on the $\{1\bar{1}00\}$ prism planes shown in red in Fig. 5.1 [107].

Because there are only two independent prism slip systems, three additional independent slip systems are required to accommodate an arbitrary deformation according to the von Mises criterion [108]. One possibility is '**c+a**-slip' involving Burgers vectors of the form $\langle \mathbf{c}+\mathbf{a} \rangle = (1/3)\langle 1\bar{2}13 \rangle$ on the $\{01\bar{1}1\}$ first-order pyramidal or pyramidal I planes, shown in green in Fig. 5.1. This deformation mode has been observed experimentally as well as **c+a**-slip on $\{11\bar{2}2\}$ pyramidal II planes [109–112]. The four independent **c+a** slip systems on the pyramidal I plane are more than enough to satisfy the von Mises criterion.

One clue to understanding slip behaviour is that in general the dominant slip plane coincides with spreading or dissociation of the dislocation core in that crystallographic plane [113]. Dissociation of a perfect dislocation into partial dislocations on a crystallographic plane requires the presence of low energy stable stacking faults (SFs) [114, section 10.3]. The low energy stable SFs of a given slip plane can be identified as local minima of the $\gamma$-surface or generalised stacking fault energy (GSFE) surface corresponding to that plane [115]. In addition, for a dislocation core that is spread in the slip plane, the slope of the $\gamma$-surface for that slip plane determines the force that constricts the core [116].

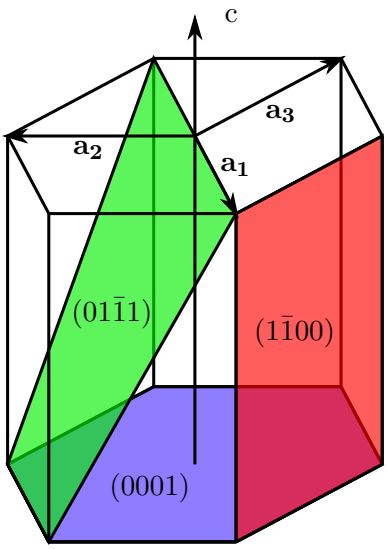



FIGURE 5.1: The (0001) basal, (1$\bar{1}$00) prism, and (01$\bar{1}$1) pyramidal I planes are shown in blue, red, and green respectively.

In addition to this inherent interest of $\gamma$-surfaces in $\alpha$-Ti, the work summarised in this chapter served as a learning exercise in carrying out large-scale density functional theory (DFT) calculations on $\alpha$-Ti. I used plane-wave pseudopotential DFT as described in the previous chapter 4 as well as four interatomic potentials (IPs) to compute $\gamma$-surfaces on the basal and pyramidal I planes for $\alpha$-Ti. I also computed the prism $\gamma$-surface using the IP Ti0 described in section 5.1.

This chapter is divided into three sections. The first section 5.1 details IP studies using the IP Ti0 developed by Ackland [9]. I used Ti0 to develop the methods of forming SFs and computing $\gamma$-surfaces with a much less computationally expensive method than DFT. The second section 5.2 details the DFT studies carried out, including the computation of the full pyramidal I $\gamma$-surface. The third section 5.3 details how those DFT results were used to test three IPs Ti1, Ti2, and Ti3 recently developed by Mendelev *et al.* [49] to assess their capability of simulating plastic deformation in $\alpha$-Ti.

## 5.1 Interatomic potential Ti0 studies

### 5.1.1 Stacking sequences

The basal plane, shown in Fig. 5.1 highlighted in blue, has a two-fold stacking sequence ...ABABAB..., with an inter-planar separation of $c/2$. The A sites in Fig. 5.2(A) are

related to the B sites by the translation $(1/3)[1\bar{1}00] \pm (1/2)[0001]$. If the atoms in the B plane are shifted by $(1/3)[1\bar{1}00]$, then the atoms will be shifted into an equivalent position in the lattice relative to the A plane under a 180° rotation. I shall denote this translated B plane by C because it is related to the A plane via a different translation vector.

The stacking sequence of the hcp basal planes is related to the stacking sequence of the fcc (111) planes that have a three-fold stacking sequence ...ABCABC.... Interrupting the hcp basal plane stacking sequence by translating half of the crystal by $(1/3)[1\bar{1}00]$ the stacking sequence takes on a local fcc structure $\ldots ABAB|CACA\ldots$. This SF is often called $I_2$ in the literature [9, 117] and is a low energy stable SF for many hcp crystals [117, 118].

The prism atomic planes in the hcp crystal have a four-fold stacking sequence $\ldots ABCD\ ABCD\ldots$ shown in Fig. 5.2 (B). The prism inter-planar spacing alternates between narrow and wide spacing. Hence there are two distinct places where SFs can be formed. I assumed that faults formed between narrowly-spaced planes would be too high energy to be relevant at in low temperature plasticity, so I only considered prism faults formed between the widely-spaced planes.

As was the case with the prism plane, the $(1\bar{1}01)$ pyramidal I plane's 16-fold stacking sequence has two distinct inter-planar spacings between the atomic planes as can be seen

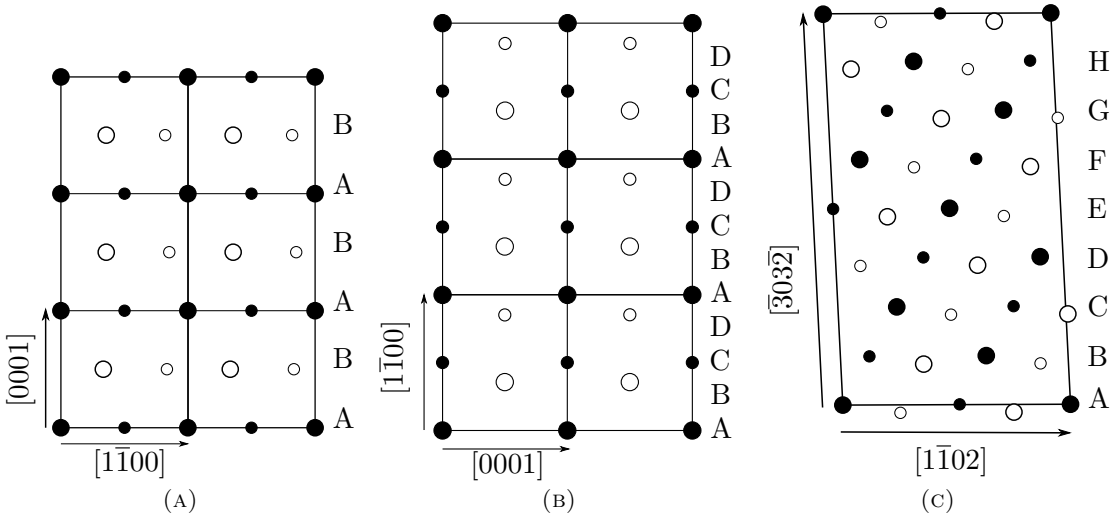



FIGURE 5.2: The stacking sequences of the (A) basal, (B) prism, and (C) pyramidal I 'superplanes' in $\alpha$-Ti. Small and large circles distinguish atoms on adjacent $(11\bar{2}0)$ planes. (A) and (C) from [2].

in Fig. 5.2. The closely-spaced pairs of planes have an inter-planar spacing of about 0.37 Å compared with an inter-planar spacing of about 1.86 Å between the widely-spaced planes according to my bulk DFT calculations (the lattice parameters I used are described in section 4.3). Because the inter-planar spacing of the closely-spaced pairs of planes is much less than the a-lattice parameter of 2.94 Å these pairs of planes tend to shear together as a single unit which I will call a 'superplane' as described by Tang and El-Awady [119].

These superplanes have an eight-fold stacking sequence $\ldots ABCDEFGHABCDEFGH \ldots$ labelled in Fig. 5.2. By considering the stacking sequence there are three possible SFs that can be formed by adding or removing superplanes without bringing atoms too close together or far apart [9]. These are:

1. $I_1$
   $\ldots ABCDEFGH|CDEFGHAB \ldots$,
2. $I_2$
   $\ldots ABCDEFGH|GHABCDEF \ldots$.

Since all of these faults can be formed by the rigid translation of one crystal half with respect to the other, all of these faults are intrinsic SFs. I have labelled the first two faults $I_1$ and $I_2$ because as shall be shown later in this chapter they are both stable intrinsic SFs.

### 5.1.2 The interatomic potential Ti0

The interatomic potential (IP) Ti0 used in all the calculations summarised in this section is a Finnis-Sinclair (FS) potential [48] developed by Ackland [9]. FS potentials are a type of central-force (CF) potential like those of the embedded atom model [120] that rely on the second-moment approximation of tight-binding [121]. CF potentials are implicitly expressed in terms of pair potentials only with no explicit angular dependence, and so total energies computed using these potentials depend only on the relative separations between atoms [122].

The version I used was developed for LAMMPS [123] by Mendelev [10]. This potential was fitted to an fcc crystal structure with a negative SFE on the (111). The potential

| Physical Quantity | This work | Ackland [9] | Experiment |
|---|---|---|---|
| Cohesive energy (eV) | 4.85 | 4.85 | 4.85 [124] |
| Lattice parameter a (Å) | 2.967 | 2.967 | 2.95 [91] |
| c/a ratio | 1.592 | 1.592 | 1.587 [91] |

TABLE 5.1: The equilibrium cohesive energy and lattice parameters I computed using Ti0 [9]. The values are compared with those of Mendelev [10] computed using Ti0 and with experimental values.

was also fitted to the cohesive energy and a-lattice parameter shown in table 5.1, but also correctly reproduces the $c/a$ ratio in good agreement with experiment.

### 5.1.3 Stacking fault simulation methods

I imposed two properties on my system geometries to simulate isolated SFs accurately. The first is that all possible SFs can be formed by rigid relative translation along the plane of interest followed by relaxation perpendicular to the fault plane. The second is that the number of atoms is conserved during displacement using 3-dimensional periodic boundary conditions. Two types of system geometry that have both of these properties I will call bulk and slab geometries.

I used the bulk geometry to simulate all basal and prism gamma-surfaces in this thesis. The un-faulted bulk geometry consists of a supercell made of perfect crystal. It is not possible to introduce a single SF by rigidly displacing part of the crystal relative to the other without violating the periodic boundary conditions being imposed. It is however possible to form a single SF using the 'tilted cell' boundary conditions described in Sutton and Balluffi [125]. Using the bulk geometry two equal but opposite SFs were formed by rigidly displacing the middle section of the cell along the crystallographic plane of interest. This is shown in Fig. 5.3(A). If the two faults are well separated the influence of their interaction is minimised and both faults can be treated as isolated from each other. If this is the case the two faults will be structurally identical with the same SFE. The bulk geometry was used to simulate all basal and prism $\gamma$-surfaces in this thesis.

The slab geometry consists of an infinite slab with two surfaces separated by a region of vacuum. A SF is formed by translating one slab half along the plane of interest with respect to the other slab half (see Fig. 5.3)(B). The two surfaces both need to be relaxed

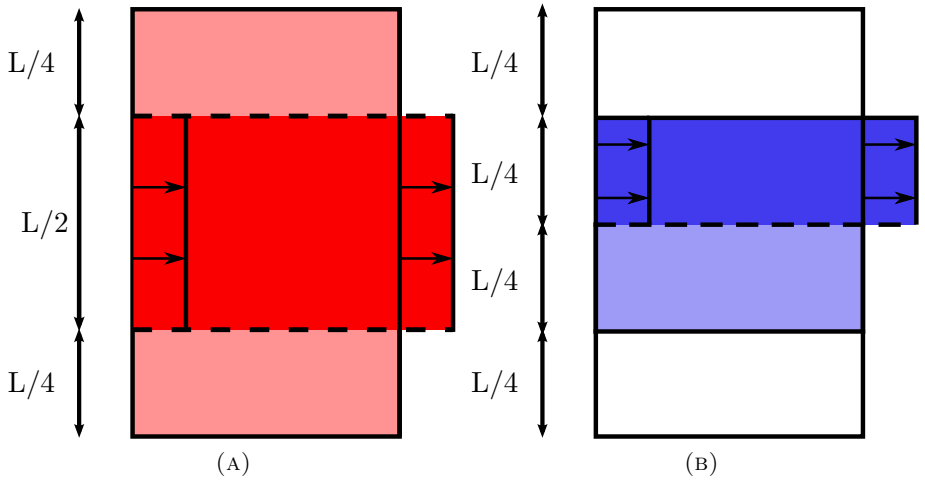



FIGURE 5.3: The two stacking fault system geometries I used to simulate $\gamma$-surfaces are the (A) bulk (B) and slab geometries. Regions containing atoms are red/blue in the bulk/slab system, and regions of vacuum are white. Displaced regions are coloured darker than regions that are not displaced. See the text in section 5.1.3 for more details.

and well separated from the SF to reduce interaction between these planar faults. In particular the relaxation of the surfaces significantly increases the computational cost of using the slab compared with the bulk geometry.

The slab geometry was used to simulate the pyramidal I $\gamma$-surface because it is not possible to form all SFs as identical pairs in the bulk geometry cell described above. Consider taking the pyramidal I superplane stacking sequence and displacing one A superplane to the C configuration forming an $I_1$ SF $H|C$:

$$\ldots EFGHABCD\cdots \rightarrow \ldots EFGH|C|BCD\ldots. \tag{5.1}$$

The other fault formed $C|B$ is not the same fault, but $I_2$. Because there are two distinct SFs in this system it is impossible to extract the SFE of each individual fault from this system. This shows that when translating one superplane it is not possible to form $I_1$ in the pyramidal I bulk geometry without forming $I_2$ as well. Since all neighbouring superplanes are related by the same translation vector it follows that forming $I_1$ in the bulk geometry will always form $I_2$ regardless of how many superplanes are translated.

The smallest rectangular repeat cell in the $(1\bar{1}0\bar{1})$ plane is bounded by $(1/3)[11\bar{2}0]$ and $[1\bar{1}02]$ lattice vectors. This cell also contains two lattice sites. Another important consideration when constructing the $(1\bar{1}0\bar{1})$ pyramidal I plane supercell is that the normal to this plane is not a lattice vector. To satisfy periodic boundary conditions only lattice

vectors can be used to construct the supercell. Because of this I chose the third lattice vector to be $[\bar{3}03\bar{2}]$ which is about 7.17° from the $(1\bar{1}0\bar{1})$ plane normal for the Ti0 $c/a$ ratio of 1.592.

### 5.1.4 Convergence tests

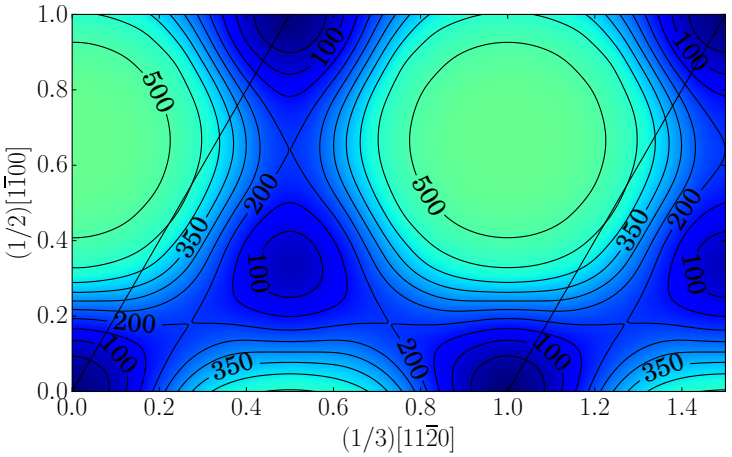
To verify the model of bulk $\alpha$-Ti built using LAMMPS [123] and Ti0 [9] I performed a full relaxation of the hcp primitive unit cell to obtain equilibrium values of the a-lattice parameter, cohesive energy, and $c/a$ ratio. I then compared these values with the results of Ackland and the fitting data for the LAMMPS version of the potential [9, 10]. The a-lattice parameter, cohesive energy, and $c/a$ ratio all agreed to within $10^{-3}$% as shown in table 5.1.

The Ti0 calculations described in this section were used to estimate the convergence parameters for subsequent DFT calculations of the basal and pyramidal I $\gamma$-surfaces. To converge the system size for the Ti0 calculations I varied the number of basal, prism, and pyramidal I planes used to compute the corresponding $\gamma$-surfaces. For efficient and accurate SFE measurements there must be as few atoms as possible, but also enough to reduce planar fault interaction energies below a required tolerance.

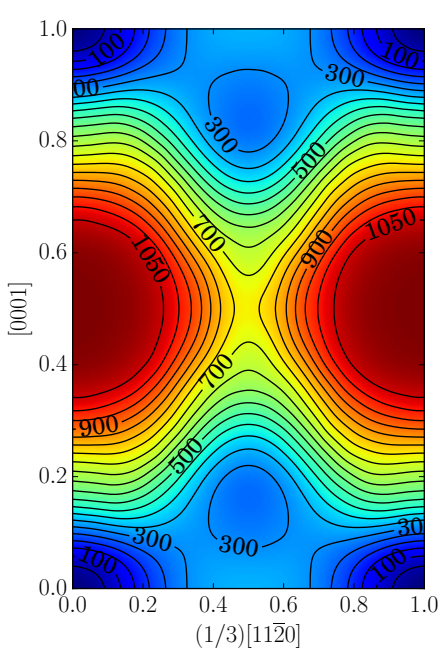
I converged the system size with respect to the $I_2$ SFE for the basal system, the energy of the SF located at $(1/6)[11\bar{2}0] + (1/2)[0001]$ labelled $F_1$ for the prism system, and the global maximum of the $\gamma$-surface for the pyramidal I system $(0.33)[1\bar{1}02]$. The basal SFE was accurate to within 0.1% for a system of 6 atoms or basal planes for the bulk geometry. The prism SFE was accurate to within 1% for a system of 38 prism planes for the bulk geometry. The pyramidal I global maximum SFE was accurate to within 0.1% for a system of 8 pyramidal I superplanes for the slab geometry. See tables 5.2 for the convergence test results.

### 5.1.5 Basal, prism, and pyramidal I $\gamma$-surfaces

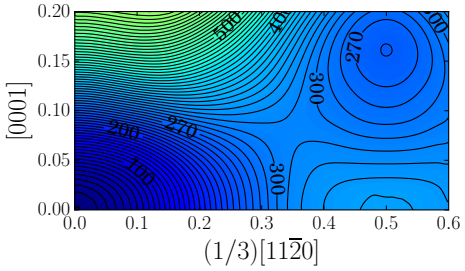
The basal $\gamma$-surface shown in Fig. 5.4 is in good agreement with those computed by Benoit *et al.* [127], Poty *et al.* [131], and Gershick *et al.* [113] using central-force potentials. There is one local minimum at $(1/3)[10\bar{1}0]$ (or $[0.5, 0.33]$ in coordinates



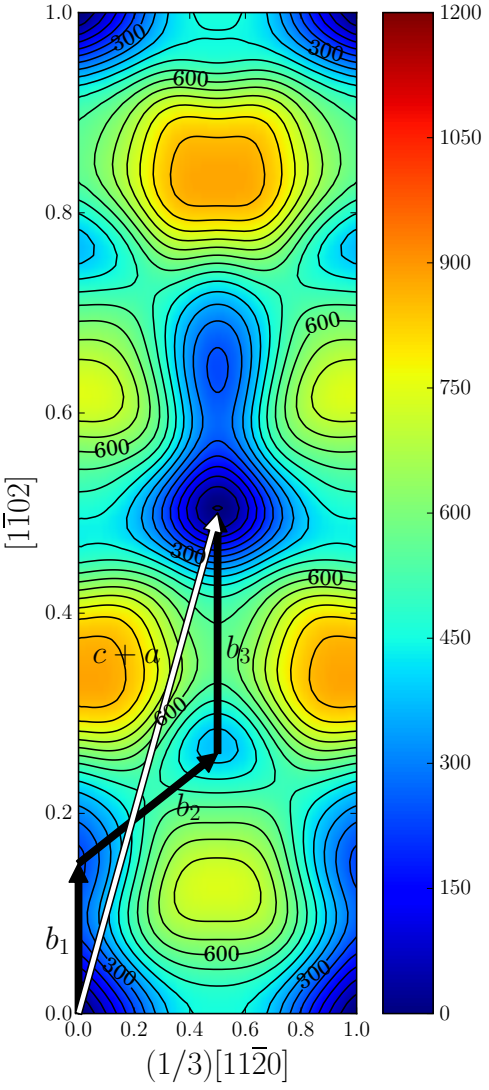

(A)




(B)




(C)




(D)

FIGURE 5.4: The basal (A), prism (B), and pyramidal I (D) $\gamma$-surfaces simulated using Ti0 [9]. In (C) a section of the prism $\gamma$-surface with a higher sampling density is plotted for a more detailed view of the $F_1$ stacking fault. Contour labels are in units of mJ/m$^2$. All heat plots use the colour scheme in the colour bar next to (D). (A) and (D) are based on Fig. 3(b) from [2] and Fig. 3 from [1] respectively.

| $N$atoms | $I_2$, mJ/m$^2$ |
|---|---|
| 6 | 63.930 |
| 14 | 63.841 |
| 22 | 63.841 |
| 30 | 63.842 |
| 38 | 63.841 |
| 46 | 63.842 |
| 54 | 63.842 |
| 62 | 63.850 |

(A) Basal

| $N$atoms | $F_1$, mJ/m$^2$ |
|---|---|
| 14 | 259.64 |
| 22 | 241.27 |
| 30 | 259.59 |
| 38 | 259.58 |
| 46 | 259.59 |
| 54 | 261.98 |
| 62 | 259.81 |
| 70 | 259.96 |

(B) Prism

| $N$atoms | Global Max, mJ/m$^2$ |
|---|---|
| 16 | 895.398 |
| 32 | 888.966 |
| 48 | 890.179 |
| 56 | 890.182 |
| 64 | 890.182 |
| - | - |
| - | - |
| - | - |

(C) Pyramidal I

TABLE 5.2: Stacking fault energies (SFEs) generated using Ti0 [9] on the basal, prism and pyramidal I planes. I varied the number of atoms ($N$atoms) in the system used to compute each SFE in order to converge the system size. Energies are in units of mJ/m$^2$. See section 5.1.4 for more details.

| Stacking faults | Basal | Prism | Pyramidal I | |
|---|---|---|---|---|
| | $I_2$ | $F_1$ | $I_1$ | $I_2$ |
| Position (x, y) | (0.5,0.33) | (0.5,0.16) | (0,0.15) | (0,0.77) |
| This work | 64 | 259 | 236 | 380 |
| Ackland [9] | 64 | - | 314 | 359 |
| Pasianot A [126] | 104 | - | - | - |
| Benoit CF [127] | 65 | 286 | - | - |
| Tarrat CF [128] | 54 | 342 | - | - |
| Experiment [129] | 310 | - | - | - |
| Experiment [130] | - | 150 | - | - |

TABLE 5.3: Stacking fault energies computed using Ti0 [9] on the basal, prism, and pyramidal I planes. These are compared with results in the literature computed using central force (CF) potentials, interatomic potentials with angular dependence (A), as well as experimental data. All energies are shown in mJ/m$^2$. Positions mark coordinates on the $\gamma$-surfaces in Fig. 5.4. Based in part on Tables 1 and 2 from [1].

on the $\gamma$-surface in Fig. 5.4(A)) with a SFE of 64 mJ/m$^2$ corresponding to the $I_2$ SF described in section 5.1.1. This energy is compared with other basal $I_2$ SFEs computed using central-force potentials in table 5.3. It is worth noting that this SFE is almost a factor of 5 smaller than the corresponding energy computed from experiment, as the results in table 5.5 show. This will be discussed further in this section and also in the DFT results section 5.2 of this chapter.

Figure 5.4(B) shows the $[10\bar{1}0]$ prism $\gamma$-surface formed between the widely-spaced prism

planes as described in section 5.1.1. This plane has been experimentally observed to be the plane of least resistance to **a**-type slip [14, Fig. 2.7], and is thus an important plane for the study of plastic deformation in $\alpha$-Ti. The saddle point $F_1$ located at [0.5,0.16] has a SFE of 259 mJ/m$^2$ in good agreement with other central-force potential results shown in table 5.3, but significantly higher than the value deduced experimentally from the core width of $a$-type dislocations on this plane [130].

As shown by the SFEs in table 5.3 the central-force potentials all predict that the basal $I_2$ SFE is lower than the prism $F_1$ SFE. The difference is striking, with $I_2$ being more than a factor of 6 lower than $F_1$ in the results of Tarrat *et al.* [128]. The underestimation of the $I_2$ basal SFE is a known feature of central-force potentials for the case of $\alpha$-Ti and has been discussed in previous publications [113, 127].

It has been shown that more accurate methods such as DFT and tight-binding (TB) can obtain the correct ordering of the basal and prism SFEs [127, 132–134]. Hence it is possible that the failing of the central-force potentials cited in table 5.3 is due to the inability of these potentials to describe the long-ranged character of bonding involving $d$-electrons in Ti as was first proposed by Legrand [132, 133].

Another reason for the discrepancy between the central-force potentials and the DFT and TB results is that the potentials were not fitted to the SFEs in question. This point was recently addressed by Mendelev *et al.* [49] in which the authors summarise the development of three embedded atom model potentials fitted to the $I_2$ and $F_1$ SFEs. A number of tests, including $\gamma$-surface results computed using these potentials, are summarised in section 5.3.

The pyramidal I $\gamma$-surface computed using Ti0 is shown in Fig. 5.4(D). Apart from perfect stacking at $[0, 0]$ and $[0.5, 0.5]$ there are two local minima on this $\gamma$-surface located at $[0, 0.15]$ and $[0.5, 0.27]$. These local minima correspond to the $I_1$ and $I_2$ SFs described in section 5.2, and their energies when fully relaxed are shown in table 5.3. My results are in qualitative agreement with those of Ackland [9] as shown in table 5.3. It is not clear why my results for the relaxed stacking fault energies $I_1$ and $I_2$ on the pyramidal I plane differ from those computed by Ackland.

The two stable SFs $I_1$ and $I_2$ on the pyramidal I $\gamma$-surface suggest a possible dissociation mechanism for **c+a** dislocations on this plane. On the pyramidal I $\gamma$-surface in Fig. 5.4,

the white arrow denotes the **c+a** vector at (0.5,0.5), and the black arrows show a set of vectors $\mathbf{b}_1$, $\mathbf{b}_2$, and $\mathbf{b}_3$ defined as:

$$\begin{aligned} \mathbf{b_1} &= \frac{1}{6}[01\bar{1}2] \\ \mathbf{b_2} &= \frac{1}{6}[2\bar{1}\bar{1}0] + \frac{1}{12}[01\bar{1}2] \\ \mathbf{b_3} &= \frac{1}{4}[01\bar{1}2]. \end{aligned} \tag{5.2}$$

These vectors lie between local minima of the $\gamma$-surface that add up to **c+a**. These black vectors are partial Burgers vectors describing a possible dissociation of the **c+a** Burgers vector. This dissociation has been observed in MD studies of **c+a** dislocations nucleating in Mg by Tang *et al.* [119] using the Mg IPs of Liu *et al.* [135] and Sun *et al.* [136]. Also a closely related dissociation of a **c+a** dislocation on the $\{11\bar{2}\bar{2}\}$ pyramidal II planes into two $(\mathbf{c}+\mathbf{a})/2$ dislocations has been proposed by Agnew *et al.* to explain their experimental results in Mg [137]. I will show in the following section 5.2 that this three-partial dissociation is not predicted by the DFT results because of the high SFE of the DFT $I_2$ fault.

## 5.2 Density functional theory studies

### 5.2.1 DFT parameters

All the DFT results in this chapter were obtained using CASTEP version 8.0 [8]. In this chapter I used two ultrasoft pseudopotentials for Ti [81], one with 12-valence states denoted by 12elPP and one with 4-valence states denoted by 4elPP as described in section 3.5. I used the PBE exchange-correlation functional [68] for all calculations.

The DFT parameters used in these simulations are detailed in section 4.2. In summary, I used a plane-wave energy cut-off of 480 eV for both pseudopotentials, a $23\times23\times15$ MP **k**-point sampling grid, and the cold smearing scheme with a smearing width of 0.1 eV. The lattice parameters used were $a = 2.94$ Å and $c/a = 1.580$. DFT relaxations were finished once the maximum force on any atom was lower than 10 meV/Å, and the total energy convergence was to within 0.01 meV/atom.

### 5.2.2 Convergence tests

The methods used to simulate the DFT $\gamma$-surfaces were the same as those used for the Ti0 $\gamma$-surfaces. Hence the bulk geometry was used to simulate the basal $\gamma$-surface and the slab geometry was used to simulate the pyramidal I $\gamma$-surface for the same reasons described in section 5.1.3.

The system size convergence tests carried out with Ti0 also helped to narrow down the range of system sizes that needed to be tested for the basal and pyramidal I systems. Hence systems containing $\{6, 10, 14, 18, 22, 26\}$ atoms were used to converge the basal supercell size and $\{16, 24, 32, 40, 48, 56, 64\}$ atoms systems were used for the size of the pyramidal I supercell. The results are shown in tables 5.4. I found that a supercell of 14 atoms for the basal system gave an $I_2$ SFE within 2% of those computed with larger cells. For a pyramidal I supercell the size convergence was carried out using the global maximum located at $0.4[1\bar{1}02]$ or $[0.0, 0.4]$ of the Ti0 $\gamma$-surface in Fig. 5.4(D). In this case 48 atoms or 12 superplanes resulted in a relaxation energy of this SF that was within 2% of the relaxation energies of two larger cells.

In addition to computing the relaxation energies of the $[0.0, 0.4]$ fault using the pyramidal I supercell, I also calculated the inter-planar spacings of the relaxed system for both pseudopotentials. As shown in Fig. 5.5, there is a large expansion at the fault, with contractions at the surface layers, and oscillations between the intermediate superplanes. As the system size increases these oscillations decay and almost vanish for the 16 superplane supercells. These results also show that the SF is reasonably well isolated for a system of 12 superplanes, especially in the case of the 12elPP. It is worth noting that a supercell containing 12 superplanes has 26.8 Å of vacuum between the slabs.

Using the mirror symmetry of the Ti0 basal $\gamma$-surface shown in Fig. 5.4(A) I sampled half of the full area of the $\gamma$-surface and generated the rest of the points using symmetry. Using Ti0 I determined the size of the sampling grid needed to accurately sample the whole basal $\gamma$-surface by using $6 \times 6$, $12 \times 12$, $24 \times 24$, and $48 \times 48$ sampling grids. I obtained sufficiently accurate sampling with the $12 \times 12$ grid. The mirror symmetry reduced the number of unique points to 78 points.

The pyramidal I $\gamma$-surface shown in Fig. 5.4(D) has a reflection symmetry with mirror plane along $(1/2)[11\bar{2}0]$, as well as a translational symmetry of $\mathbf{c+a}$. Hence only a

| Natoms | 12elPP |
|---|---|
| 6 | 326.9 |
| 10 | 314.9 |
| 14 | 306.0 |
| 18 | 303.4 |
| 22 | 301.2 |
| 26 | 302.7 |
| - | - |

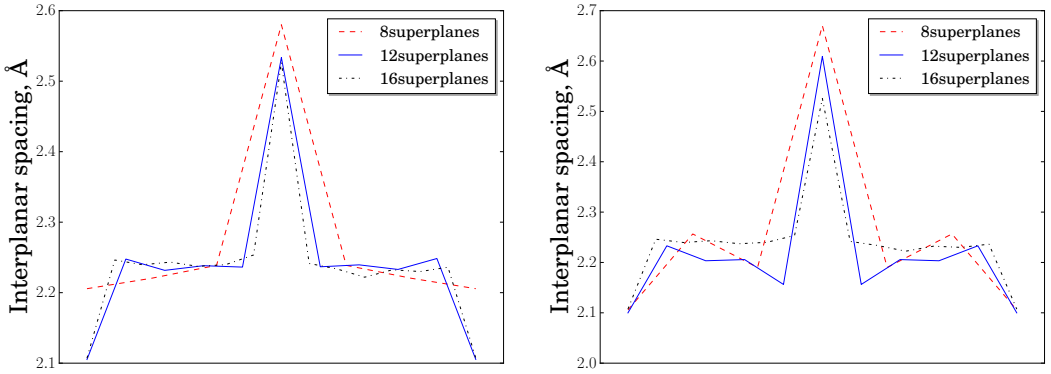
(A) Basal $I_2$ SFE in units of $mJ/m^2$

| Natoms | 12elPP | 4elPP |
|---|---|---|
| 16 | 1.59 | 1.56 |
| 24 | 1.57 | 1.50 |
| 32 | 1.67 | 1.38 |
| 40 | 1.65 | 1.32 |
| 48 | 1.48 | 1.28 |
| 56 | 1.47 | 1.29 |
| 64 | 1.45 | 1.26 |

(B) Pyramidal I unstable stacking fault relaxation energies, in units of eV

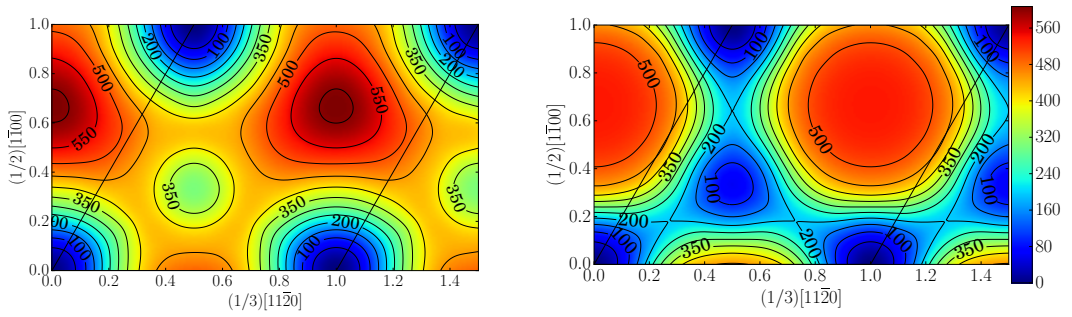
TABLE 5.4: DFT stacking fault energies generated on the basal and pyramidal I planes. I varied the number of atoms (Natoms) in the system used to compute each SFE in order to converge the system size. See section 5.2.2 for more details.

quarter of the pyramidal I $\gamma$-surface is unique, and the rest can be generated by these symmetry operations. The quarter spanned by the vectors $(1/6)[11\bar{2}0]$ and $\frac{1}{2}[1\bar{1}02]$ was simulated with the sampling grids $4 \times 12$, $6 \times 18$, and $8 \times 24$. I found that the $4 \times 12$ grid was accurate enough to reproduce the $\gamma$-surfaces of the finer sampling grids. To make the features of the resulting surface more smooth Fourier interpolation was used on the sampling grid of the full $\gamma$-surface. Due to the computational cost a coarser uniform grid of 24 points forming a subset of the full $4 \times 12$ grid was used to simulate the 12elPP pyramidal I $\gamma$-surface. The full $4 \times 12$ grid was used to simulate the 4elPP $\gamma$-surface.




(A) (B)

FIGURE 5.5: The interplanar spacings through slabs of 8, 12 and 16 superplanes after constrained relaxations. (A) shows the 12elPP results, and (C) shows the 4elPP results. From [2].



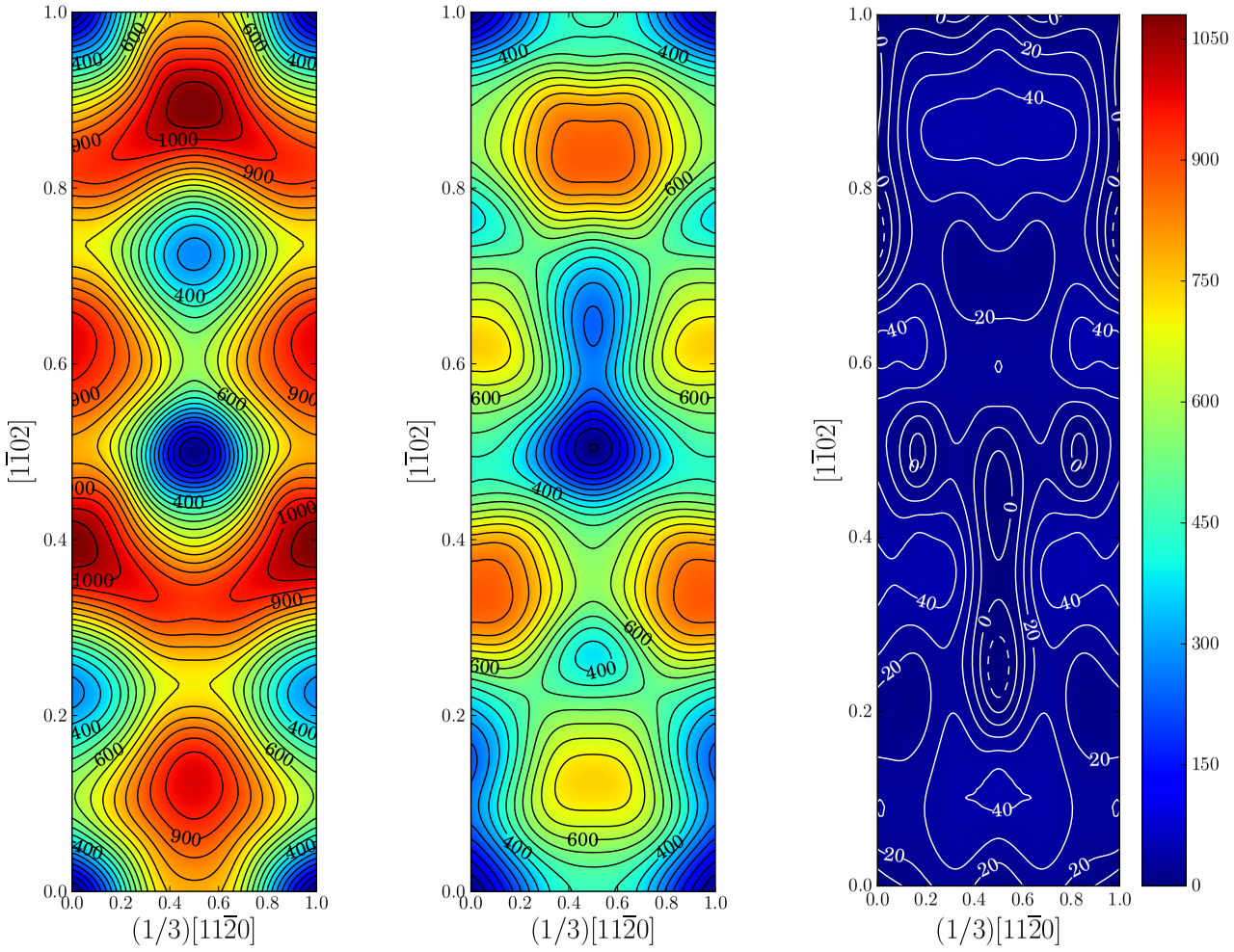

(A) (B)

FIGURE 5.6: The $\gamma$-surface for the basal plane calculated with (A) DFT with the 12elPP and (B) Ti0 [9]. The maxima and minima are in the same locations for both surfaces, but the energies are generally lower in the Ti0 surface. All energies are shown in mJ/m$^2$. A contour spacing of 50 mJ/m$^2$ was used. The basal plane unit cell is highlighted in black. From [2].

### 5.2.3 Basal and pyramidal I $\gamma$-surfaces

The basal $\gamma$-surface computed using the 12elPP is shown Fig. 5.6(A). The Ti0 $\gamma$-surface, plotted using the same data as Fig. 5.4(A), is shown in Fig. 5.6(B) for comparison. As pointed out by Benoit *et al.* [127] the Ti0 basal surface has deeper local minima than the DFT surface. The local minimum corresponding to the $I_2$ SF is at the same location $(1/3)[10\bar{1}0]$ or $[0.5, 0.33]$ on both $\gamma$-surfaces, and the energy of this fault is in good agreement with previous DFT calculations, as shown in table 5.5. Hence my results show a large discrepancy between the DFT and Ti0 $I_2$ SFEs as discussed in section 5.1.5 and previous publications [113, 127].

The pyramidal I $\gamma$-surface I computed using DFT with the 4elPP is shown in Fig. 5.7(A). The surface features are similar to those of the $\alpha$-Zr $\gamma$-surface computed by Chaari *et al.* [146], and also those of the full $\alpha$-Ti surface published by Liang *et al.* [144]. The pyramidal I $\gamma$-surface energies I obtained using the 12elPP were very similar to those of the 4elPP. The difference between these two samplings $\gamma_{12elPP}(\mathbf{t}) - \gamma_{4elPP}(\mathbf{t})$ on the coarse grid is shown in Fig. 5.7(C). This surface gives a measure of the error associated with using the 4elPP rather than the 12elPP. The entire surface is dark blue, indicating that this error is small over the entire surface. This is verified by the root mean square difference of 27 mJ/m$^2$. There are two maxima located at $[0, 0.4]$ and $[0.5, 0.12]$ where the energy difference reaches 40 mJ/m$^2$. The locations of all the local minima are the same for the 12elPP and 4elPP calculations.




(A) DFT (B) IP (C) Difference

FIGURE 5.7: Pyramidal I $\gamma$-surfaces computed using (A) DFT with the 4elPP and (B) Ti0 [9]. All energies are expressed in mJ/m$^2$, and the contours are separated by 50 mJ/m$^2$. The difference between the DFT $\gamma$-surfaces computed with the 4elPP and 12elPP is plotted in (C), where the contours are separated by 10 mJ/m$^2$. Contours of negative energy are shown by broken lines. From [2].

| | $I_2$ SFE ($mJ/m^2$) |
|---|---|
| DFT | |
| 12elPP (this work) | 306 |
| 10elPP [127] | 259 |
| 10elPP [138] | 292 |
| 10elPP [139] | 320 |
| 4elPP [138] | 322 |
| 4elPP [131] | 336 |
| 4elPP [140] | 292 |
| 4elPP [141, 142] | 307 |
| 4elPP [143, 144] | 309 |
| 4elPP [117] | 306 |
| Wu *et al.* [145] | 287 |
| TB | |
| Legrand [132, 133] | 290-370 |
| Experiment | |
| Partridge [107] | >300 |

TABLE 5.5: $I_2$ stacking fault energies on the basal plane computed in this work and elsewhere compared with experiment. All values quoted are DFT results apart from the results labelled tight-binding (TB) or Experiment. DFT results are labelled according to the number of valence electrons used in the pseudopotential where this information is known. Based on Table 1 from [2].

The DFT pyramidal I $\gamma$-surface can be compared with the Ti0 surface shown in Fig. 5.7(B) (plotted using the same data as Fig. 5.4(D)). The DFT surface has a local minimum at $[0.00, 0.22]$ which corresponds to the $I_1$ SF defined in sections 5.1.1 and 5.1.5. The DFT surface does not have a minimum corresponding to the fault $I_2$ at $[0.5, 0.26]$ on the Ti0 surface, but instead has a saddle point located at $[0.5, 0.23]$. I confirmed this by decreasing the contour spacing to 10 $mJ/m^2$ as shown in Fig. 5.8. Hence this SF is not stable when only relaxation normal to the fault is allowed.

The SFEs of the DFT pyramidal I surface are compared with published DFT results in table 5.6. The fault energies are given for (i) relaxation perpendicular to the fault plane only, and (ii) relaxations perpendicular and parallel to the plane allowed (labelled as 'Con' and 'Full' respectively in table 5.6). The fully relaxed $I_1$ SFE energies are 150 $mJ/m^2$ for the 4elPP and 163 $mJ/m^2$ for the 12elPP. It is worth noting that $I_1$ is about half the size of the stable basal SF $I_2$, and so is small compared with other DFT SFEs for $\alpha$-Ti in this study as shown in tables 5.5 and 5.6. I found the fully relaxed $I_2$

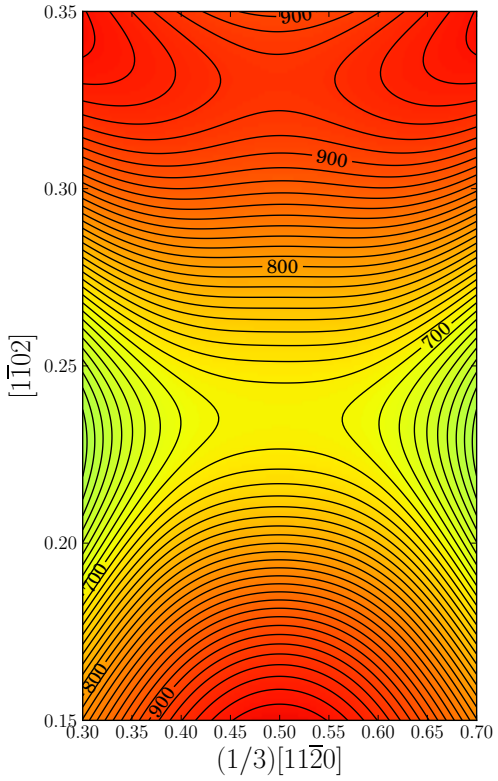



FIGURE 5.8: A section of the full DFT pyramidal I $\gamma$-surface shown in Fig. 5.7(A), with a refined contour spacing of 10 mJ/m$^2$. From this plot it is clear that the stationary point at [0.5,0.23] is a saddle point.

energies at $[0.5, 0.26]$ to be 700 mJ/m$^2$ for the 4elPP and 681 mJ/m$^2$ for the 12elPP. These energies are a little higher than those of Yin *et al.* [117] and Liang *et al.* [144].

As the results in table 5.6 show, the SFE of $I_1$ drops significantly once fully relaxed from its normal relaxed configuration, almost by a factor of two. I investigated this difference by comparing both atomic structures obtained from normal and full relaxation using the 12elPP. The differences were very small, the difference parallel to the $I_1$ fault plane being only $[0.00, 0.02]$ Å and a difference perpendicular to it of 0.10 Å facilitated by small local relaxations.

In contrast with $I_1$, the decrease in energy of the $I_2$ SF when going from normal to full relaxation is only 15%. Relaxations of this fault were slightly larger than the $I_1$ case with an expansion of the slab of 0.10 Å perpendicular to the fault. The differences along $[1\bar{1}02]$ were as large as 0.19 Å on either side of the geometrical fault plane, which decreases to 0.07 Å at the surfaces. To test the stability of the $I_2$ fault I displaced the

| | $I_1$ | | | $I_2$ | | |
|---|---|---|---|---|---|---|
| | Full | Con | Position | Full | Con | Position |
| 12elPP (this work) | 163 | 288 | [0,0.22] | 681 | 775 | [0.5,0.23] |
| 4elPP (this work) | 150 | 279 | [0,0.22] | 700 | 788 | [0.5,0.23] |
| 4elPP [142] | 148 | - | - | - | - | - |
| 4elPP [117] | 134 | - | [0,0.22] | 634 | - | [0.5,0.24] |
| 10elPP [143, 144] | 134 | 243 | [0,0.22] | - | - | - |

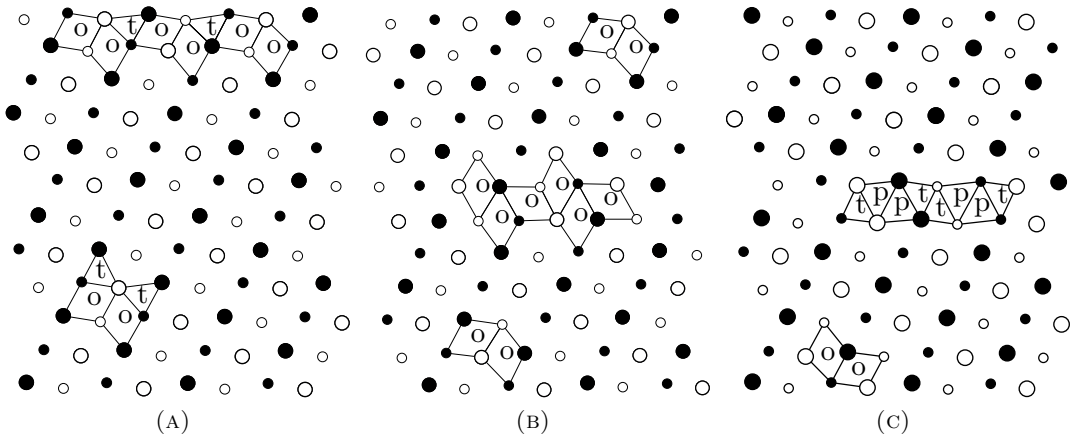
TABLE 5.6: The energies and $\gamma$-surface positions of the $I_1$ and $I_2$ intrinsic faults for the pyramidal I plane computed with DFT and three pseudopotentials, and with Ti0 [9]. 'Full' indicates an unconstrained ionic relaxation allowing atomic displacements parallel and normal to the fault plane. 'Con' indicates a constrained ionic relaxation allowing displacements only normal to the fault plane. The energies quoted for the $I_2$ fault with constrained DFT relaxation are for the unstable saddle point configuration in the $\gamma$-surface, which becomes a local minimum with full DFT relaxation. All energies in $mJ/m^2$. Based on Table 2 from [2].

normal relaxed $I_2$ structure by $[-0.1, 0]$ or $-(0.1)\mathbf{a}_1$ and then fully relaxed the resulting structure. It relaxed to $I_1$. This is in agreement with the results of Yin *et al.* [117] who found that the $I_2$ fault is stable after a small perturbation, but for perturbations greater than $3\%a$ the structure relaxes to $I_1$.

In order to better compare the above DFT results with Ti0 I also carried out the same relaxations of the Ti0 $I_1$ and $I_2$ SFs. The changes in the energies were much less for Ti0 than for the DFT calculations. The relaxation displacements of the constrained and fully relaxed systems generated with Ti0 differed by up to 0.11 Å for $I_1$ and 0.17 Å for $I_2$. These were relaxations parallel to the fault. Displacements perpendicular to the fault differed by less than 0.02 Å for both Ti0 faults.

The structure of the fully relaxed pyramidal I slab obtained with the 12elPP is shown in Figure 5.9(A). The structure is made up of contiguous arrays of octahedra and tetrahedra, examples of which are labelled by 'o' and 't'. The free $(1\bar{1}0\bar{1})$ surfaces of the slab relax inward by a small amount, and so their structure is made up of contiguous arrays of slightly distorted octahedra and tetrahedra.

The structure of the fully relaxed $I_1$ fault obtained with the 12elPP shown in Fig. 5.9(B) is different compared with the bulk of the unfaulted slab in Fig. 5.9(A). This atomic structure is made up of an array of adjoining octahedra labelled by 'o' with tetrahedra (not shown) occupying the remaining space. The superplanes neighbouring the fault are




(A) (B) (C)

FIGURE 5.9: Two periods of the fully relaxed (A) unfaulted slab, (B) $I_1$ fault, (C) $I_2$ fault, viewed in projection along $[11\bar{2}0]$ obtained from 12elPP calculations. (A) Local atomic structures in the bulk and surface regions are specified by octahedra and tetrahedra labels 'o' and 't' respectively. Circle sizes follow the same scheme as in Fig. 5.3. (B) The fault structure in the $I_1$ fault region is specified by octahedra labels 'o'. (C) The fault structure in the $I_2$ fault region is specified by trigonal prisms and tetrahedra labels 'p' and 't' respectively. From [2].

less rumpled than those in the bulk.

Figure 5.9(C) shows the $I_2$ fault's fully relaxed atomic structure obtained with the 12elPP. Because part of the displacement associated with this fault is along the direction of projection, the displacement transforms small circles into large circles and vice versa. Because of this the atomic structure of the fault differs significantly from that of $I_1$ and comprises an array of trigonal prisms and tetrahedra, shown by 'p' and 't'.

To investigate the discrepancy between the 4elPP and 12elPP pyramidal I $\gamma$-surfaces I looked for the smallest separations between the nuclei in the atomic configurations corresponding to the local maxima of the surface in Fig. 5.7(C). These points are $p_1 = [0, 4/11]$ and $p_2 = [1/2, 3/22]$. The smallest separations with the 4elPP for $p_1$ was 2.58 Å and for $p_2$ it was 2.71 Å, with each separation occurring at the fault. These separations are 0.3 Å and 0.17 Å smaller than the smallest perfect crystal separations of the nuclei.

I compared these separations with twice the core radius of the 4elPP. In the case of the 4elPP the core radius is 1.27 Å, so twice the core radius is 2.54 Å. Because the wavelength of electrons at 480 eV is 0.56 Å the 'core radius' of the 4elPP atom actually has a finite width of roughly 0.28 Å. Hence, when atoms come within 2.54+0.28 = 2.82 Å of each other the core and valence electrons begin to overlap significantly. Because both the separations 2.58 Å and 2.71 Å are less than 2.82 Å this is the most likely cause

of the difference between the 4elPP and 12elPP $\gamma$-surfaces. Because the points $p_1$ and $p_2$ correspond to local maxima of both the 12elPP and 4elPP pyramidal I $\gamma$-surfaces, they correspond to very high SFEs that are unlikely to be reached in low temperature plasticity of $\alpha$-Ti. Hence the 4elPP appears to be a good approximation of the 12elPP for describing physically relevant SFs in $\alpha$-Ti.

My results show that the dissociation of a **c+a** dislocation into two (**c+a**)/2 dislocations suggested by the $\gamma$-surface line sections of [138, 147] is not possible due to the absence of a stable SF at $[0.25, 0.25]$ in the $\gamma$-surface. A line section of the 4elPP pyramidal I $\gamma$-surface shown in Fig. 5.7(A) can be taken from $[0, 0]$ to $[0.5, 0.5]$, corresponding to the **c+a** Burgers vector, which is shown in Fig. 5.10. There is a local minimum along this line section at $[0.2, 0.2]$, but this is not a true minimum, as shown by the full $\gamma$-surface in Fig. 5.7(A). Because my values for the fully relaxed $I_1$ and $I_2$ SFEs agree with those of Yin *et al.* [117] and Wu *et al.* [148] my results support their conclusion that a **c+a** dissociation into three partial dislocations on the pyramidal I plane is unfavourable partially due to the high value of the $I_2$ SFE.

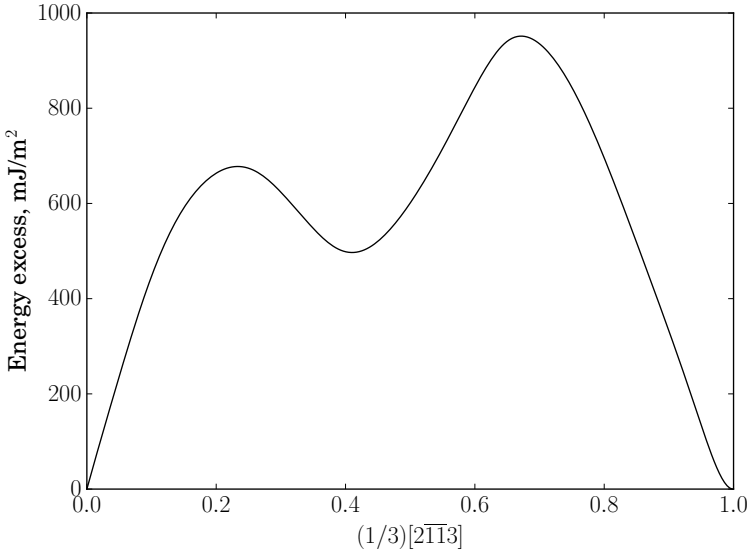



FIGURE 5.10: A line section of the 4elPP pyramidal $\gamma$-surface shown in Fig. 5.7(A) along the straight line between [0,0] and [0.5,0.5]. The point [0.5,0.5] on the $\gamma$-surface corresponds to a translation of $\frac{1}{3}[2\bar{1}\bar{1}3]$. From [2].

The authors Liang and Hardouin-Duparc recently proposed an alternative dissociation of the **c** + **a** dislocation into three partial dislocations [143, 144]. This suggestion is based on their simulations of the pyramidal I and pyramidal II $\gamma$-surfaces for $\alpha$-Ti using DFT with a 4elPP [143, 144]. The dissociation involves a Burgers vector corresponding to the $I_1$

SF with a similar energy to the result I computed as shown in table 5.6. The dissociation also involves the Burgers vectors $0.57(\mathbf{c}+\mathbf{a})$ on one of the $\{11\bar{2}2\}$ pyramidal II planes and $0.215\mathbf{a}$ on one of the narrowly spaced $\{1\bar{1}01\}$ pyramidal I planes. Further verification of this dissociation process would require computationally expensive DFT simulations of dissociation of the $\mathbf{c}+\mathbf{a}$ dislocation core.

## 5.3 Interatomic potential Ti1, Ti2, Ti3 tests

### 5.3.1 The interatomic potentials Ti-$\{1,2,3\}$

The IPs Ti1, Ti2, and Ti3 developed recently by Mendelev, Underwood, and Ackland (MUA) [49] are central force potentials like Ti0 [9]. These IPs were fitted to a number of DFT SFEs, including the DFT $I_2$ basal SFE of Benoit *et al.* [127]. To further assess the capability of Ti-$\{1,2,3\}$ I carried out SF and $\gamma$-surface calculations on the basal and pyramidal I planes using the same methods described in section 5.1. I also computed the root mean square (RMS) difference between the Ti-$\{1,2,3\}$ and DFT $\gamma$-surface data, as well as the RMS differences of their gradients. These RMS differences were also computed for the Ti0 IP used in the previous two sections 5.1 and 5.2 for comparison.

### 5.3.2 $\gamma$-surfaces and stable stacking fault energies

Using the same methods described in section 5.1 I computed the basal and pyramidal I $\gamma$-surfaces using the Ti-$\{1,2,3\}$ IPs. The resulting surfaces are shown in Figs. 5.11 and 5.12. I also included the DFT basal and pyramidal I surfaces identical to those in Figs. 5.6(A) and 5.7(A) for comparison.

The four $\gamma$-surfaces in Figs. 5.11 have a stable $I_2$ SF located at [0.5,0.33]. The fully relaxed $I_2$ SFEs are shown in table 5.7 including the corresponding value for Ti0, and are in good agreement with those of MUA [49]. Because the DFT $I_2$ SFE of 306 mJ/m$^2$ from Benoit *et al.* [127] was used in the fitting procedure of Ti-$\{1,2,3\}$, the agreement between the $I_2$ values of the Ti-$\{1,2,3\}$ and the DFT is much closer than the agreement between the Ti0 and DFT values.

| Fault | Ti0 | Ti1 | Ti2 | Ti3 | DFT |
|---|---|---|---|---|---|
| Basal $I_2$ | 64 | 255 | 234 | 235 | 306 |
| | [0.5,0.33] | [0.5,0.33] | [0.5,0.33] | [0.5,0.33] | [0.5,0.33] |
| Pyr. $I_1$ | 225 | 197 | 218 | 191 | 163 |
| | [0,0.15] | [0,0.15] | [0,0.17] | [0,0.17] | [0,0.22] |
| Pyr. $I_2$ | 359 | 655 | 494 | 472 | 681 |
| | [0.5,0.27] | [0.5,0.27] | [0.5,0.27] | [0.5,0.27] | [0.5,0.23] |

TABLE 5.7: Stable SFEs and their positions on the basal and pyramidal I $\gamma$-surfaces computed using the IPs and DFT. All energies are expressed in mJ/m$^2$. All positions are expressed as fractions of the lattice vectors along the $x$- and $y$-axes of the $\gamma$-surfaces in Figs. 5.11 and 5.12.

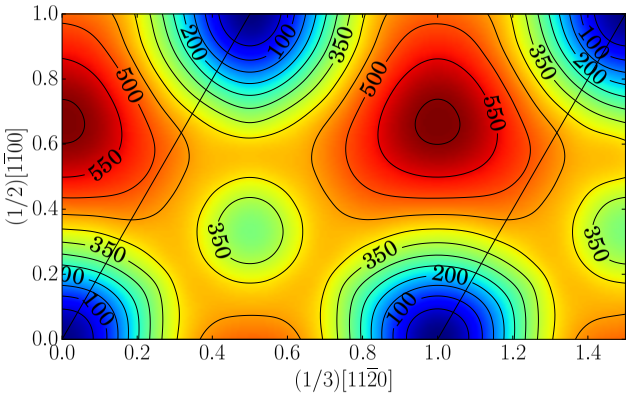
Another distinct feature of the $\gamma$-surfaces shown in Figs. 5.11 is the stationary point at $(2/3)[10\bar{1}0]$ or [1.00,0.66]. This is a global maximum of the DFT and Ti0 surfaces (see Fig. 5.6), but is a local minimum of the Ti-$\{1,2,3\}$ surfaces (see Fig. 5.11). Because this feature is present in the high energy region of all of the $\gamma$-surfaces it should not directly affect the accuracy of the potentials in the low energy region. This will be addressed in the following section 5.3.3.

The $\gamma$-surfaces on the pyramidal I plane computed with Ti-$\{1,2,3\}$ and DFT are shown in Fig. 5.12. The locations and SFEs of the $I_1$ fault are slightly different, as seen in table 5.7. The $I_2$ SFEs in computed with Ti-$\{1,2,3\}$ are in better agreement with the DFT than that of Ti0, especially that of Ti1. The IPs Ti-$\{1,2,3\}$ also describe $I_2$ as a stable SF in agreement with DFT. Two of the local maxima in the DFT $\gamma$-surface are split into two local maxima in the Ti1 $\gamma$-surface. Nonetheless the agreement between the Ti$\{1,2,3\}$ and DFT $\gamma$-surfaces is quite good despite the pyramidal I $\gamma$-surface being absent from the fitting procedure of the Ti-$\{1,2,3\}$ potentials.

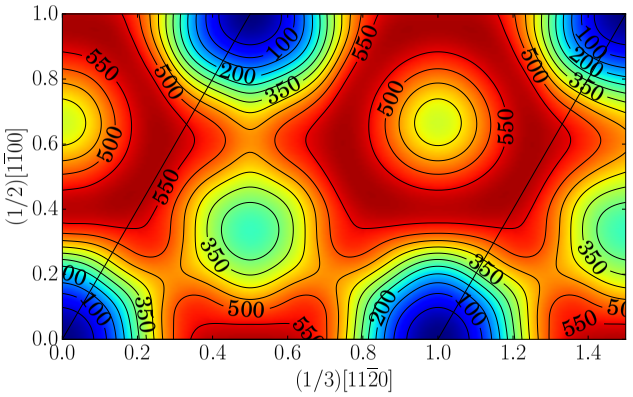
### 5.3.3 $\gamma$-surface differences

To quantify the difference between the $\gamma$-surface energies shown in Figs. 5.11 and 5.12 I computed the root-mean-square (RMS) difference between the IP and DFT $\gamma$-surfaces for IPs Ti0 and Ti-$\{1,2,3\}$.

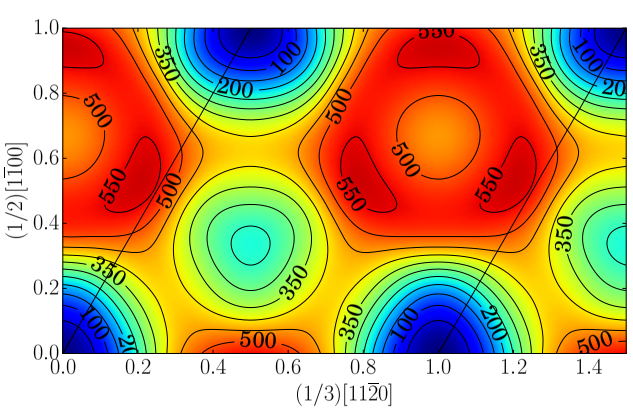
As described in section 5.1.3 each $\gamma$-surface is spanned by two lattice vectors $\mathbf{a}_1$ and $\mathbf{a}_2$. I used $\mathbf{a}_1 = (1/3)[11\bar{2}0]$ and $\mathbf{a}_2 = (1/3)[2\bar{1}\bar{1}0]$ for the basal $\gamma$-surfaces and $\mathbf{a}_1 = (1/3)[11\bar{2}0]$



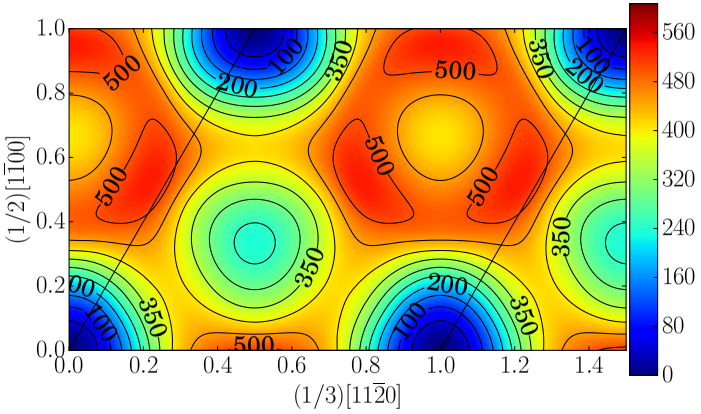

(A) Basal - DFT




(B) Basal - Ti1

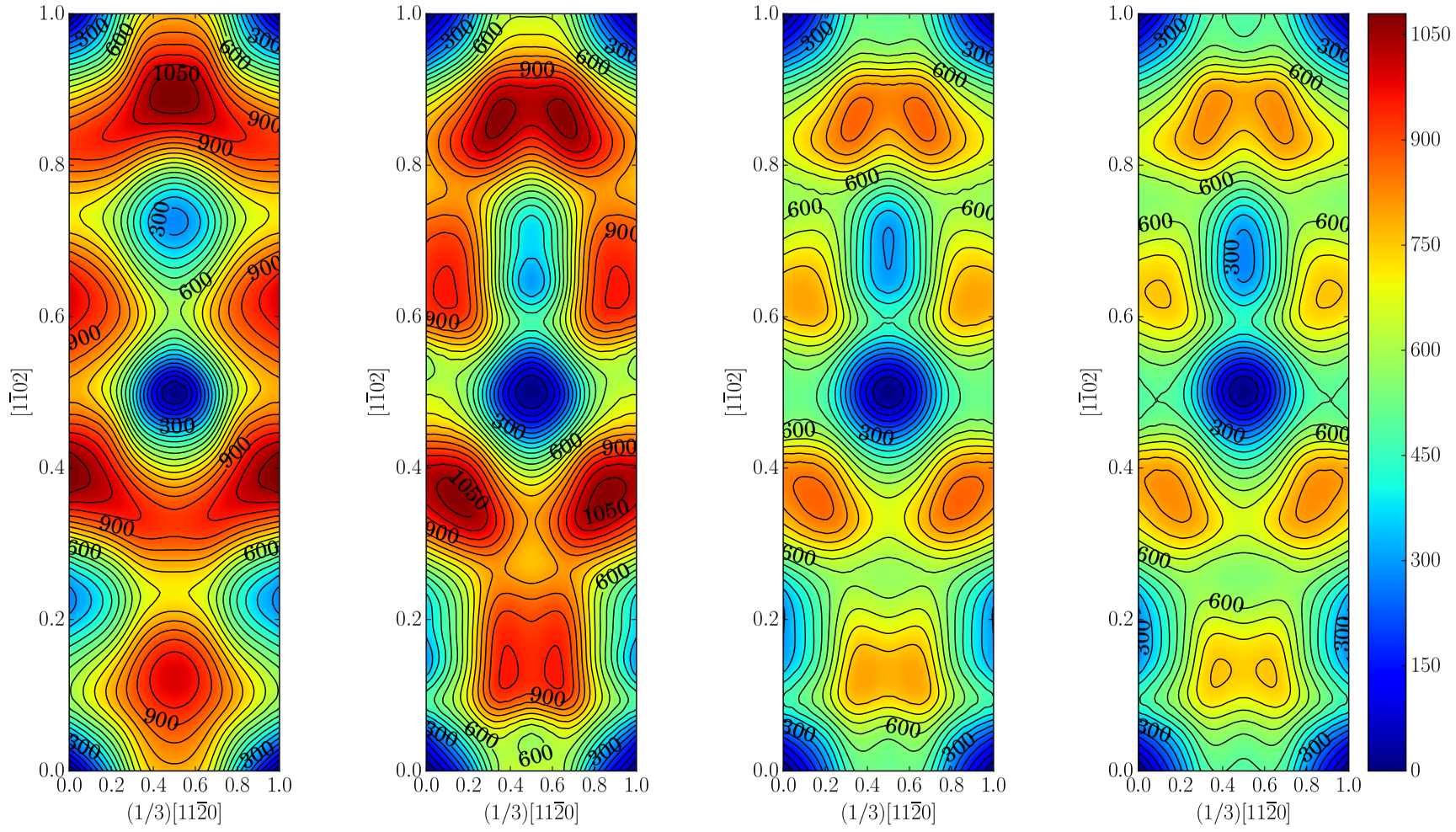



(C) Basal - Ti2




(D) Basal - Ti3

FIGURE 5.11: The basal $\gamma$-surfaces of $\alpha$-Ti generated using the Ti-$\{1,2,3\}$ IPs and DFT. All energies are expressed in mJ/m$^2$, and contours are separated by 50 mJ/m$^2$.




(A) Pyramidal I - DFT (B) Pyramidal I - Ti1 (C) Pyramidal I - Ti2 (D) Pyramidal I - Ti3

FIGURE 5.12: The pyramidal I $\gamma$-surfaces of $\alpha$-Ti generated using the IPs and DFT. All energies are expressed in mJ/m$^2$, and contours are separated by 50 mJ/m$^2$.

and $\mathbf{a}_2 = [1\bar{1}02]$ for the pyramidal I $\gamma$-surfaces. I sampled the surfaces using a discrete mesh of points $\mathbf{t}_{ij}$ such that:

$$\mathbf{t}_{ij} = \frac{i}{M}\mathbf{a}_1 + \frac{j}{N}\mathbf{a}_2, \tag{5.3}$$

where $i = \{0, 1, \ldots, M-1\}$, $j = \{0, 1, \ldots, N-1\}$. For all calculations in this section I used $M = N = 12$ for the basal sampling mesh and $M = 7$, $N = 23$ for the pyramidal I sampling mesh as described in section 5.2.2. The $\gamma$-surface energies at these sample points are expressed in mJ/m$^2$ as $\gamma_{ij} = \gamma(\mathbf{t}_{ij})$, and all distances in this section are expressed in Å. The RMS difference between an IP and a DFT $\gamma$-surface with samples $\gamma^{IP}$ and $\gamma^{DFT}$ respectively was computed using the following relation:

$$\Delta_{RMS} = \sqrt{\frac{1}{MN}\sum_{i=0}^{M-1}\sum_{j=0}^{N-1}\left(\gamma_{ij}^{DFT} - \gamma_{ij}^{IP}\right)^2}. \tag{5.4}$$

As shown in table 5.13(A), Ti0 has the largest RMS difference compared with the DFT basal and pyramidal I $\gamma$-surfaces. The lowest RMS differences for the basal $\gamma$-surface are between the Ti2 and Ti3 samples and those of DFT, and the lowest for the pyramidal I surfaces are between Ti1 and DFT.

A major contribution to the basal RMS differences in table 5.13(A) is the stationary point at [1.00,0.66] described in the previous subsection 5.3.2. Even though this point is unlikely to affect plastic deformation at low temperatures, it does significantly affect the RMS differences between Ti0, Ti-$\{1, 2, 3\}$ and the DFT values. To reduce the effects of higher energy SFEs I weighted each SFE sample with a Boltzmann factor of the form:

$$w_{ij} = \frac{1}{Q}e^{-\gamma_{ij}/\rho_E} \quad ; \quad Q = \frac{1}{MN}\sum_{i=0}^{M-1}\sum_{j=0}^{N-1} e^{-\gamma_{ij}/\rho_E}, \tag{5.5}$$

where $i = \{0, 1, \ldots, M-1\}$, $j = \{0, 1, \ldots, N-1\}$, and $\rho_E$ is an energy per unit area that determines how the RMS differences are weighted by the $w_{ij}$. The weighting was carried out by pre-multiplying each $\gamma$-surface sample by the corresponding weighting factor $\gamma_{ij} \rightarrow w_{ij}\gamma_{ij}$ for all $i, j$. These weighting factors reduce the contribution of samples with high SFEs, and increase the contribution of samples with low SFEs. I used $\rho_E = 300$ mJ/m$^2$ for both the basal and pyramidal I cases.

The weighted RMS differences are shown in table 5.13(B). There is a significant reduction in all of the RMS differences compared with the un-weighted values. In particular the

basal RMS differences for all the IPs decrease by about 40-50 mJ/m$^2$ upon weighting compared with the DFT data. The weighting appears to show that the potentials Ti-$\{1, 2, 3\}$ do significantly improve on Ti0 when describing the basal $\gamma$-surface at low SFEs.

Weighting the pyramidal I $\gamma$-surface samples decreases all of the RMS differences as shown in table 5.13(B). The values of Ti-$\{1, 2, 3\}$ are within about 20 mJ/m$^2$ of each other, and the value of Ti0 is about 30 mJ/m$^2$ higher than the Ti-$\{1, 2, 3\}$ values. Hence applying the Boltzmann weighting creates a significant gap between the RMS differences corresponding to Ti0 and the Ti-$\{1, 2, 3\}$ IPs. Of the IPs Ti-$\{1, 2, 3\}$, Ti2 has the lowest RMS difference for the basal case and Ti1 has the lowest RMS difference for the pyramidal I case.

| RMS differences (mJ/m$^2$) | Ti0 | Ti1 | Ti2 | Ti3 |
|---|---|---|---|---|
| Basal | 107 | 87 | 57 | 62 |
| Pyramidal I | 236 | 116 | 172 | 190 |

(A)

| RMS Boltzmann (mJ/m$^2$) | Ti0 | Ti1 | Ti2 | Ti3 |
|---|---|---|---|---|
| Basal | 68 | 34 | 17 | 18 |
| Pyramidal I | 135 | 86 | 99 | 106 |

(B)

FIGURE 5.13: The root-mean-square difference between samples of the IP and DFT $\gamma$-surfaces. (A) shows the RMS differences between $\gamma$-surface samples, and (B) shows the RMS differences with samples weighted by the Boltzmann factor in (5.5).

### 5.3.4 $\gamma$-surface gradient differences

As described in the introduction of this chapter, the slope of the $\gamma$-surface corresponding to a particular slip plane is related to the force constricting the core of a dislocation on this slip plane. The balance of this force and the force resulting from the elastic energy of the dislocation determines the dislocation core width [116]. To investigate the capability of these IPs to model this property I computed the RMS difference between the IP and DFT $\gamma$-surface gradients to test the IPs Ti-$\{1, 2, 3\}$. The expression I used to compute the RMS difference between the gradients of the IP and DFT $\gamma$-surface samples is similar

to equation (5.4):

$$\frac{\Delta_{RMS}^{\text{Gradient}}}{\overline{|\nabla\gamma_{DFT}|}} = \frac{1}{\overline{|\nabla\gamma_{DFT}|}}\sqrt{\frac{1}{MN}\sum_{i=0}^{M-1}\sum_{j=0}^{N-1}\left[\nabla^2(\gamma_{ij}^{DFT}-\gamma_{ij}^{IP})\right]}, \tag{5.6}$$

where the laplacian was computed as $\nabla^2 = \frac{\partial^2}{\partial x^2} + \frac{\partial^2}{\partial y^2}$. The expression in (5.6) returns a single number expressed as a percentage of $\overline{|\nabla\gamma_{DFT}|}$, the average absolute value of the corresponding DFT $\gamma$-surface gradient. The methods used to compute the $\gamma$-surface gradients are described in appendix A.

As shown in table 5.14(A), the basal RMS gradient differences are all within about 70-100% of the average slope of the corresponding DFT $\gamma$-surface, where Ti2 and Ti3 have the smallest RMS differences and Ti1 has the largest. The pyramidal I RMS gradient differences are generally smaller percentages of the average DFT slope, with Ti0 having the largest value, and Ti2 having the smallest value.

| RMS differences (%) | Ti0 | Ti1 | Ti2 | Ti3 |
|---|---|---|---|---|
| Basal | 85.7 | 100.0 | 73.8 | 73.2 |
| Pyramidal I | 77.6 | 60.9 | 52.5 | 56.9 |

(A)

| RMS Boltzmann (%) | Ti0 | Ti1 | Ti2 | Ti3 |
|---|---|---|---|---|
| Basal | 95.3 | 83.1 | 62.7 | 58.9 |
| Pyramidal I | 101.4 | 71.4 | 65.5 | 74.1 |

(B)

FIGURE 5.14: RMS differences between gradients of the IP and DFT $\gamma$-surfaces expressed as a percentage of the average slope of the corresponding DFT $\gamma$-surface. (A) shows the RMS gradient differences between $\gamma$-surfaces samples, and (B) shows the RMS gradient differences with samples weighted by the Boltzmann factor in (5.5).

I used the same weighting procedure described in the previous section 5.3.3 for the RMS gradient differences as shown in table 5.14(B). The weights still depend on the sample energies, not their gradients, so samples with high SFEs contribute less to the RMS gradient difference, and samples with low SFEs contribute more upon weighting. For the basal case the RMS gradient difference of Ti0 increases, and the values of Ti-$\{1, 2, 3\}$ decrease upon weighting. This changes the ordering of Ti0 and Ti1 compared with the un-weighted RMS differences in table 5.14(A).

The pyramidal I RMS gradient differences all increase when weighted $\gamma$-surface samples are used compared with un-weighted samples. This implies that the differences between the IP and DFT gradients at low SFEs are larger than at higher SFEs. As was the case for the Pyramidal I RMS gradient differences without weighting Ti2 has the lowest RMS difference and Ti0 has the highest RMS difference after weighting as well.

These results show that the new IPs Ti-$\{1, 2, 3\}$ developed by MUA [49] offer improvements over the original potential Ti0 developed by Ackland [9]. All three IPs predict stable SFEs on the basal and pyramidal I planes that are closer to the DFT values than those of Ti0. In particular Ti2 and Ti3 both show good agreement with DFT in the form of low RMS differences between the basal and pyramidal I $\gamma$-surfaces and their gradients.

It is worth noting that although Ti2 and Ti3 show the best agreement with DFT results according to the RMS differences, Ti1 predicts a lower prism SFE than the $I_2$ basal SFE in agreement with experiment and DFT [49]. Hence the choice between Ti1 and Ti-$\{2, 3\}$ requires choosing between correct stable SFE ordering on the basal and prism planes, and better overall agreement with the DFT $\gamma$-surfaces.

# Chapter 6

# Point defects in titanium

As described in chapter 1 the main motivation for the work described in this thesis is the problem of cold dwell fatigue (CDF). The work in this chapter is motivated by the strong effect Mo has on the CDF susceptibility of Ti-alloys that include Mo as an alloying element. Qiu *et al.* [26] suggested that the influence of Mo on CDF susceptibility is at the microstructural scale. Another hypothesis proposed in chapter 1 is that Mo influences the CDF susceptibility at the atomic scale by trapping vacancies in $\alpha$ grains thus reducing creep relaxation and preventing the large stress concentrations at hard grains known to cause CDF failure.

I tested this hypothesis by computing formation and binding energies between Mo-atoms and vacancies. Some of these quantities have been calculated before. Huang *et al.* [149] computed formation and stabilisation energies of transition metal elements, including Mo in the $\alpha, \beta$ and $\omega$ phases. The focus of their work was understanding the influence of transition metal elements on phase diagrams. Tegner *et al.* [99] studied the effect of alloying elements, including Mo, on the phase stability of Ti alloys and showed that the stabilisation of the $\beta$-phase is correlated with the filling of the $d$-band. Nevertheless I calculated these quantities again for consistency and completeness of the results, and as a check for my own simulations.

The chapter begins with a description of the simulation methods as well as convergence tests of the supercell sizes that I used in the calculations. Then the results pertaining to the Ti-vacancy, the Mo interstitial, the Mo substitutional, and the Mo-vacancy binding energy are summarised and discussed. Finally, a mechanism addressing the temperature

dependence of CDF is summarised. The mechanism was suggested by Sutton in the work by Ready, Haynes, Grabowski, Rugg, and Sutton [4].

## 6.1 Methods

### 6.1.1 DFT parameters

As stated in section 3.5 all calculations in this chapter were computed using VASP version 5.3.5 [84–87]. I used the 10elPP PAW pseudopotential for Ti and a Mo PAW potential with 6 valence electrons, as included in the VASP database [83, 103, 104]. I used the PBE parameterisation of the exchange-correlation functional for most calculations in this chapter, and where stated I used the parameterisation of Perdew and Wang (PW91) [69].

Based on the convergence tests in section 4.2 I used a plane wave energy cut-off of 350 eV for all calculations in this chapter, and I used a $23 \times 23 \times 15$ Γ-centred Monkhorst-Pack (MP) **k**-point mesh for the primitive unit cell. For this **k**-point mesh the product of the total number of **k**-points in the first Brillouin zone and the number of atoms in the unit cell is about 16,000. In order to preserve this sampling density I ensured that all other **k**-point samplings were equivalent to or greater than this product. Methfessel-Paxton smearing was used with a smearing width of 0.1 eV.

DFT ionic relaxations were finished once the maximum force on any atom was lower than 10 meV/Å, and the total energy convergence was to within 0.005 meV/atom.

### 6.1.2 Supercell size effects in point defect calculations

The use of periodic boundary conditions causes elastic and electronic interactions to occur between a point defect in the supercell and its periodic images. The effects of these interactions on the computed total energies can be lessened to a desired level by using a larger supercell and by choosing a suitable **k**-point mesh. I used Γ-centred MP **k**-point meshes with an odd number of **k**-points along each reciprocal direction.

| Supercell | no. atoms | MP mesh | kp×atom | $E^{\mathrm{f}}$ | $E^{\mathrm{coh}}$ |
|---|---|---|---|---|---|
| $2 \times 2 \times 2$ | 15 | $13 \times 13 \times 9$ | 22,815 | 2.13 | 7.8897 |
| $3 \times 3 \times 2$ | 35 | $9 \times 9 \times 9$ | 25,515 | 2.13 | 7.8899 |
| $3 \times 3 \times 3$ | 53 | $9 \times 9 \times 7$ | 30,051 | 2.13 | 7.8901 |
| $4 \times 4 \times 2$ | 63 | $7 \times 7 \times 9$ | 27,783 | 2.15 | 7.8900 |
| $4 \times 4 \times 3$ | 95 | $7 \times 7 \times 7$ | 32,585 | 2.16 | 7.8901 |

TABLE 6.1: Vacancy formation energies ($E^{\mathrm{f}}$) in $\alpha$-Ti and cohesive energies ($E^{\mathrm{coh}}$) of the perfect hcp crystal in eV computed for different supercell sizes. MP mesh is the Monkhorst-Pack mesh of **k**-points. kp×atom is the number of **k**-points multiplied by the number of atoms in the supercell used for comparisons between the **k**-point sampling for different supercells.

I investigated the influence of the supercell on the formation energy of the vacancy in $\alpha$-Ti by computing the formation energy for a number of supercell sizes (see table 6.1). During the energy minimisation the supercell vectors were held fixed. The supercell size is specified using the notation $m \times n \times p$, where $m$, $n$, and $p$ define the numbers of hcp primitive vectors **a**, **b**, and **c** as described in section 4.1. As table 6.1 shows, I found that a $2 \times 2 \times 2$ supercell of 15 atoms converged the formation energy to within 0.03 eV. My computed formation energies are compared with other values in the literature in section 6.2.

To further test the convergence of my calculations with respect to supercell size I computed the formation energy of the octahedral self-interstitial in $\alpha$-Ti and compared those energies with those of Vérité *et al.* [11]. The results in table 6.2 show that my results and those of Vérité *et al.* differ by less than 3%. Because my results were in good agreement with those of Vérité *et al.* [11] I also found that the $6 \times 6 \times 4$ supercell was large enough to achieve convergence of the self-interstitial formation energy. Hence I used a $6 \times 6 \times 4$ supercell for calculating the formation energies of the interstitial and substitutional Mo atoms in $\alpha$-Ti, as well as the binding energy between a Mo substitutional atom and a vacancy in $\alpha$-Ti.

| Supercell | no. atoms | MP mesh | kp×atom | $E^{\mathrm{f}}$ | Ref. [11] |
|---|---|---|---|---|---|
| $5 \times 5 \times 4$ | 201 | $5 \times 5 \times 3$ | 15,075 | 2.58 | - |
| $6 \times 6 \times 4$ | 289 | $5 \times 5 \times 3$ | 21,675 | 2.46 | 2.40 |
| $6 \times 6 \times 5$ | 361 | $5 \times 5 \times 3$ | 27,075 | 2.47 | 2.40 |

TABLE 6.2: Self-interstitial formation energies in $\alpha$-Ti computed as part of this study and compared with those of Vérité *et al.* [11].

### 6.1.3 The formation energies of a Mo-atom in $\alpha$ and $\beta$-phases of Ti

Define $E(N_{\mathrm{Ti}}, \mathrm{Mo})$ as the total energy for a supercell containing $N_{\mathrm{Ti}}$ titanium atoms in the $\alpha$- or $\beta$-phases and a Mo atom occupying either a substitutional or interstitial site. Then the formation energy of a Mo point defect can be defined as follows [150]:

$$E^{\mathrm{f}} = E(N_{\mathrm{Ti}}, \mathrm{Mo}) - N_{\mathrm{Ti}}\mu_{\mathrm{Ti}} - \mu_{\mathrm{Mo}}, \tag{6.1}$$

where $\mu_{\mathrm{Ti}}$ and $\mu_{\mathrm{Mo}}$ are the chemical potentials of Ti and Mo respectively. I have defined $\mu_{\mathrm{Mo}}$ to be the total energy per atom of Mo in its equilibrium bcc crystal structure. I defined $\mu_{\mathrm{Ti}}$ to be the total energy per atom in a supercell of $\alpha$- or $\beta$-Ti with the same supercell dimensions as the supercell containing the defect and with the same **k**-point sampling.

Defining $\mu_{\mathrm{Mo}}$ as the total energy per atom of bcc-Mo is only appropriate if the Ti-alloy coexists in equilibrium with bcc-Mo. In the case of Ti-6242 and Ti-6246 alloys this does not occur. Mo only exists in solid solution in the $\alpha$ and $\beta$ phases of Ti. It is still possible to calculate the lowest energy phase of Mo by subtracting formation energies in the $\alpha$ and $\beta$ phases as in equation (6.1) because the term $\mu_{\mathrm{Mo}}$ cancels out in the subtraction. Those results are shown in section 6.4.

### 6.1.4 Mo-vacancy binding energy in $\alpha$-Ti

I have defined the binding energy of a Mo substitutional defect and a vacancy in $\alpha$-Ti as the total energy difference between a system in which the defects are infinitely far apart and a system in which they occupy neighbouring sites. When the defects are attracted to each other the binding energy is positive. In practice the binding energy was calculated as the total energy of both defects as far apart as possible in a $6 \times 6 \times 4$ supercell minus the total energy of the same supercell in which the vacancy occupies a site neighbouring the Mo atom. I used a $5 \times 5 \times 3$ MP **k**-point mesh for these calculations.

In $\alpha$-Ti a given site has six nearest neighbour sites in the same basal plane, which are not equivalent to the nearest neighbouring sites above and below this basal plane. Because of this there are two distinct nearest neighbour sites, and so there are two distinct

configurations for the Mo-vacancy pair: in the same basal plane, or in two adjacent basal planes. I calculated the binding energies for both configurations in $\alpha$-Ti.

## 6.2 Vacancy in $\alpha$-Ti

| | | Formation energy, eV |
|---|---|---|
| PBE | This work | 2.15 |
| | Scotti *et al.* [151] | 1.97 |
| | Medasani *et al.* [152] | 2.08 |
| | Shang *et al.* [153] | 2.09 |
| PBEsol | Medasani *et al.* [152] | 2.15 |
| | Shang *et al.* [13] | 2.14 |
| | Shang *et al.* [153] | 2.16 |
| PW91 | This work | 1.99 |
| | Medasani *et al.* [152] | 1.99 |
| | Raji *et al.* [154] | 1.97 |
| LDA | Medasani *et al.* [152] | 2.08 |
| | Shang *et al.* [153] | 2.07 |
| TB | Trinkle *et al.* [155] | 2.03 |
| Expt. | Estimate from [12, 13] | 2.74 |
| | Hashimoto *et al.* [156] | 1.27 |
| | (bcc) Shestopal *et al.* [157, 158] | 1.55 |

TABLE 6.3: Vacancy formation energies in Ti from DFT using different exchange-correlation functionals (PBE, PBEsol PW91 and LDA), tight-binding (TB), and experiment. All formation energies are shown in eV. The estimate calculated from the results of Köppers *et al.* [12] and Shang *et al.* [13] is discussed in section 6.2.

The vacancy formation energies I computed using the PBE and PW91 exchange-correlation (XC) functionals (shown in table 6.3) are within 10% of all other results shown in the table using these functionals. I included the PBEsol results of Medasani and Shang *et al.* [13, 152, 153] because the functional was optimised to give improved bond lengths in solids and surfaces compared with the PBE XC functional [159].

The DFT results in table 6.3 all agree on a vacancy formation energy of about 2 eV. For the case of a vacancy formation energy of 2.15 eV that I computed in this study, the equilibrium vacancy concentration at room temperature is $7.6 \times 10^{-37}$ vacancies

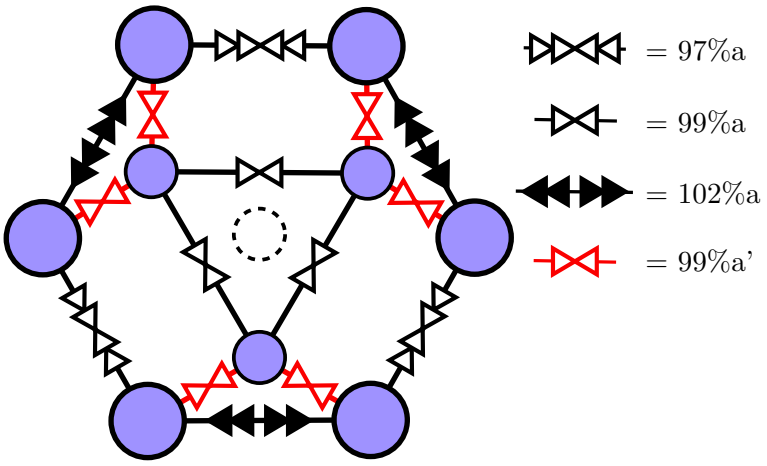



FIGURE 6.1: The distinct bonds between atoms neighbouring the vacancy in $\alpha$-Ti. Bond lengths are shown as percentages of the corresponding equilibrium bond lengths $a = 2.94$ Å in the basal plane and $a' = 2.88$ Å out of the basal plane. The vacancy occupies a site of $C_{3v}$ symmetry.

per atom in the system, essentially zero. Even at the elevated temperature of 200°C the equilibrium concentration is only $1.2 \times 10^{-23}$ vacancies per system atom, which is still completely negligible. This implies that there is a negligible number of intrinsic vacancies in macroscopic samples of $\alpha$-Ti in thermal equilibrium. Despite this result, it is well known [12, 160] that trace amounts of Fe, Co, and Ni substitutional impurities produce vacancies in $\alpha$-Ti by becoming interstitial defects that leave behind vacancies. By using the formation energies I have computed shown in table 6.4 I can test this mechanism for Mo. The energy required to form an interstitial Mo defect and a vacancy from a substitutional Mo defect is $2.17 - 0.57 + 2.15 = 3.75$ eV. This energy is so high that I can conclude that Mo is not an extrinsic vacancy source in $\alpha$-Ti.

As well as the formation energy I considered the changes in the lengths of bonds between nearest neighbour atoms of the vacancy. As shown in Fig. 6.1 the bond lengths vary by as much as 3% from the equilibrium bond lengths of 2.94 Å in the basal plane and by 1% of 2.88 Å out of the basal plane. These bond length changes maintain the local $C_{3v}$ point group symmetries of atomic sites in the hcp crystal.

The experimental values for the vacancy formation energy vary considerably when compared with the theoretical results, ranging from 1.27 eV [156] to 2.74 eV [12, 13]. In their study of self-diffusion in ultra-pure samples of $\alpha$-Ti, Köppers *et al.* [12] deduced a self-diffusion activation energy parallel to the basal plane of $3.14 \pm 0.02$ eV from measurements in the temperature range $600 - 860$°C. Assuming self-diffusion is mediated

by vacancies, and assuming the vacancy migration energy parallel to the basal plane is 0.40 eV, as computed by Shang *et al.* [13], I obtain a vacancy formation energy of 2.74 eV. This value is much higher than the DFT results in table 6.3.

The work of Glensk *et al.* [161] shows that in Cu the vacancy entropy of formation is linearly dependent on temperature, in contrast with the assumption usually used in the Arrhenius relation that the entropy is temperature-independent. This work implies that the enthalpy of formation at absolute zero is over-estimated when using the Arrhenius relation to extrapolate from data obtained at high temperatures, such as the data of Köppers *et al.* [12]. For a Cu vacancy it was shown [161] that the formation enthalpy at absolute zero is over-estimated by about 20%. If the enthalpy of formation of vacancies in $\alpha$-Ti follows a similar trend, then the corrected experimental enthalpy of formation will be much closer to the DFT results in table 6.3.

Hashimoto *et al.* [156] deduced the vacancy formation energy in $\alpha$-Ti from positron annihilation measurements. The authors used an empirical relation [162] obtained for fcc metals $E_v^f(\text{in eV}) = 1.46 \times 10^{-3}\, T_C$, where $E_v^f$ is the vacancy formation energy, and $T_C$ is the critical temperature at which the temperature dependence of the normalised peak positron count deviates from a linear relation because of thermal expansion [156]. In the experiment of Hashimoto *et al.* $T_C = 597°\text{C}$, so this is a high temperature measurement. It is not clear whether the empirical relation [162] holds for hcp metals as well, not least because there are two independent thermal expansion coefficients.

The energy of vacancy formation of Shestopal *et al.* [158] was obtained from measurements of the specific heat over a range of temperatures. A curve was then fitted to these data, and then a linear contribution not due to vacancy formation following a trend observed in other metals was subtracted. The measurement was made at temperatures above the $\alpha - \beta$ transition temperature of 882°C, and is thus a measurement of the vacancy formation energy in the $\beta$-phase.

## 6.3 Interstitial Mo in $\alpha$-Ti

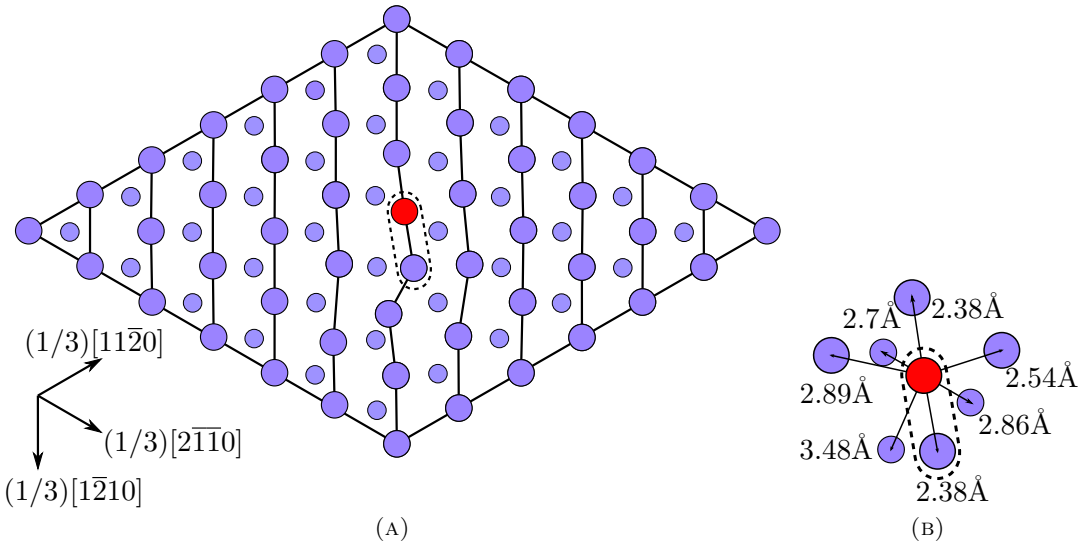
To find the minimum energy configuration of the Mo-interstitial I relaxed the Mo atom in six interstitial structures in the hcp lattice. I labelled the relaxed configurations using

the naming convention of Johnson and Beeler [163]. The six distinct metastable relaxed configurations of the Mo-interstitial are shown with their formation energies in table 6.4. I found three variants of the split dumbbell configuration in the basal plane (BS) that transform into each other via the three-fold rotational symmetry along the $c$-axis for every atomic site in $\alpha$-Ti. The BS-dumbbell is highlighted in Fig. 6.2(A), and has the lowest formation energy of the interstitial structures considered. As shown in Fig. 6.2(A) the most significant distortions are in the basal plane of the Mo interstitial. The bond lengths between the Mo atom and its nearest neighbours in the BS configuration are shown in Fig. 6.2(B). Other workers [11, 164, 165] have found the split dumbbell in the basal plane is metastable for self-interstitials in Ti, Zr, and Hf. Their formation energies are all within 0.2 eV of the lowest energy structures [11, 164, 165].

| Mo defect configuration | Formation energy, eV |
|---|---|
| Interstitial | |
| Octahedral | 2.32 |
| Basal octahedral | 2.67 |
| Basal split dumbell (BS) | 2.17 |
| BS 90° rotation | 2.23 |
| Split dumbell | 2.54 |
| Tetragonal | 3.37 |
| Substitutional | |
| $\alpha$-Ti | 0.57 |
| $\beta$-Ti | −0.71 |

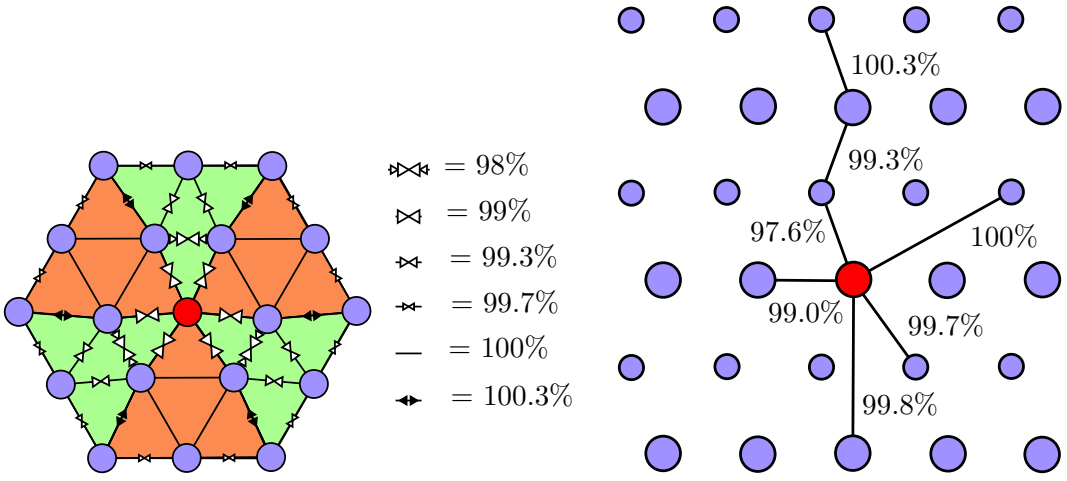
| Mo - Vac in $\alpha$-Ti | Binding energy, eV |
|---|---|
| Same basal | 0.22 |
| Adjacent basal | 0.23 |

TABLE 6.4: Relaxed formation energies of six Mo interstitial configurations in $\alpha$-Ti, and of Mo substitutional atoms in $\alpha$- and $\beta$-Ti. The last two rows show binding energies between a Mo substitutional atom and a vacancy in $\alpha$-Ti (Mo - Vac in $\alpha$-Ti) in the same basal plane and adjacent basal planes. (Positive binding energies correspond to defects that are attracted to each other).




(A) (B)

FIGURE 6.2: (A) The minimum energy dumbbell structure of the Mo interstitial in red with Ti atoms in blue. The structure is shown as a projection along the $c$-axis of two adjacent basal planes of the $6 \times 6 \times 4$ supercell. Circles of the same size denote atoms in the same basal plane. The dumbbell has been outlined. There are two equivalent structures related to this one by a three-fold rotational symmetry about the $c$-axis (normal to the page). The distortion due to the Mo atom is highlighted by black lines between atoms parallel to the [1$\bar{2}$10] perfect crystal direction. (B) A close-up of the Mo interstitial and the bond lengths between the defect and its nearest neighbours.




(A) (B)

FIGURE 6.3: (A) The Mo substitutional atom (red circle) in $\alpha$-Ti (blue circles) showing bond lengths in the basal plane, shown as a percentage of the ideal bond length in the basal plane of $\alpha$-Ti. The relaxed defect configuration is located in a site of $C_{3v}$ symmetry, highlighted by green and brown shading, the same as a Ti atoms in $\alpha$-Ti. (B) Projection of the Mo substitutional along [1$\bar{1}$00] with bond lengths shown as a percentage of ideal bond lengths in pure $\alpha$-Ti. The smaller circles are on adjacent planes along [1$\bar{1}$00].

## 6.4 Substitutional Mo in $\alpha$- and $\beta$-Ti

I found the formation energy of the relaxed Mo substitutional atom in $\alpha$-Ti to be +0.57 eV. The structure of the relaxed defect is shown in Fig. 6.3. I compared my Mo substitutional results with those of Huang *et al.* [149] by using a free, non-spin polarised atom as the reference state of the Mo chemical potential. The inclusion of spin polarisation does not have a significant effect on the bulk energy in bcc-Mo, but it does have a significant effect on the isolated Mo atom, as the results of Huang *et al.* show [149]. With this chemical potential I calculated a formation energy of −9.83 eV in good agreement with the value of −9.88 eV obtained by Huang *et al.* [166].

Huang *et al.* [149] used the isolated transition metal atoms as the reference state to calculate formation energies of substitutional transition metal defects in Ti. The authors did this to remove the influence of the varying interatomic bonding of the transition metals in their bulk phase on the formation energies [149]. However, because these energies are very large in magnitude the crystalline state of Mo appears to be a more appropriate choice for the chemical potential reference state when computing formation energies that are likely to occur physically.

To better understand why Mo is more soluble in the $\beta$-phase than the $\alpha$-phase I simulated a relaxed Mo substitutional defect in a supercell composed of $6 \times 6 \times 6$ conventional unit cells of $\beta$-Ti. From these simulations I calculated a formation energy of −0.71 eV. Hence the process of forming Mo substitutional defects in the $\alpha$-phase is endothermic, whereas it is exothermic in the $\beta$-phase. This implies that in thermal equilibrium Mo is much more stable in the $\beta$-phase of Ti than the $\alpha$-phase, and so a much higher concentration of Mo would be expected in the $\beta$-phase relative to the $\alpha$-phase in Ti-alloys containing both phases.

## 6.5 Binding energy between a Mo substitutional atom and a vacancy in $\alpha$-Ti

I found that the Mo substitutional atom and the vacancy bind with an energy of 0.22 eV for both defects in the same basal plane, and 0.23 eV for defects in adjacent planes. My results are in fairly good agreement with those of Xu *et al.* [167], with good agreement for

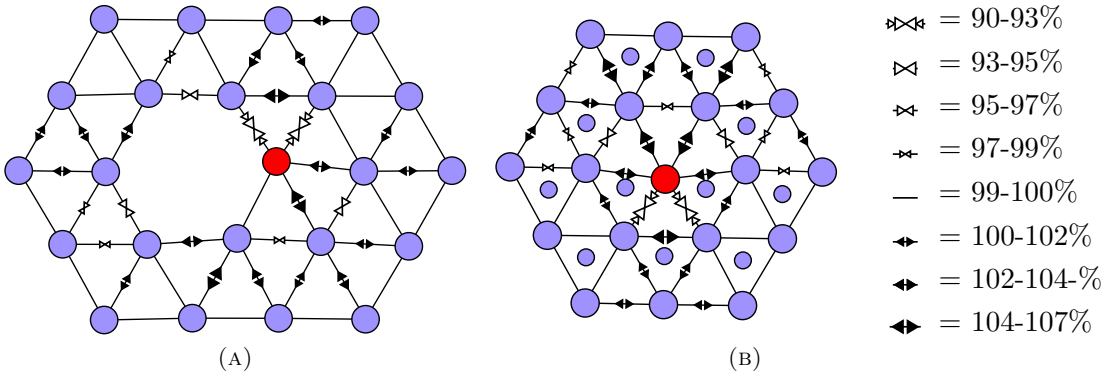



FIGURE 6.4: (A) Neighbouring Mo substitutional atom (red) and vacancy defects in the same basal plane of $\alpha$-Ti. (B) Neighbouring Mo substitutional atom (red) and vacancy defects in adjacent basal planes. The Mo atom lies in the basal plane containing atoms represented by larger circles, and the vacancy in the basal plane containing atoms represented by smaller circles. All bond lengths are shown as percentages of the ideal lattice parameter $a = 2.94$ Å.

the binding energy of defects in the same basal plane, and a deviation of 0.1 eV between our binding energies for defects on adjacent basal planes. The significant difference in the latter case could be because of the smaller supercell of $4 \times 4 \times 2$ primitive hcp unit cells used by Xu *et al.* [167]. The deviations in bond length near the Mo-vacancy complex are large, with differences in between -10% and +7% from the ideal bond length in the basal plane. Because the supercell size parallel to the **c** lattice vector that was used by Xu *et al.* [167] is half the value used in this study, distortions such as those shown in Fig. 6.4 may not be allowed.

Despite the binding energy between a Mo atom and a vacancy being positive it is not enough to bind the defect pair for a significant length of time. For a typical vibrational frequency of $10^{12}$ Hz it would take about 10 ns for the defects to unbind. Even at room temperature the vacancy would almost instantly break away from the Mo atom. Thus even if there were enough vacancies present to allow creep to occur via vacancy mediated mass transport, the effect of additional Mo in $\alpha$-Ti regions of Ti-6246 in suppressing creep would be negligible. This result indicates that the relatively lower CDF susceptibility of Ti-6246 compared with Ti-6242 is not due to suppression of mass transport, and hence load transfer to hard grains during CDF loading. This result also implies that the intrinsic creep properties of $\alpha$-grains in Ti-6242 and Ti-6246 should not differ. In this instance, 'intrinsic' means excluding differences due to microstructural features like differing grain sizes and relative grain orientations.

## 6.6 The effect of Mo in Ti-6242 and Ti-6246

Based on the results in the previous section it is more likely that the CDF susceptibility difference is due to the influence of Mo on the microstructure and microtexture of the alloys as observed by Qiu *et al.* [26]. The authors observed that the microstructural effect of the extra Mo in Ti-6246 compared with Ti-6242 was to decrease the phase fraction of the $\alpha$ phase, as well as the average $\alpha$ grain size from roughly 13.6 $\mu$m in Ti-6242 to roughly 5.3 $\mu$m in Ti-6246. Qiu *et al.* attributed this to Mo being a slow diffuser in $\alpha$-Ti [26], [14, pp. 45-46].

Qiu *et al.* prepared their alloys by thermo-mechanically processing the ingots of Ti-624X (X=2,3,4,5,6 wt. % Mo) above the $\alpha$-$\beta$ phase transition temperature, reducing the ingot diameters by ~30%. Qiu *et al.* then deformed the alloys below the $\alpha$-$\beta$ phase transition temperature in the $\alpha + \beta$ phase field, reducing the ingot diameters further by ~70%. In this second processing stage the $\alpha$-phase began to nucleate. The growth rate of the $\alpha$-phase is partially determined by the diffusion rate of Mo atoms out of the $\alpha$-phase to the $\beta$-phase [26]. Hence the slow diffusion rate of Mo limits the growth rate of the $\alpha$-phase, resulting in a smaller $\alpha$ grain size being formed in Ti-624X alloys containing a higher wt. % of Mo. Since most of the plastic strain is accommodated in the $\alpha$ grains as shown by Qiu *et al.* [26], smaller $\alpha$ grains result in a shorter effective slip length for dislocations, which can result in a smaller accumulated strain whilst deformation occurs.

Another effect of a smaller average $\alpha$ grain size is that it decreases the average slip band spacing within the $\alpha$ grains [26]. This is shown in the experimental results of Qiu *et al.* [26] where the slip band spacing decreases in the $\alpha$-grains going from Ti-6242 to Ti-6246. A smaller slip band spacing results in a more homogenous distribution of dislocations, reducing the likelihood of high stress concentrations occurring at phase or grain boundaries. This reduces the effects of load shedding, which is hypothesised to play a key role in CDF failure [23].

The microtextural effect Mo has in Ti-6246 compared with Ti-6242 described by Qiu *et al.* [26] is that it forms a more random orientation distribution of $\alpha$ grains. Qiu *et al.* assert that Mo does this as a strong $\beta$ stabiliser by lowering the $\alpha$-$\beta$ transition temperature, which encourages formation of multiple differing $\alpha$-grain orientations [14, pp. 32-33]. Qiu *et al.* [26] observed this tendency in their Ti-6242 and Ti-6246 samples,

such that the Ti-6242 sample had $\alpha$ grains that were clustered together into colonies of similar orientation, whereas the Ti-6246 contained thin $\alpha$ grains with a more random orientation distribution.

## 6.7 CDF temperature dependence

The previous section shows that Mo atoms binding to vacancies does not explain the difference in CDF susceptibility between Ti-6242 and Ti-6246. My results show that the binding energy between a Mo substitutional atom and a vacancy in $\alpha$-Ti is only 0.23 eV. This energy barrier could be overcome by a vacancy in 10 ns via thermal excitations at room temperature, allowing a vacancy to almost instantaneously escape from a Mo atom. Hence our results are in agreement with those of Qiu *et al.* [26] suggesting that the role of Mo in affecting CDF susceptibility is primarily microstructural and microtextural. However, their observations do not explain the vanishing CDF susceptibility in Ti-6242 for temperatures exceeding roughly 200°C [14].

In a recent article by Ready, Haynes, Grabowski, Rugg, and Sutton (RHGRS) [4], Sutton suggests that the temperature dependence of CDF is caused by the large reduction of the critical resolved shear stress of $\langle \mathbf{c} + \mathbf{a} \rangle$ slip for temperatures in the range 0°C and 300°C observed [14] for single crystals of Ti-6.6Al. Sutton suggests that the reduction allows enough plastic deformation to occur in hard grains via $\langle \mathbf{c} + \mathbf{a} \rangle$ slip to prevent large loads forming at grain boundaries. Once the research was completed RHGRS [4] became aware that a similar explanation was suggested recently by Somnath Ghosh and coworkers [35, 168].

When the intrinsic lattice resistance impeding $\langle \mathbf{c} + \mathbf{a} \rangle$ dislocation motion is large then the dislocations are likely to move via the nucleation and migration of double kinks, which are both thermally activated processes. Consider a length $L$ of the dislocation with a crystal period parallel to the $\langle \mathbf{c} + \mathbf{a} \rangle$ dislocation line $p$. For the kink height of $h$ the number of sites where a double kink could be nucleated along this dislocation line is $L/p$. The fraction of these sites where nucleation of a double kink does occur is:

$$\exp\left(\frac{-\Delta G_f + \tau b h l_c}{k_B T}\right), \tag{6.2}$$

where $\Delta G_f$ is the free energy of formation of a double kink, $\tau$ is the resolved shear stress on the pyramidal plane along the $\langle \mathbf{c}+\mathbf{a} \rangle$ direction, $b$ is the magnitude of $\mathbf{c}+\mathbf{a}$, $l_c$ is the critical separation of the double kink beyond which it separates into two kinks, $k_B$ is Boltzmann's constant, and $T$ is the temperature. Using the definition in (6.2), the number of kinks on the dislocation is:

$$2\frac{L}{p}\exp\left(\frac{-\Delta G_f}{k_B T}\right)\exp\left(\frac{\tau b h l_c}{k_B T}\right). \tag{6.3}$$

Let $v_d$ be the velocity of the dislocation, and $v_k$ be the velocity of a kink. If $t_l$ is the time needed for a kink to travel the distance $L$, then $t_l = L/v_k$. When the kink travels the length $L$ the dislocation advances a distance equal to the kink height $h$. Therefore:

$$v_d = \frac{h}{t_l} = \frac{h}{L}v_k. \tag{6.4}$$

The kink velocity shown in (6.4) can be defined as follows:

$$\begin{aligned} v_k &= p\nu\exp\left(\frac{-\Delta G_m}{k_B T}\right)\left[\exp\left(\frac{\tau b h p}{k_B T}\right) - \exp\left(\frac{-\tau b h p}{k_B T}\right)\right], \\ &= 2p\nu\exp\left(\frac{-\Delta G_m}{k_B T}\right)\sinh\left(\frac{|\tau| b h p}{k_B T}\right), \end{aligned} \tag{6.5}$$

where $\Delta G_m$ is the free energy of migration of the kink, $\nu$ is the attempt frequency. The two exponential terms inside the square brackets of the first equation in (6.5) correspond to kinks migrating forwards and backwards along the dislocation line. Substituting the expression for the kink velocity in (6.5) into (6.4), and multiplying by the number of kinks given by (6.3) results in:

$$v_d = 4h\nu\exp\left(-\frac{\Delta G}{k_B T}\right)\sinh\left(\frac{|\tau| b h p}{k_B T}\right)\exp\left(\frac{|\tau| b h l_c}{k_B T}\right), \tag{6.6}$$

where $\Delta G = \Delta G_f + \Delta G_m$. The dislocation velocity $v_d$ can then be related to a strain rate contribution $\dot{\gamma}$ using Orowan's equation, $\dot{\gamma} = \rho_M b v_d$, where $\rho_M$ is the density of mobile $\langle \mathbf{c}+\mathbf{a} \rangle$ dislocations. Testing this suggestion would require reliable calculations of the energy of formation of double kinks and the single kink migration energy for $\langle \mathbf{c}+\mathbf{a} \rangle$ dislocations. This would be a major undertaking using DFT.

Sutton estimated $\Delta G$ in [4] by first assuming a Debye temperature of 147°C [38]. This implies that at room temperature the attempt frequency is lower than $\nu_D$ the Debye

frequency, but for temperatures greater than 200°C the attempt frequency may be set equal to $\nu_D = 8.75 \times 10^{12}$ s$^{-1}$. For a screw $\mathbf{c}+\mathbf{a}$ dislocation such that $b = p = 5.51$ Å, the kink height, $h$, is the spacing between Peierls valleys parallel to $\mathbf{c}+\mathbf{a}$, which is roughly equal to the lattice constant $a = 2.94$ Å. For $T = 200$°C the argument of sinh in (6.6) is $|\tau|bhp/(k_BT) = 8.20$, assuming a value of $|\tau| = 600$ MPa from the experimental measurements of [14, p. 21]. Using these values $\sinh(|\tau|bhp/(k_BT))$ can be well approximated using $\frac{1}{2}\exp(|\tau|bhp/(k_BT))$. Assuming $l_c \approx p$ equation (6.6) becomes:

$$v_d = 2h\nu \exp\left(-\frac{\Delta G}{k_BT}\right) \exp\left(\frac{2|\tau|bhp}{k_BT}\right) \tag{6.7}$$

Using the values in the above paragraph $\exp\left((2|\tau|bhp)/(k_BT)\right) = 1.32 \times 10^7$. For a typical strain rate of $10^{-4}$ s$^{-1}$ and a mobile $\langle \mathbf{c}+\mathbf{a} \rangle$ dislocation density of roughly $10^{10}$ m$^{-2}$, Orowan's equation requires an average dislocation velocity of about $1.81 \times 10^{-5}$ ms$^{-1}$. When these values are substituted into equation (6.7) they give a value of $\Delta G \approx 1.46$ eV. As a check this estimated value of $\Delta G$ can be used to calculate the critical resolved shear stress for slip of screw $\langle \mathbf{c}+\mathbf{a} \rangle$ dislocations at 27°C needed to produce a strain rate of $10^{-4}$ s$^{-1}$. The value obtained is 860 MPa, which agrees fairly well with the experimental measurement of [14, p. 21] of $\approx 800$ MPa, given the uncertainties in the mobile $\langle \mathbf{c}+\mathbf{a} \rangle$ dislocation density, the strain rate assumed, and in $l_c$. The combination of equation (6.7) and the Orowan equation gives the following relation between the critical resolved shear stress and the strain rate:

$$\tau = \frac{1}{\Omega}\left[\Delta G + k_BT \ln\left(\frac{\dot{\gamma}p}{\nu\Omega\rho_M}\right)\right], \tag{6.8}$$

where $\Omega = 2bhp$ is the activation volume for forming a double kink and moving a single kink.

# Chapter 7

# Conclusions and Outlook

The primary motivation for this project was to better understand the fatigue failure mechanism called cold dwell fatigue (CDF). The observation that the Ti-alloys Ti-6242 and Ti-6246 have very different CDF susceptibilities led to a hypothesis about the role the extra Mo plays in Ti-6246 to reduce its CDF susceptibility. The hypothesis is that Mo traps vacancies in the hexagonal close-packed $\alpha$ phase of these alloys thus reducing creep relaxation and preventing large stress concentrations known to cause CDF failure [23].

Testing this hypothesis required simulating large supercells of Ti atoms containing point defects using density functional theory (DFT). In preparation for these calculations I parameterised the DFT model by carrying out convergence tests on bulk Ti. As well as these tests I studied the bonding of hexagonal close-packed Ti by comparing its charge density on the basal plane with that of face-centred cubic Al on the (111) plane using DFT. This study showed that while Ti appears to have more bond directionality in its basal charge density compared with the (111) charge density of Al, it can be argued that the charge density variations are not large enough to provide evidence of directional bonding.

Because of the significant interest in the slip deformation of Ti-alloys and as a learning exercise for carrying out large-scale DFT calculations I computed the $\gamma$-surface for the pyramidal I plane in $\alpha$-Ti using DFT. I used two different pseudopotentials to compute this surface, one denoted by 4elPP with four valence states and one denoted by 12elPP with 12 valence states. My results show that the 4elPP provides a good approximation

of the 12elPP for describing physically relevant stacking faults in the pyramidal I plane of $\alpha$-Ti.

From the features of the pyramidal I $\gamma$ surface I identified two stable stacking faults, $I_1$ with an energy of 163 mJ/m$^2$, and $I_2$ with an energy of 681 mJ/m$^2$. The high value of the $I_2$ stacking fault energy implies that $\mathbf{c}+\mathbf{a}$ dissociation on the pyramidal I plane into three partial dislocations described in chapter 5 is unfavourable. The surface also rules out dissociation of $\mathbf{c}+\mathbf{a}$ dislocations into two $(\mathbf{c}+\mathbf{a})/2$ partial dislocations because there is no stable minimum at $(\mathbf{c}+\mathbf{a})/2$ on the surface.

Using the basal and pyramidal I $\gamma$-surfaces computed using DFT I tested three new interatomic potentials (IPs) for Ti for simulating plasticity developed by Mendelev *et al.* [49]. I tested these new IPs by computing $\gamma$-surfaces and stable SFEs, and then compared them to the corresponding DFT results. These IPs are much less computationally expensive, and so they if they are accurate enough compared with DFT they could be used to efficiently simulate plastic deformation in $\alpha$-Ti. I found that the new IPs show better agreement with DFT than the potential developed by Ackland [9]. However all of the IPs have $\gamma$-surface energies and gradients that differ significantly from those of DFT. Hence further tests need to be carried out to assess the impact of these differences.

Using the experience I gained from running the $\gamma$-surface calculations I tested the hypothesis about the role of Mo in affecting CDF susceptibility. I did this by computing the binding energy between a Mo substitutional defect and vacancy in $\alpha$-Ti. I found that the binding energy was positive, but too small to keep the defect pair bound when thermal fluctuations are present. Hence I found that Mo does not influence creep deformation by trapping vacancies.

Based on these findings I now think that the effect Mo has on the CDF susceptibility is largely microstructural as shown by the experimental studies of Qiu *et al.* [26]. The authors show that Mo reduces the CDF susceptibility in Ti-6246 relative to that of Ti-6242 by causing a more random orientation distribution of smaller $\alpha$-grains to form in Ti-6246. These conditions serve to lessen the probability of large stress concentrations building up at hard grains in the $\alpha$-phase, and so reduce the likelihood of CDF failure.

One possible explanation for the temperature dependence was proposed by Somnath Ghosh and coworkers [35, 168] and was derived later and independently by Sutton in

the work of Ready *et al.* [4]. The suggestion is that the temperature dependence is due to the strong temperature dependence of $\langle \mathbf{c} + \mathbf{a} \rangle$ slip, with the $\langle \mathbf{c} + \mathbf{a} \rangle$ slip being activated by the nucleation of double kinks and the migration of the individual kinks. The proposed model agrees with the experimental data of Paton *et al.* [169] [14, p. 21].

To test the suggestion of Ghosh *et al.* [35, 168] and Sutton [4] reliable calculations of the formation energy of double kinks and the migration energy of single kinks would have to be carried out. Carrying out these calculations using DFT would be a major undertaking.

The directional bonding study could be continued by using more quantitative measures of directional bonding. One such measure involves taking the charge density and projecting it into spherical harmonics, or lattice harmonics consisting of linear combinations of spherical harmonics that transform under the symmetry group of the hexagonal close-packed crystal [170–172]. If the projections for orders $l \neq 0$ are comparable to the $l = 0$ projection then this would indicate significant angular variation or bond directionality.

Our work testing the new IPs of Mendelev *et al.* [49] has not fully assessed their capability of accurately simulating plastic deformation in $\alpha$-Ti. One way of further assessing these IPs would be to carry out the tests presented in section 5.3 for the prism $\gamma$-surface computed using the new IPs and DFT. Because prism slip is the dominant slip mode in $\alpha$-Ti this test would provide a useful test of these new IPs for describing slip in $\alpha$-Ti. The entire prism $\gamma$-surface has already been computed before using DFT [127, 140, 143, 173].

# Bibliography


[1] A. J. Ready, A. P. Sutton, P. D. Haynes, and D. Rugg. Point, Linear and Planar Defects in Titanium. In *Proc. 13th World Conf. Titan.*, pages 1029–1034. John Wiley and Sons, Inc., 2016. doi:10.1002/9781119296126.ch175.

[2] A. J. Ready, P. D. Haynes, D. Rugg, and A. P. Sutton. Stacking faults and the $\gamma$-surface on first-order pyramidal planes in $\alpha$-titanium. *Philos. Mag.*, 97(14): 1129–1143, 2017. ISSN 1478-6435. doi:10.1080/14786435.2017.1292059.

[3] A. J. Ready, P. D. Haynes, and A. P. Sutton. Comment on Development of an interatomic potential for the simulation of defects, plasticity, and phase transformations in titanium [J. Chem. Phys. 145, 154102 (2016)]. *J. Chem. Phys.*, 147(1): 017101, 2017. ISSN 0021-9606. doi:10.1063/1.4990736.

[4] A. J. Ready, P. D. Haynes, B. Grabowski, D. Rugg, and A. P. Sutton. The role of molybdenum in suppressing cold dwell fatigue in titanium alloys. *Proc. R. Soc. A*, 473(2203), 2017. doi:10.1098/rspa.2017.0189.

[5] J. Updike. *Midpoint and Other Poems*. Harper Collins Distribution Services, 1969. ISBN 0233961526.

[6] M. R. Bache. A review of dwell sensitive fatigue in titanium alloys : the role of microstructure , texture and operating conditions. *Int. J. Fatigue*, 25:1079–1087, 2003. doi:10.1016/S0142-1123(03)00145-2.

[7] M. R. Bache, M. Cope, H. M. Davies, W. J. Evans, and G. Harrison. Dwell sensitive fatigue in a near alpha titanium alloy at ambient temperature. *Int. J. Fatigue*, 19(1):83–88, 1998. doi:10.1016/S0142-1123(97)00020-0.

[8] S. J. Clark, M. D. Segall, C. J. Pickard, P. J. Hasnip, M. I. J. Probert, K. Refson, and M. C. Payne. First principles methods using CASTEP. *Z. Krist.*, 220:567–570, 2005. ISSN 0044-2968. doi:10.1524/zkri.220.5.567.65075.

[9] G. J. Ackland. Theoretical study of titanium surfaces and defects with a new many-body potential. *Philos. Mag. A*, 66(6):917–932, 1992. ISSN 0141-8610. doi:10.1080/01418619208247999.

[10] M. I. Mendelev. LAMMPS implementation of the Ackland potential (accessed on 2015-02-16), 2009. URL `http://www.ctcms.nist.gov/potentials/Ti.html`.

[11] G. Vérité, C. Domain, C. C. Fu, P. Gasca, A. Legris, and F. Willaime. Self-interstitial defects in hexagonal close packed metals revisited: Evidence for low-symmetry configurations in Ti, Zr, and Hf. *Phys. Rev. B*, 87(13):1–6, 2013. ISSN 10980121. doi:10.1103/PhysRevB.87.134108.

[12] M. Köppers, C. Herzig, M. Friesel, and Y. Mishin. Intrinsic self-diffusion and substitutional Al diffusion in $\alpha$-Ti. *Acta Mater.*, 45(10):4181–4191, 1997. ISSN 13596454. doi:10.1016/S1359-6454(97)00078-5.

[13] S. L. Shang, L. G. Hector Jr., Y. Wang, and Z. K. Liu. Anomalous energy pathway of vacancy migration and self-diffusion in hcp Ti. *Phys. Rev. B*, 83(22):224104, 2011. ISSN 10980121. doi:10.1103/PhysRevB.83.224104.

[14] G. Lutjering and J. C. Williams. *Titanium*. Springer, Berlin Heidelberg New York, second edition, 2007. ISBN 978-3-540-71397-5.

[15] R. L. Fleischer (author) and D. Peckner (editor). *The strengthening of metals: Solid-Solution Hardening*. Reinhold Publishing Corporation, New York, 1967. ISBN 0278915248.

[16] R. R. Boyer. An overview on the use of titanium in the aerospace industry. *Mater. Sci. Eng. A*, 213(1-2):103–114, 1996. ISSN 09215093. doi:10.1016/0921-5093(96)10233-1.

[17] P. Ruffles. The RB 211: the first 25 years, 1992. URL `http://dspace.rri.res.in/handle/2289/5433`.

[18] P. Ruffles. Aerospace structural materials: present and future. *Mater. World*, 3 (10), 1995.

[19] National Transportation Safety Board. NTSB Identification: LAX94IA018. Technical report, National Transportation Safety Board, 1993. URL https://www.ntsb.gov/_layouts/ntsb.aviation/brief2.aspx?ev_id=20001211X13583&ntsbno=LAX94IA018&akey=1.

[20] D. R. Hinson. NTSB Safety Recommendation, A-95-84 and -85. Technical Report March 1992, National Transportation Safety Board, 1995. URL https://www.ntsb.gov/safety/safety-recs/recletters/A95_84_85.pdf.

[21] Centro de Investigação e Prevenção de Acidentes Aeronáuticos. Accident Report, Aircraft PN-VNN, Boeing 767-0200ER,. Technical report, CENIPA, 2000. URL http://aviation-safety.net/database/record.php?id=20000607-1&lang=en.

[22] J. F. Garvey. NTSB Safety Recommendation, A-00-104. Technical report, National Transportation Safety Board, 2000. URL https://www.ntsb.gov/_layouts/ntsb.recsearch/Recommendation.aspx?Rec=A-00-104.

[23] T. B. Britton, F. P. E. Dunne, and A. J. Wilkinson. On the mechanistic basis of deformation at the microscale in hexagonal close-packed metals. *Proc. R. Soc. A Math. Phys. Eng. Sci.*, 471(2178):20140881–20140881, 2015. ISSN 1364-5021. doi:10.1098/rspa.2014.0881.

[24] M. R. Bache and W. J. Evans. Dwell Sensitive Fatigue Response of Titanium Alloys for Power Plant Applications. *J. Eng. Gas Turbines Power*, 125(1):241, 2003. ISSN 07424795. doi:10.1115/1.1494094.

[25] Z. Zhang, M. A. Cuddihy, and F. P. E. Dunne. On rate-dependent polycrystal deformation: the temperature sensitivity of cold dwell fatigue. *Proc. R. Soc. A*, 471(2181):20150214, 2015. ISSN 1364-5021. doi:10.1098/rspa.2015.0214.

[26] J. Qiu, Y. Ma, J. Lei, Y. Liu, and A. Huang. A Comparative Study on Dwell Fatigue of Ti-6Al-2Sn-4Zr-xMo (x=2 to 6) Alloys on a Microstructure-Normalized Basis. *Metall. Mater. Trans. A Phys. Metall. Mater. Sci.*, 45(13):6075–6087, 2014. ISSN 10735623. doi:10.1007/s11661-014-2541-5.

[27] B. C. Odegard and A. W. Thompson. Low temperature creep of Ti-6 Al-4 V. *Metall. Trans.*, 5(5):1207–1213, 1974. ISSN 1543-1916. doi:10.1007/BF02644335.

[28] T. Neeraj, D-H. Hou, G. S. Daehn, and M. J. Mills. Phenomenological and microstructural analysis of room temperature creep in titanium alloys. *Acta Mater.*, 48(6):1225–1238, 2000. ISSN 13596454. doi:10.1016/S1359-6454(99)00426-7.

[29] S. Suri, T. Neeraj, G. S. Daehn, D-H. Hou, J. M. Scott, R. W. Hayes, and M. J. Mills. Mechanisms of primary creep in alpha/beta titanium temperatures alloys at lower temperatures. *Mater. Sci. Eng. A*, 236:996–999, 1997. doi:10.1016/S0921-5093(97)00322-5.

[30] V. Hasija, S. Ghosh, M. J. Mills, and D. S. Joseph. Deformation and creep modeling in polycrystalline Ti-6Al alloys. *Acta Mater.*, 51:4533–4549, 2003. doi:10.1016/S1359-6454(03)00289-1.

[31] T. Neeraj and M. J. Mills. Short-range order ( SRO ) and its effect on the primary creep behavior of a Ti 6wt. % Al alloy. *Mater. Sci. Eng. A*, 321:415–419, 2001. doi:10.1016/S0921-5093(01)01045-0.

[32] W. J. Evans and M. R. Bache. Dwell-sensitive fatigue under biaxial loads in the near-alpha titanium alloy IMI685. *Fatigue*, 16:443–452, 1994. doi:10.1016/0142-1123(94)90194-5.

[33] A. N. Stroh. The Formation of Cracks as a Result of Plastic Flow. *Proc. R. Soc. A Math. Phys. Eng. Sci.*, 223(1154):404–414, 1954. ISSN 1364-5021. doi:10.1098/rspa.1954.0124.

[34] A. N. Stroh. Dislocations and Cracks in Anisotropic Elasticity. *Philos. Mag.*, 3 (30):625–646, 1958. ISSN 0031-8086. doi:10.1080/14786435808565804.

[35] D. Ozturk, A. Shahba, and S. Ghosh. Crystal plasticity FE study of the effect of thermo-mechanical loading on fatigue crack nucleation in titanium alloys. *Fatigue Fract. Eng. Mater. Struct.*, 39(6):752–769, 2016. ISSN 14602695. doi:10.1111/ffe.12410.

[36] Larry Kaufman. The lattice stability of metals-I. Titanium and zirconium. *Acta Metall.*, 7(8):575–587, 1959. ISSN 00016160. doi:10.1016/0001-6160(59)90195-6.

[37] E. W. Collings and J. C. Ho. Magnetic susceptibility and low-temperature specific heat of high-purity titanium. *Phys. Rev. B*, 2(2):235–244, 1970. ISSN 01631829. doi:10.1103/PhysRevB.2.235.

[38] C. Kittel. *Introduction to Solid State Physics, 8th edn.* John Wiley and Sons, Hoboken NJ, 2005. ISBN 9780471415268.

[39] J. C. Williams, R. G. Baggerly, and N. E. Paton. Deformation behavior of hcp Ti-Al alloy single crystals. *Metall. Mater. Trans. a-Physical Metall. Mater. Sci.*, 33(3):837–850, 2002. ISSN 1073-5623. doi:10.1007/s11661-002-1016-2.

[40] D. Deka, D. S. Joseph, S. Ghosh, and M. J. Mills. Crystal plasticity modeling of deformation and creep in polycrystalline Ti-6242. *Metall. Mater. Trans. A*, 37(5): 1371–1388, 2006. ISSN 1073-5623. doi:10.1007/s11661-006-0082-2.

[41] H. Conrad. Effect of Interstitial Solutes on the Strength and Ductility of Titanium. *Prog. Mater. Sci.*, 26:123–403, 1981. doi:10.1016/0079-6425(81)90001-3.

[42] Y. Mishin and C. Herzig. Overview No. 136: Diffusion in the Ti-Al System. *Acta Mater.*, 48(136):589–623, 2000. doi:10.1016/S1359-6454(99)00400-0.

[43] C. Herzig, R. Willecke, and K. Vieregge. Self-diffusion and fast cobalt impurity diffusion in the bulk and in grain boundaries of hexagonal titanium. *Philos. Mag.*, 63(5):949–958, 1991. ISSN 0141-8610. doi:10.1080/01418619108213927.

[44] V. Sinha, M. J. Mills, J. C. Williams, and J. E. Spowart. Observations on the faceted initiation site in the dwell-fatigue tested Ti-6242 alloy: Crystallographic orientation and size effects. *Metall. Mater. Trans. A*, 37(5):1507–1518, 2006. ISSN 1073-5623. doi:10.1007/s11661-006-0095-x.

[45] P. J. Hasnip, K. Refson, M. I. J. Probert, J. R. Yates, S. J. Clark, and C. J. Pickard. Density functional theory in the solid state. *Philos. Trans. R. Soc. A*, 372(2011):20130270, 2014. doi:10.1098/rsta.2013.0270.

[46] B. E. Tegner and G. J. Ackland. Pseudopotential errors in titanium. *Comput. Mater. Sci.*, 52(1):2–6, 2012. ISSN 09270256. doi:10.1016/j.commatsci.2010.12.033.

[47] D. Sholl and J. A. Steckel. *Density functional theory: a practical introduction.* John Wiley and Sons, 2011. ISBN 978-0-470-37317-0.

[48] M. W. Finnis and J. E. Sinclair. A simple empirical N-body potential for transition metals. *Philos. Mag. A*, 50(1):45–55, 1984. ISSN 01418610. doi:10.1080/01418618408244210.

[49] M. I. Mendelev, T. L. Underwood, and G. J. Ackland. Development of an interatomic potential for the simulation of phase transformations in titanium. *J. Chem. Phys.*, 145(15):154102, 2016. doi:10.1063/1.4964654.

[50] R. P. Feynman, R. B. Leighton, and M. Sands. *The Feynman Lectures on Physics*. Basic Books, New York, new millen edition, 2011.

[51] C. D. Chaffee. *Building the global fiber optics superhighway*. Springer Science and Business Media, 2001.

[52] D. A. Park. *Introduction to the Quantum Theory*. McGraw-Hill, second edition, 1974. ISBN 0-07-048481-3.

[53] J. M. Zhang and M. Kollar. Optimal multiconfiguration approximation of an N-fermion wave function. *Phys. Rev. A*, 89(1):012504, 2014. ISSN 1050-2947. doi:10.1103/PhysRevA.89.012504.

[54] R. Van Noorden, B. Maher, and R. Nuzzo. The top 100 papers. *Nature*, 514(7524): 550–553, 2014. ISSN 0028-0836. doi:10.1038/514550a.

[55] J. M. Ziman. *Principles of the Theory of Solids*. Cambridge University Press, 2nd edition, 1972. ISBN 9781139644075. doi:10.1017/CBO9781139644075.

[56] P. Hohenberg and W. Kohn. Inhomogeneous electron gas. *Phys. Rev. B*, 136(3B): 864–871, 1964. ISSN 01631829. doi:10.1103/PhysRevB.7.1912.

[57] W. Kohn and L. J. Sham. Self-Consistent equations including exchange and correlation effects. *Phys. Rev.*, 140(4A):1133–1138, 1965. doi:10.1103/PhysRev.140.A1133.

[58] M. Ernzerhof and G. E. Scuseria. Assessment of the Perdew–Burke–Ernzerhof exchange-correlation functional. *J. Chem. Phys.*, 110(1999):5029, 1999. ISSN 00219606. doi:10.1063/1.478401.

[59] W. M. C. Foulkes, L. Mitas, R. J. Needs, and G. Rajagopal. Quantum Monte Carlo simulations of solids. *Rev. Mod. Phys.*, 73(1):33–83, 2001. doi:10.1103/RevModPhys.73.33.

[60] G. H. Booth, A. Grüneis, G. Kresse, and A. Alavi. Towards an exact description of electronic wavefunctions in real solids. *Nature*, 493(7432):365–70, 2013. ISSN 1476-4687. doi:10.1038/nature11770.

[61] C. Muller and B. Paulus. Wavefunction-based electron correlation methods for solids. *Phys. Chem. Chem. Phys.*, 14(21):7605–7614, 2012. doi:10.1039/c2cp24020c.

[62] D. M. Ceperley and B. J. Alder. Ground state of the electron gas by a stochastic method. *Phys. Rev. Lett.*, 45(7):566–569, aug 1980. doi:10.1103/PhysRevLett.45.566.

[63] T. Schmidt and S. Kümmel. The influence of one-electron self-interaction on d-electrons. *Computation*, 4:33, 2016. ISSN 2079-3197. doi:10.3390/computation4030033.

[64] C. J. Cramer and D. G. Truhlar. Density functional theory for transition metals and transition metal chemistry. *Phys. Chem. Chem. Phys.*, 11(46):10757–10816, 2009. ISSN 1463-9084. doi:10.1039/b907148b.

[65] J. P. Perdew and A. Zunger. Self-interaction correction to density-functional approximations for many-electron systems. *Phys. Rev. B*, 23(10):5048–5079, 1981. ISSN 01631829. doi:10.1103/PhysRevB.23.5048.

[66] A. P. Sutton. *Electronic Structure of Materials*. Oxford University Press, Oxford, UK, first edition, 1993. ISBN 0198517548.

[67] S. Kurth, J. P. Perdew, and P. Blaha. Molecular and solid-state tests of density functional approximations: LSD, GGAs, and meta-GGAs. *Int. J. Quantum Chem.*, 75(45):889, 1999. ISSN 0020-7608. doi:10.1002/(SICI)1097-461X(1999)75:4/5<889::AID-QUA54>3.0.CO;2-8.

[68] J. P. Perdew, K. Burke, and M. Ernzerhof. Generalized gradient approximation made simple. *Phys. Rev. Lett.*, 77(18):3865–3868, 1996. ISSN 0031-9007. doi:10.1103/PhysRevLett.77.3865.

[69] K. Burke, J. P. Perdew, and Y. Wang. *Derivation of a generalized gradient approximation: The PW91 density functional*, pages 81–111. Springer US, Boston, MA, 1998. ISBN 978-1-4899-0316-7. doi:10.1007/978-1-4899-0316-7_7.

[70] F. Bloch. Uber die Quantenmechanik der Elektronen in Kristallgittern. *Zeitschrift fur Phys.*, 52(7-8):555–600, 1929. ISSN 14346001. doi:10.1007/BF01339455.

[71] N. W. Ashcroft and N. D. Mermin. *Solid State Physics*. Harcourt College Publishers, Orlando, FL, college edition, 1976. ISBN 0-03-083993-9.

[72] H. J. Monkhorst and J. D. Pack. Special points for Brillouin-zone integrations. *Phys. Rev. B*, 13(12):5188–5192, 1976. doi:10.1103/PhysRevB.13.5188.

[73] M. Methfessel and A. T. Paxton. High-precision sampling for Brillouin-zone integration in metals. *Phys. Rev. B*, 40(6):3616–3621, 1989. doi:10.1103/PhysRevB.40.3616.

[74] N. Marzari, D. Vanderbilt, A. De Vita, and M. C. Payne. Thermal contraction and disordering of the Al(110) surface. *Phys. Rev. Lett.*, 82(16):3296–3299, 1999. ISSN 0031-9007. doi:10.1103/PhysRevLett.82.3296.

[75] J. Aarons, M. Sarwar, D. Thompsett, and C. Skylaris. Perspective: Methods for large-scale density functional calculations on metallic systems. *J. Chem. Phys.*, 145(22):220901, 2016. ISSN 0021-9606. doi:10.1063/1.4972007.

[76] G. P. Kerker. Efficient iteration scheme for self-consistent pseudopotential calculations. *Phys. Rev. B*, 23(6):3082–3084, 1981. ISSN 01631829. doi:10.1103/PhysRevB.23.3082.

[77] P. Pulay. Convergence acceleration of iterative sequences: the case of SCF iteration. *Chem. Phys. Lett.*, 73(2):393–398, 1980. ISSN 1939-1536. doi:10.1016/0009-2614(80)80396-4.

[78] D. R. Hamann, M. Schlüter, and C. Chiang. Norm-conserving pseudopotentials. *Phys. Rev. Lett.*, 43(20):1494–1497, 1979. ISSN 0031-9007. doi:10.1103/PhysRevLett.43.1494.

[79] N. Troullier and L. J. Martins. Efficient pseudopotentials for plane-wave calculations. *Phys. Rev. B*, 43(3):1993–2006, 1991. doi:10.1103/PhysRevB.43.1993.

[80] S. Goedecker and K. Maschke. Transferability of pseudopotentials. *Phys. Rev. A.*, 45(1):88–93, 1992. doi:10.1103/PhysRevA.45.88.

[81] D. Vanderbilt. Soft self-consistent pseudopotentials in a generalized eigenvalue formalism. *Phys. Rev. B*, 41(11):7892–7895, 1990. ISSN 01631829. doi:10.1103/PhysRevB.41.7892.

[82] P. E. Blöchl. Projector augmented wave method. *Phys. Rev. B*, 50(24):17953–17979, 1994. doi:10.1103/PhysRevB.50.17953.

[83] G. Kresse. From ultrasoft pseudopotentials to the projector augmented-wave method. *Phys. Rev. B*, 59(3):1758–1775, 1999. ISSN 1098-0121. doi:10.1103/PhysRevB.59.1758.

[84] G. Kresse and J. Hafner. Ab initio molecular dynamics for liquid metals. *Phys. Rev. B*, 47(1):558–561, 1993. ISSN 01631829. doi:10.1103/PhysRevB.47.558.

[85] G. Kresse and J. Hafner. Ab initio molecular-dynamics simulation of the liquid-metalamorphous-semiconductor transition in germanium. *Phys. Rev. B*, 49(20): 14251–14269, 1994. ISSN 0163-1829. doi:10.1103/PhysRevB.49.14251.

[86] G. Kresse and J. Furthmüller. Efficiency of ab-initio total energy calculations for metals and semiconductors using a plane-wave basis set. *Comput. Mater. Sci.*, 6 (1):15–50, 1996. ISSN 09270256. doi:10.1016/0927-0256(96)00008-0.

[87] G. Kresse and J. Furthmüller. Efficient iterative schemes for ab initio total-energy calculations using a plane-wave basis set. *Phys. Rev. B*, 54(16):11169–11186, 1996. ISSN 0163-1829. doi:10.1103/PhysRevB.54.11169.

[88] K. Refson. Practical calculations using first-principles QM: Convergence, convergence, convergence (accessed on 16-05-2017), 2007. URL `http://www.tcm.phy.cam.ac.uk/castep/CASTEP_talks_07/refson1.pdf`.

[89] J. White. Ti_00.uspcc (accessed on 16-05-2017), 1998. URL `http://cmt.dur.ac.uk/Pseudopotentials/Ti_00.uspcc`.

[90] D. E. Sands. *Introduction to crystallography*. Dover Publishing, Mineola, New York, new editio edition, 1993. ISBN 0-486-67839-3.

[91] E. S. Fisher and C. J. Renken. Single-crystal elastic moduli and the hcp to bcc transformation in Ti, Zr, and Hf. *Phys. Rev.*, 135(2A):482–494, 1964. doi:10.1103/PhysRev.135.A482.

[92] O. N. Senkov, B. C. Chakoumakos, J. J. Jonas, and F. H. Froes. Effect of temperature and hydrogen concentration on the lattice parameter of beta titanium. *Mater. Res. Bull.*, 36(7-8):1431–1440, 2001. ISSN 00255408. doi:10.1016/S0025-5408(01)00604-3.

[93] F. D. Murnaghan. The compressibility of media under extreme pressures. *Proc. Natl. Acad. Sci.*, 30(9):244–247, 1944. ISSN 0027-8424. doi:10.1073/pnas.30.9.244.

[94] F. Birch. Finite elastic strain of cubic crystals. *Phys. Rev.*, 71(11):809–824, 1947. ISSN 0031899X. doi:10.1103/PhysRev.71.809.

[95] L-F. Huang, B. Grabowski, E. McEniry, D. R. Trinkle, and J. Neugebauer. Importance of coordination number and bond length in titanium revealed by electronic structure investigations. *Phys. Status Solidi*, 18(9):1907–1924, 2015. ISSN 03701972. doi:10.1002/pssb.201552280.

[96] M. Finnis. *Interatomic Forces in Condensed Matter (Oxford Series on Materials Modelling)*. Oxford University Press, Oxford, UK, 1st edition, 2003. ISBN 0198509774.

[97] A. M. Walker and D. Wilson. Scripts to calculate elastic properties from a set of strained structures (Accessed on 25-03-2017), 2010. URL `https://github.com/andreww/elastic-constants`.

[98] A. M. Walker. The effect of pressure on the elastic properties and seismic anisotropy of diopside and jadeite from atomic scale simulation. *Phys. Earth Planet. Inter.*, 192-193:81–89, 2012. ISSN 00319201. doi:10.1016/j.pepi.2011.10.002.

[99] B. E. Tegner, L. Zhu, and G. J. Ackland. Relative strength of phase stabilizers in titanium alloys. *Phys. Rev. B*, 85(21):3–6, 2012. ISSN 10980121. doi:10.1103/PhysRevB.85.214106.

[100] M. Jafari, N. Zarifi, M. Nobakhti, A. Jahandoost, and M. Lame. Pseudopotential calculation of the bulk modulus and phonon dispersion of the bcc and hcp structures of titanium. *Phys. Scr.*, 83(6):065603, 2011. ISSN 0031-8949. doi:10.1088/0031-8949/83/06/065603.

[101] K. Lejaeghere, V. Van Speybroeck, G. Van Oost, and S. Cottenier. Error estimates for solid-state density-functional theory predictions: An overview by means of the ground-state elemental crystals. *Crit. Rev. Solid State Mater. Sci.*, 39(1):1–24, 2014. ISSN 1040-8436. doi:10.1080/10408436.2013.772503.

[102] D. J. Bacon and V. Vitek. Atomic-scale modeling of dislocations and related properties in the hexagonal-close-packed metals. *Metall. Mater. Trans. A*, 33(13): 721–733, 2002. ISSN 1073-5623. doi:10.1007/s11661-002-1001-9.

[103] G. Kresse and J. Hafner. Norm-conserving and ultrasoft pseudopotentials for first-row and transition elements. *J. Phys. Condens. Matter*, 6(40):8245–8257, 1994. ISSN 0953-8984. doi:10.1088/0953-8984/6/40/015.

[104] N. Drakos, M. Hennecke, R. Moore, and H. Swan. The VASP pseudopotential database, 2016. URL http://cms.mpi.univie.ac.at/vasp/vasp/Pseudopotentials_supplied_with_VASP_package.html.

[105] K. Momma and F. Izumi. VESTA 3 for three-dimensional visualization of crystal, volumetric and morphology data. *J. Appl. Crystallogr.*, 44(6):1272–1276, 2011. ISSN 00218898. doi:10.1107/S0021889811038970.

[106] M. E. Eberhart, T. E. Jones, and M. A. Sauer. Visualizing the metallic bond, 2008. ISSN 10474838.

[107] P. G. Partridge. The crystallography and deformation modes of hexagonal close-packed metals. *Metall. Rev.*, 12:169–194, 1967. doi:10.1179/mtlr.1967.12.1.169.

[108] R. von Mises. Mechanik der festen Körper im plastisch-deformablen Zustand. *Nachrichten von der Gesellschaft der Wissenschaften zu Göttingen, Math. Klasse*, 1:582–592, 1913. URL http://eudml.org/doc/58894.

[109] N. E. Paton and W. A. Backofen. Plastic deformation of titanium at elevated temperatures. *Metall. Trans.*, 1(10):2839–2847, 1970. ISSN 10735615. doi:10.1007/BF03037822.

[110] Y. Minonishi, S. Morozumi, and H. Yoshinaga. $\{11\bar{2}2\}\ \langle\bar{1}\bar{1}23\rangle$ slip in titanium. *Scr. Metall.*, 16(4):427–430, 1982. ISSN 00369748. doi:10.1016/0036-9748(82)90166-1.

[111] I. P. Jones and W. B. Hutchinson. Stress-state dependence of slip in titanium-6Al-4V and other h.c.p. metals. *Acta Metall.*, 29(6):951–968, 1981. ISSN 00016160. doi:10.1016/0001-6160(81)90049-3.

[112] H. Numakura, Y. Minonishi, and M. Koiwa. $\langle\bar{1}\bar{1}23\rangle\ \{10\bar{1}1\}$ slip in titanium polycrystals at room temperature. *Scr. Metall.*, 20(11):1581–1586, 1986. ISSN 00369748. doi:10.1016/0036-9748(86)90399-6.

[113] A. Girshick, D. G. Pettifor, and V. Vitek. Atomistic simulation of titanium - II. Structure of 1/3 $\langle \bar{1}2\bar{1}0 \rangle$ screw dislocations and slip systems in titanium. *Philos. Mag. A*, 77(4):37–41, 1998. ISSN 0141-8610. doi:10.1080/01418619808221224.

[114] D. Hull and D. J. Bacon. *Introduction to dislocations*. Elsevier Ltd, Oxford, UK, fifth edition, 2011. ISBN 978-0-08-096672-4.

[115] V. Vítek. Intrinsic stacking faults in body-centred cubic crystals. *Philos. Mag.*, 18(154):773–786, 1968. ISSN 0031-8086. doi:10.1080/14786436808227500. URL http://dx.doi.org/10.1080/14786436808227500.

[116] V. Vitek, A. P. Sutton, D. A. Smith, and R. C. Pond. On the structure of grain-boundary dislocations. *Philos. Mag. A*, 39(2):213–224, 1979. ISSN 0141-8610. doi:10.1080/01418617908236894.

[117] B. Yin, Z. Wu, and W. A. Curtin. A systematic study of the stable stacking fault in hcp metals from first-principles. *Acta Mater.*, 123:223–234, 2017. ISSN 13596454. doi:10.1016/j.actamat.2016.10.042.

[118] D. H. Sastry, Y. V. R. K. Prasad, and K. I. Vasu. On the stacking fault energies of some hexagonal close-packed metals. *Scr. Metall.*, 3(1):927–930, 1969. doi:10.1016/0036-9748(69)90243-9.

[119] Y. Tang and J. A. El-Awady. Formation and slip of pyramidal dislocations in hexagonal close-packed magnesium single crystals. *Acta Mater.*, 71:319–332, 2014. ISSN 13596454. doi:10.1016/j.actamat.2014.03.022.

[120] M. S. Daw and M. I. Baskes. Embedded-atom method: Derivation and application to impurities, surfaces, and other defects in metals. *Phys. Rev. B*, 29(12):6443–6453, 1984. ISSN 01631829. doi:10.1103/PhysRevB.29.6443.

[121] G. J. Ackland, M. W. Finnis, and V. Vitek. Validity of the second moment tight-binding model. *J. Phys. F Met. Phys.*, 18(8):L153–L157, 1988. ISSN 0305-4608. doi:10.1088/0305-4608/18/8/002.

[122] A. Girshick, A. M. Bratkovsky, D. G. Pettifor, and V. Vitek. Atomistic simulation of titanium. I. A bond-order potential. *Philos. Mag. A*, 77(4):981–997, 1998. ISSN 0141-8610. doi:10.1080/01418619808221223.

[123] S. Plimpton. Fast parallel algorithms for short-range molecular dynamics. *J. Comput. Phys.*, 117(1):1–19, 1995. ISSN 00219991. doi:10.1006/jcph.1995.1039.

[124] C Kittel. *Introduction to solid state physics*. John Wiley and Sons, New York, 8th edition, 2004. ISBN 978-0471415268.

[125] A. P. Sutton and Balluffi R. W. *Interfaces in crystalline materials*. Oxford University Press, Oxford, UK, new edition, 2006. ISBN 978-0199211067.

[126] R. Pasianot and E. J. Savino. Embedded-atom-method interatomic potentials for hcp metals. *Phys. Rev. B*, 45(22):12704–12710, 1992. ISSN 01631829. doi:10.1103/PhysRevB.45.12704.

[127] M. Benoit, N. Tarrat, and J. Morillo. Density functional theory investigations of titanium $\gamma$-surfaces and stacking faults. *Model. Simul. Mater. Sci. Eng.*, 21(1): 015009, 2013. ISSN 0965-0393. doi:10.1088/0965-0393/21/1/015009.

[128] N. Tarrat, M. Benoit, and J. Morillo. Core structure of screw dislocations in hcp Ti: an ab initio DFT study. *Int. J. Mater. Res.*, 100(3):329–332, 2009. doi:10.3139/146.110055.

[129] Z. Guo, A. P. Miodownik, N. Saunders, and J-Ph. Schillé. Influence of stacking-fault energy on high temperature creep of alpha titanium alloys. *Scr. Mater.*, 54 (12):2175–2178, 2006. ISSN 13596462. doi:10.1016/j.scriptamat.2006.02.036.

[130] A. De Crecy, A. Bourret, S. Naka, and A. Lasalmonie. High resolution determination of the core structure of $1/3\langle 11\bar{2}0\rangle\{10\bar{1}0\}$ edge dislocation in titanium. *Philos. Mag. A*, 47(January 2015):245–254, 1983. ISSN 0141-8610. doi:10.1080/01418618308245221.

[131] A. Poty, J. M. Raulot, H. Xu, J. Bai, C. Schuman, J. S. Lecomte, M. J. Philippe, and C. Esling. Classification of the critical resolved shear stress in the hexagonal-close-packed materials by atomic simulation: Application to $\alpha$-zirconium and $\alpha$-titanium. *J. Appl. Phys.*, 110(1), 2011. ISSN 00218979. doi:10.1063/1.3599870.

[132] B. Legrand. Structure du coeur des dislocations vis $1/3\langle 11\bar{2}0\rangle$ dans le titane. *Philos. Mag. A*, 52(1):83–97, 1985. ISSN 0141-8610. doi:10.1080/01418618508237608.

[133] B. Legrand. Relation between the electronic structure and ease of gliding in hexagonal close-packed metals. *Philos. Mag. B*, 49(2):171–184, 1984. ISSN 1364-2812. doi:10.1080/13642818408227636.

[134] B. Legrand. *Influence de la structure electronique sur la facilite relative des glissements dans les metaux de structure hexagonale compacte.* PhD thesis, Universite Pierre et Marie Curie, 1984. URL http://www.iaea.org/inis/collection/NCLCollectionStore/_Public/16/043/16043245.pdf.

[135] Xiang-Yang Liu, James B Adams, Furio Ercolessi, and John A Moriarty. EAM potential for magnesium from quantum mechanical forces. *Model. Simul. Mater. Sci. Eng. Mater. Sci. Eng*, 4(4):293–303, 1996. ISSN 0965-0393. doi:10.1088/0965-0393/4/3/004.

[136] D. Y. Sun, M. I. Mendelev, C. A. Becker, K. Kudin, Tomorr Haxhimali, M. Asta, J. J. Hoyt, A. Karma, and D. J. Srolovitz. Crystal-melt interfacial free energies in hcp metals: A molecular dynamics study of Mg. *Phys. Rev. B - Condens. Matter Mater. Phys.*, 73(2):1–12, 2006. ISSN 10980121. doi:10.1103/PhysRevB.73.024116.

[137] S. R. Agnew, J. A. Horton, and M. H. Yoo. Transmission electron microscopy investigation of $\langle c+a \rangle$ dislocations in Mg and $\alpha$-solid solution Mg-Li alloys. *Metall. Mater. Trans. A*, 33(13):851–858, 2002. ISSN 1073-5623. doi:10.1007/s11661-002-1017-1.

[138] C. Domain and A. Legris. Investigation of glide properties in hexagonal titanium and zirconium: an ab-initio atomic scale study. *IUTAM Symp. Mesoscopic Dyn. Fract. Process Mater. Strength*, pages 411–420, 2004. ISSN 0925-0042. doi:10.1007/978-1-4020-2111-4_39.

[139] R. G. Hennig, T. J. Lenosky, D. R. Trinkle, S. P. Rudin, and J. W. Wilkins. Classical potential describes martensitic phase transformations between the $\alpha$, $\beta$, and $\omega$ titanium phases. *Phys. Rev. B*, 78(5):054121, 2008. ISSN 10980121. doi:10.1103/PhysRevB.78.054121.

[140] M. Ghazisaeidi and D. R. Trinkle. Core structure of a screw dislocation in Ti from density functional theory and classical potentials. *Acta Mater.*, 60(3):1287–1292, 2012. ISSN 13596454. doi:10.1016/j.actamat.2011.11.024.

[141] P. Kwaśniak, M. Muzyk, H. Garbacz, and K. J. Kurzydłowski. Influence of C, H, N, and O interstitial atoms on deformation mechanism in titanium - First principles calculations of generalized stacking fault energy. *Mater. Lett.*, 94:92–94, 2013. ISSN 0167577X. doi:10.1016/j.matlet.2012.12.002.

[142] P. Kwaśniak, H. Garbacz, and K. J. Kurzydłowski. Solid solution strengthening of hexagonal titanium alloys: Restoring forces and stacking faults calculated from first principles. *Acta Mater.*, 102:304–314, 2016. ISSN 13596454. doi:10.1016/j.actamat.2015.09.041.

[143] L. Liang. *Simulation ab initio des defauts etendus du Ti alpha en presence d'interstitiels H et O*. PhD thesis, Ecole Polytechnique, Universite Paris-Saclay, Route de Saclay, 91128 Palaiseau, France, 2016. URL `http://www.theses.fr/2016SACLX009`.

[144] L. Liang and O. B. M. Hardouin Duparc. Ab initio reappraisal of the dislocation-associated stacking faults in hcp titanium : a new dissociation mechanism. *Philos. Mag. Lett.*, 97(January):19–26, 2017. doi:10.1080/09500839.2016.1265680.

[145] X. Wu, R. Wang, and S. Wang. Generalized-stacking-fault energy and surface properties for hcp metals: A first-principles study. *Appl. Surf. Sci.*, 256(11):3409–3412, 2010. ISSN 01694332. doi:10.1016/j.apsusc.2009.12.042.

[146] N. Chaari, E. Clouet, and D. Rodney. First order pyramidal slip of $1/3\langle 1\bar{2}10\rangle$ screw dislocations in zirconium. *Metall. Mater. Trans. A Phys. Metall. Mater. Sci.*, 45(13):5898–5905, 2014. ISSN 10735623. doi:10.1007/s11661-014-2568-7.

[147] P. Kwaśniak, P. Śpiewak, H. Garbacz, and K. J. Kurzydłowski. Plasticity of hexagonal systems: Split slip modes and inverse Peierls relation in $\alpha$-Ti. *Phys. Rev. B - Condens. Matter Mater. Phys.*, 89(144105):144105, 2014. ISSN 1550235X. doi:10.1103/PhysRevB.89.144105.

[148] Z. Wu, B. Yin, and W. A. Curtin. Energetics of dislocation transformations in hcp metals. *Acta Mater.*, 119:203–217, 2016. ISSN 13596454. doi:10.1016/j.actamat.2016.08.002.

[149] L-F. Huang, B. Grabowski, J. Zhang, M-J. Lai, C. Cem Tasan, S. Sandlöbes, D. Raabe, and J. Neugebauer. From electronic structure to phase diagrams: A bottom-up approach to understand the stability of titanium-transition metal alloys. *Acta Mater.*, 113:311–319, 2016. ISSN 13596454. doi:10.1016/j.actamat.2016.04.059.

[150] C. Freysoldt, B. Grabowski, T. Hickel, J. Neugebauer, G. Kresse, A. Janotti, and C. G. Van De Walle. First-principles calculations for point defects in solids. *Rev. Mod. Phys.*, 86(1):253–305, 2014. ISSN 15390756. doi:10.1103/RevModPhys.86.253.

[151] L. Scotti and A. Mottura. Diffusion anisotropy of poor metal solute atoms in hcp-Ti. *J. Chem. Phys.*, 142:204308, 2015. ISSN 0021-9606. doi:10.1063/1.4921780.

[152] B. Medasani, M. Haranczyk, A. Canning, and M. Asta. Vacancy formation energies in metals: A comparison of MetaGGA with LDA and GGA exchange-correlation functionals. *Comput. Mater. Sci.*, 101:96–107, 2015. ISSN 09270256. doi:10.1016/j.commatsci.2015.01.018.

[153] S. L. Shang, B. C. Zhou, W. Y. Wang, A. J. Ross, X. L. Liu, Y. J. Hu, H. Z. Fang, Y. Wang, and Z. K. Liu. A comprehensive first-principles study of pure elements: Vacancy formation and migration energies and self-diffusion coefficients. *Acta Mater.*, 109:128–141, 2016. ISSN 13596454. doi:10.1016/j.actamat.2016.02.031.

[154] A. T. Raji, S. Scandolo, R. Mazzarello, S. Nsengiyumva, M. Härting, and D. T. Britton. Ab initio pseudopotential study of vacancies and self-interstitials in hcp titanium. *Philos. Mag.*, 89(20):1629–1645, 2009. ISSN 1478-6435. doi:10.1080/14786430903019032.

[155] D. R. Trinkle, M. D. Jones, R. G. Hennig, S. P. Rudin, R. C. Albers, and J. W. Wilkins. Empirical tight-binding model for titanium phase transformations. *Phys. Rev. B*, 73(9):1–9, 2006. ISSN 10980121. doi:10.1103/PhysRevB.73.094123.

[156] E. Hashimoto, E. A. Smirnov, and T. Kino. Temperature dependence of the Doppler-broadened lineshape of positron annihilation in $\alpha$-Ti. *J. Phys. F Met. Phys.*, 14(10):L215–L217, 1984. ISSN 0305-4608. doi:10.1088/0305-4608/14/10/004.

[157] Y. Kraftmakher. Equilibrium vacancies and thermophysical properties of metals. *Phys. Rep.*, 299:79–188, 1998. ISSN 03701573. doi:10.1016/S0370-1573(97)00082-3.

[158] V. O. Shestopal. Specific heat and vacancy formation in titanium at high temperatures. *Sov. Phys Solid State*, 7(11):2798–2799, 1966.

[159] J. P. Perdew, A. Ruzsinszky, G. I. Csonka, O. A. Vydrov, G. E. Scuseria, L. A. Constantin, X. Zhou, and K. Burke. Restoring the density-gradient expansion for exchange in solids and surfaces. *Phys. Rev. Lett.*, 100(13):136406, 2008. ISSN 0031-9007. doi:10.1103/PhysRevLett.100.136406.

[160] C. Herzig, Y. Mishin, and S. Divinski. Bulk and interface boundary diffusion in group IV hexagonal close-packed metals and alloys. *Metall. Mater. Trans. A*, 33 (March):765–775, 2002. ISSN 1073-5623. doi:10.1007/s11661-002-1006-4.

[161] A. Glensk, B. Grabowski, T. Hickel, and J. Neugebauer. Breakdown of the arrhenius law in describing vacancy formation energies: The importance of local anharmonicity revealed by ab initio thermodynamics. *Phys. Rev. X*, 4(1):011018, 2014. ISSN 21603308. doi:10.1103/PhysRevX.4.011018.

[162] K. Kuribayashi, S. Tanigawa, S. Nanao, and M. Doyama. Evaluation of the formation entropy of a single vacancy by means of positron annihilation. *Solid State Commun.*, 12(11):1179–1182, 1973. ISSN 00381098. doi:10.1016/0038-1098(73)90137-3.

[163] R. A. Johnson and J. R. Beeler. Point defects in titanium (M2). In *J. Met.*, volume 32, 8, page 15. Minerals Metals Materials Soc 420 Commonwealth Dr, Warrendale, PA 15086, 1980.

[164] C. Domain and A. Legris. Ab initio atomic-scale determination of point-defect structure in hcp zirconium. *Philos. Mag.*, 85(4-7):569–575, 2005. ISSN 1478-6435. URL http://www.tandfonline.com/doi/abs/10.1080/14786430412331334625.

[165] F. Willaime. Ab initio study of self-interstitials in hcp-Zr. *J. Nucl. Mater.*, 323 (2-3):205–212, 2003. ISSN 00223115. doi:10.1016/j.jnucmat.2003.08.005.

[166] L-F. Huang. Personal communication, 2016.

[167] W. W. Xu, S. L. Shang, B. C. Zhou, Y. Wang, L. J. Chen, C. P. Wang, X. J. Liu, and Z. K. Liu. A first-principles study of the diffusion coefficients of alloying elements in dilute $\alpha$-Ti alloys. *Phys. Chem. Chem. Phys.*, 18(25):16870–16881, 2016. ISSN 1463-9076. doi:10.1039/C6CP01899H.

[168] A. Shahba and S. Ghosh. Crystal plasticity FE modeling of Ti alloys for a range of strain-rates. Part I: A unified constitutive model and flow rule. *Int. J. Plast.*, 87:48–68, 2016. ISSN 07496419. doi:10.1016/j.ijplas.2016.09.002.

[169] N. E. Paton, R. G. Baggerly, and J. C. Williams. Deformation and Solid Solution Strengthening of Titanium-Aluminum Single Crystals, SC 526.7FR. Technical report, Rockwell International, Thousand Oaks, California, 1976.

[170] S. L. Altmann and C. J. Bradley. Lattice harmonics II. Hexagonal close-packed lattice. *Rev. Mod. Phys.*, 37(1):33–45, 1965. ISSN 00346861. doi:10.1103/RevModPhys.37.33.

[171] S. L. Altmann and A. P. Cracknell. Lattice Harmonics. *Rev. Mod. Phys.*, 37(1): 19–32, 1965. doi:10.1103/RevModPhys.37.19.

[172] F. C. Von der Lage and H. A. Bethe. A Method for Obtaining Electronic Eigenfunctions and Eigenvalues in Solids with An Application to Sodium. *Phys. Rev.*, 71(9):612–622, 1947. doi:10.1103/PhysRev.71.612.

[173] D. Rodney, L. Ventelon, E. Clouet, L. Pizzagalli, and F. Willaime. Ab initio modeling of dislocation core properties in metals and semi-conductors. *Acta Mater.*, 124:633–659, 2016. ISSN 13596454. doi:10.1016/j.actamat.2016.09.049.

# Appendix A

# $\gamma$-surface gradients

In chapter 5 I used root mean square differences between gradients of $\gamma$-surfaces to quantify the difference between surfaces computed using interatomic potentials (IPs) and density functional theory (DFT). Those results are shown in section 5.3.4. In this appendix I summarise how I computed the $\gamma$-surface gradients by using energy samples of the surfaces as well as slow Fourier transforms.

As described in section 5.1.3 each $\gamma$-surface is spanned by two lattice vectors $\mathbf{a}_1$ and $\mathbf{a}_2$. I sampled the surfaces using a discrete mesh of points $\mathbf{t}_{ij}$ such that:

$$\mathbf{t}_{ij} = \frac{i}{M}\mathbf{a}_1 + \frac{j}{N}\mathbf{a}_2, \tag{A.1}$$

where $i = \{0, 1, \ldots, M-1\}$, $j = \{0, 1, \ldots, N-1\}$. The lattice vectors and sampling meshes used in this study are described in section 5.2.2. The $\gamma$-surface energies at these sample points are defined as $\gamma_{ij} = \gamma(\mathbf{t}_{ij})$.

I used the lattice vectors $\mathbf{a}_1$ and $\mathbf{a}_2$ that span the $\gamma$-surface, as well as a third lattice vector $\mathbf{a}_3 = \mathbf{a}_1 \times \mathbf{a}_2$ to compute the reciprocal lattice vectors $\{\mathbf{a}_1^*, \mathbf{a}_2^*, \mathbf{a}_3^*\}$:

$$\mathbf{a}_1^* = 2\pi\frac{\mathbf{a}_2 \times \mathbf{a}_3}{\mathbf{a}_1 \cdot (\mathbf{a}_2 \times \mathbf{a}_3)} \;\; ; \;\; \mathbf{a}_2^* = 2\pi\frac{\mathbf{a}_3 \times \mathbf{a}_1}{\mathbf{a}_1 \cdot (\mathbf{a}_2 \times \mathbf{a}_3)} \;\; ; \;\; \mathbf{a}_3^* = 2\pi\frac{\mathbf{a}_1 \times \mathbf{a}_2}{\mathbf{a}_1 \cdot (\mathbf{a}_2 \times \mathbf{a}_3)}. \tag{A.2}$$

Then I used $\mathbf{a}_1^*$ and $\mathbf{a}_2^*$ in (A.2) to construct the wave-vectors:

$$\mathbf{k}_{pq} = \left(p - \frac{m}{2}\right)\mathbf{a}_1^* + \left(q - \frac{n}{2}\right)\mathbf{a}_2^*, \tag{A.3}$$

where $p = \{0, 1, \ldots, M-1\}$ and $q = \{0, 1, \ldots, N-1\}$. I then used the wave-vectors in (A.3) as well as the translation vectors in (A.1) to compute the Fourier coefficients $\tilde{\gamma}_{pq}$ of the $\gamma$-surface samples $\gamma_{ij}$:

$$\tilde{\gamma}_{pq} = \sum_{i=0}^{M-1} \sum_{j=0}^{N-1} \gamma_{ij} \exp\big(-i\mathbf{k}_{pq} \cdot \mathbf{t}_{ij}\big). \tag{A.4}$$

The corresponding inverse FT is defined as:

$$\gamma_{ij} = \frac{1}{MN} \sum_{p=0}^{M-1} \sum_{q=0}^{N-1} \tilde{\gamma}_{pq} \exp\left(i\mathbf{k}_{pq} \cdot \mathbf{t}_{ij}\right). \tag{A.5}$$

To compute the $\gamma$-surface gradient I expressed the translation vectors $\mathbf{t}_{ij}$ and the wave-vectors $\mathbf{k}_{pq}$ in cartesian components:

$$\begin{aligned} \mathbf{t}_{ij} &= \frac{i}{M}\mathbf{a}_1 + \frac{j}{N}\mathbf{a}_2 \\ &= t_{ij}^x \hat{\mathbf{x}} + t_{ij}^y \hat{\mathbf{y}} \\ &= \left[\frac{i}{M}a_{1x} + \frac{j}{N}a_{2x}\right]\hat{\mathbf{x}} + \left[\frac{i}{M}a_{1y} + \frac{j}{N}a_{2y}\right]\hat{\mathbf{y}}, \end{aligned} \tag{A.6}$$

where $\hat{\mathbf{x}}$ and $\hat{\mathbf{y}}$ are unit 2-d cartesian vectors, $a_{1x}$ and $a_{1y}$ are the projections of $\mathbf{a}_1$ along $\hat{\mathbf{x}}$ and $\hat{\mathbf{y}}$ respectively, and $a_{2x}$ and $a_{2y}$ are the projections of $\mathbf{a}_2$ along $\hat{\mathbf{x}}$ and $\hat{\mathbf{y}}$ respectively. I defined the cartesian components of the wave-vector $\mathbf{k}_{ij}$ in a similar fashion:

$$\begin{aligned} \mathbf{k}_{pq} &= \left(p - \frac{M}{2}\right)\mathbf{a}_1^* + \left(q - \frac{N}{2}\right)\mathbf{a}_2^* \\ &= k_{pq}^x \hat{\mathbf{x}} + k_{pq}^y \hat{\mathbf{y}} \\ &= \left[\left(p - \frac{M}{2}\right)a_{1x}^* + \left(q - \frac{N}{2}\right)a_{2x}^*\right]\hat{\mathbf{x}} \\ &+ \left[\left(p - \frac{M}{2}\right)a_{1y}^* + \left(q - \frac{N}{2}\right)a_{2y}^*\right]\hat{\mathbf{y}}, \end{aligned} \tag{A.7}$$

where $a_{1x}^*$ and $a_{1y}^*$ are the projections of $\mathbf{a}_1^*$ along $\hat{\mathbf{x}}$ and $\hat{\mathbf{y}}$ respectively, and $a_{2x}^*$ and $a_{2y}^*$ are the projections of $\mathbf{a}_2^*$ along $\hat{\mathbf{x}}$ and $\hat{\mathbf{y}}$ respectively. I then used these cartesian decompositions to define the gradient of the $\gamma$-surface at $\mathbf{t}_{ij}$ as follows:

$$\begin{aligned} \left(\frac{\partial \gamma_{ij}}{\partial x}\right)_{x=t_{ij}^x} &= \frac{1}{MN} \sum_{p=0}^{M-1} \sum_{q=0}^{N-1} i k_{pq}^x \tilde{\gamma}_{pq} \exp\big(i\mathbf{k}_{pq} \cdot \mathbf{t}_{ij}\big), \\ \left(\frac{\partial \gamma_{ij}}{\partial y}\right)_{y=t_{ij}^y} &= \frac{1}{MN} \sum_{p=0}^{M-1} \sum_{q=0}^{N-1} i k_{pq}^y \tilde{\gamma}_{pq} \exp\big(i\mathbf{k}_{pq} \cdot \mathbf{t}_{ij}\big). \end{aligned} \tag{A.8}$$